

AD-A235 424



2

AFOSR-TR-91-0248

STRENGTH AND MICROSTRUCTURE OF CERAMICS

BRIAN R. LAWN

Ceramics Division  
National Institute of Standards and Technology  
Gaithersburg, MD 20899

With S.J. Bennison, H.M. Chan, P. Chantikul, J. Kelly, S. Lathabai,  
N.P. Padture, M.J. Readey, J. Rödel, J.L. Runyan, M.R. Stoudt

Technical Report  
FY 90

AFOSR Contract Nos. ISSA-91-002  
NIST Project No. 4206464

for

Air Force Office of Scientific Research  
Bolling Air Force Base  
Washington, DC 20332

November 1990

DTIC  
ELECTE  
MAY 02 1991  
S E D

DTIC FULL COPY

DISTRIBUTION STATEMENT A

Approved for public release;  
Distribution Unlimited

91 5 01 011

STRENGTH AND MICROSTRUCTURE OF CERAMICS

BRIAN R. LAWN

Ceramics Division  
National Institute of Standards and Technology  
Gaithersburg, MD 20899

With S.J. Bennison, H.M. Chan, P. Chantikul, J. Kelly, S. Lathabai,  
N.P. Padture, M.J. Readey, J. Rödel, J.L. Runyan, M.R. Stoudt

Technical Report  
FY 90

AFOSR Contract Nos. ISSA-91-002  
NIST Project No. 4206464

for

Air Force Office of Scientific Research  
Bolling Air Force Base  
Washington, DC 20332

November 1990

OTIS  
CART  
NIST  
6

Accession For	
NTIS GRA&I	<input checked="" type="checkbox"/>
DTIC TAB	<input type="checkbox"/>
Unannounced	<input type="checkbox"/>
Justification	<input type="checkbox"/>
By _____	
Distribution/	
Availability Codes	
Dist	Avail and/or Special
A1	

# REPORT DOCUMENTATION PAGE

Form Approved  
OMB No. 0704-0188

Public reporting burden for this collection of information is estimated to average 1 hour per response, including the time for reviewing instructions, searching existing data sources, gathering and maintaining the data needed, and completing and reviewing the collection of information. Send comments regarding this burden estimate or any other aspect of this collection of information, including suggestions for reducing this burden, to Washington Headquarters Services, Directorate for Information Operations and Reports, 1215 Jefferson Davis Highway, Suite 1204, Arlington, VA 22202-4302, and to the Office of Management and Budget, Paperwork Reduction Project (0704-0188), Washington, DC 20503.

1. AGENCY USE ONLY (Leave blank)	2. REPORT DATE	3. REPORT TYPE AND DATES COVERED	
	November 1990	Technical Report - FY 90 <i>Annual</i>	
4. TITLE AND SUBTITLE  "Strength and Microstructure of Ceramics"		5. FUNDING NUMBERS  <i>AFOSR-ISSA-91-0002</i>	
6. AUTHOR(S)  Brian R. Lawn		8. PERFORMING ORGANIZATION REPORT NUMBER	
7. PERFORMING ORGANIZATION NAME(S) AND ADDRESS(ES)  National Institute of Standards & Technology Ceramics Division, Building 223, Room A347 Gaithersburg, MD 20899		10. SPONSORING/MONITORING AGENCY REPORT NUMBER  <i>23061A2</i>	
9. SPONSORING/MONITORING AGENCY NAME(S) AND ADDRESS(ES)  Air Force Office of Scientific Research Bolling Air Force Base Washington, D. C. 20332		11. SUPPLEMENTARY NOTES	
12a. DISTRIBUTION/AVAILABILITY STATEMENT  Unlimited		12b. DISTRIBUTION CODE	
13. ABSTRACT (Maximum 200 words)  Results of a program on the toughness properties of monophase ceramics that toughen by bridging are presented. Fracture mechanics models describing this behavior, in the particular context of strength, are developed. Results of strengths tests confirming the essential predictions of the theory are presented. Innovative processing routes suggested by the models are shown to lead to two-phase composites with impressive flaw insensitivity.			
14. SUBJECT TERMS		15. NUMBER OF PAGES	
		16. PRICE CODE	
17. SECURITY CLASSIFICATION OF REPORT Unclassified	18. SECURITY CLASSIFICATION OF THIS PAGE Unclassified	19. SECURITY CLASSIFICATION OF ABSTRACT Unclassified	20. LIMITATION OF ABSTRACT

## STRENGTH AND MICROSTRUCTURE OF CERAMICS

### INTRODUCTION

### APPENDED PUBLICATIONS

1. "In Situ Measurements of Bridged Crack Interfaces in the SEM"  
J. Rödel, J. Kelly and B.R. Lawn  
J. Am. Ceram. Soc., in press.
2. "A Loading Device for Fracture Testing of Compact Tension Specimens in the Scanning Electron Microscope"  
J. Rödel, J.F. Kelly, M.R. Stoudt and S.J. Bennison  
Scanning Microscopy, in press.
3. "Cyclic Fatigue from Frictional Degradation at Bridging Grains in Alumina"  
S. Lathabai, J. Rödel and B.R. Lawn  
J. Am. Ceram. Soc.
4. "Role of Grain Size in the Strength and R-Curve Properties of Alumina"  
P. Chantikul, S.J. Bennison and B.R. Lawn  
J. Am. Ceram. Soc. 73 2419 (1990).
5. "The Role of Crystallization of an Intergranular Glassy Phase in Determining Grain Boundary Residual Stresses in Debased Aluminas"  
N.P. Padture, H.M. Chan, B.R. Lawn and M.J. Readey  
Mater. Res. Soc. Sympos. Proc. 170 245 (1990).
6. "Fabrication of Flaw-Tolerant Aluminum-Titanate-Reinforced Alumina"  
J.L. Runyan and S.J. Bennison  
J. Europ. Ceram. Soc., in press.
7. "Fundamental Condition for Existence of Microcrack Clouds in Monophase Ceramics"  
B.R. Lawn  
J. European Ceram. Soc., in press.

## INTRODUCTION

This program is concerned with research into the role of microstructure in the toughness and strength properties of flaw-tolerant ceramics, i.e. ceramics with strong R-curves. The R-curve is now understood to be crucial to the utility of monophase ceramics and multiphase composites in applications where high toughness is paramount. Our group has been seeking to identify and analyze the interrelations between R-curve processes and materials characteristics, both to establish reliable design criteria and tailor new, superior ceramics with maximum resistance to damage accumulation and degradation. A key aspect of our approach has been to establish strong links between properties and processing, fracture mechanics experimentation and modelling, materials design and characterization. The results of these studies are summarized in the appended publications.

Part of the fracture mechanics experimentation has been to continue with in situ observations of grain-localized bridging in elementary ceramics (e.g. aluminas), as well as (more recently) in two-phase composites, using a device that seats inside the SEM. Our studies help to determine the underlying micromechanics of the bridging process. We are now able to monitor crack growth in ceramics with remote control from outside the SEM in various loading modes, including cyclic. Some of this work is described in appended papers [1,2].

Work on cyclic fatigue has revealed important strength degradation with time, not only to moisture but also to bridge degradation. The in situ device has been useful in identifying directly a mechanism for this degradation. Sliding grains at bridging points generate very high stresses which produce

wear products, leading to progressive reduction in the contact friction. This reduces the shielding, and hence the strength. Results and fracture mechanics modelling of this process are presented in Ref. [3].

A critical facet of our program is that of the role of microstructure in the R-curve. With the bridging mechanism identified and understood, fracture mechanics models have been developed by our group. These models incorporate the essential elements of the microstructure into the underlying constitutive stress-separation function for the grain pullout. Recent versions allow one to predict the special role of the microstructural scaling, especially grain size, on the R-curve and strength. A systematic experimental study on alumina ceramics over a wide range of grain sizes confirms the basic predictions of the model, and explains previous mysteries concerning observed strength vs grain size relations [4]. On the other hand, incorporation of small additive phases at the grain boundaries has little effect on the properties [5].

Another important variable in the bridging fracture mechanics is the level of internal residual stress from thermal expansion anisotropy. The bridging models tell us that such stresses should augment the frictional tractions responsible for the toughening. We have fabricated two-phase alumina/aluminum-titanate ceramics, for which the expansion mismatch is uncommonly high. This material exhibits extraordinary flaw insensitivity, i.e. strength which are virtually independent of starting flaw size [5,6]. Work is proceeding on this exciting new area of properties-processing research.

Finally, we are paying attention to the possibility that some of the more complex ceramics with high internal stresses might exhibit microcracking. Initial work in this area is contained in Ref. [7].

IN SITU MEASUREMENTS OF BRIDGED CRACK INTERFACES IN THE SEM

Jürgen Rödel,\* James F. Kelly, Brian R. Lawn

Ceramics Division  
National Institute of Standards and Technology  
Gaithersburg, MD 20899

June 1990

For: J. Am. Ceram. Soc.

-----  
\* Guest Scientist: On leave from the Department of Materials Science  
and Engineering, Lehigh University, Bethlehem, PA 18015

ABSTRACT

A device for in situ SEM examination of crack propagation during loading of compact tension specimens is described, with a specific demonstration on an alumina ceramic. The device facilitates direct qualitative observations of the inception and subsequent frictional pullout of grain-localized bridges at the crack interface. Quantitative data on the bridging mechanism are obtained from measurements of the crack-opening displacements behind the crack tip. The crack profile is found to be closer to linear than parabolic at the bridged interface. Deconvolution of these crack-opening data allow for an evaluation of the closure tractions operative at the crack walls within the bridging zone, and thence the R-curve.

## 1. INTRODUCTION

The achievement of respectable fracture toughness in brittle ceramics necessitates the incorporation of crack-tip shielding agents like frontal-zone phase transformations [1] or microcracking [2], crack-interface fiber pullout [3] or interlocking grain sliding [4,5]. A proper understanding of the constitutive micromechanics of such processes can be gained only by direct observation of the crack shielding zone at the microstructural level during loading (and unloading, where applicable). In aluminas, for instance, *in situ* optical microscopy has been used to identify crack-interface grain bridging as the primary cause of R-curve toughening [4,6], a mechanism that had passed unnoticed in previous, conventional postmortem surface fractography. But while those studies have led to working microstructural constitutive relations for R-curve modelling of crack-interface bridging in simple monophase ceramics [5,7], finer elements of the restraining mechanisms remain obscure. Optical microscopy is severely limited in its capacity to discern critical details of grain pull-out and detachment. It is even more restrictive as a quantitative tool: in typical microstructures the crack-wall separations at the bridged interface are on the order 1  $\mu\text{m}$  or less.

Accordingly, we have custom-designed a device for *in situ* crack observations in the scanning electron microscope (SEM). Previous SEM straining fixtures for tensile specimens or bend bars [8-10] have demonstrated the feasibility of the approach. Our device allows one to follow the progress of crack propagation at relatively high magnification in compact tension specimens with externally controlled loading, and thence to gain quantitative insight into the underlying R-curve processes.

In this paper we briefly describe the fixture and illustrate its potential by tests on a polycrystalline alumina with demonstrated R-curve characteristics. Micrographs depicting the evolution of interlocking grain sites are presented as illustrations of the capacity to resolve essential microstructural detail at the bridged crack interface. Crack-opening displacement (COD) measurements are made along the bridging zone during the crack evolution. Corresponding bridging stresses in the crack wake are deconvoluted from these measurements, as functions of both COD and crack-plane coordinate. From these functions, we determine the R-curve characteristics for our particular material/geometry system.

## 2. SEM CRACK PROPAGATION STUDIES

### 2.1 The SEM Device

Essential details of the SEM crack propagation device are shown in the schematic of Fig. 1. The device allows remote electronic application and monitoring of the applied load. Extension of a piezoelectric translator T delivers an opening force to the specimen S via pivot arms P and loading arms L. The P arms are connected to the L arms by ball-bearing joints and to the base of the device by pin joints for maximum flexibility. A load cell C mounted in one of the L arms measures the transmitted force. The piezoelectric translator is activated by a high voltage amplifier which, in conjunction with a function generator, allows application of any prescribed load-time function (including, potentially, cyclic). The device operates

effectively as a "soft" machine: that is, crack extension occurs under nearly constant load.

The entire fixture is housed within the chamber of a SEM <sup>1</sup>. Crack-interface events during externally controlled loading can be viewed in real time and are routinely taped on a video recording unit for closer study.

A more detailed description of the unit will be given elsewhere [11].

## 2.2 Crack Propagation Specimens

Alumina disks 4 mm thick and 100 mm diameter were prepared by hot-pressing fine powder (nominal particle size 0.5  $\mu\text{m}$ ) <sup>2</sup>, without additives, at 1650°C for 3 hours at 35 MPa in vacuum. The pressed material was non-porous (> 99.9% density), and the microstructure was equiaxed with a grain size of 11  $\mu\text{m}$ . The disks were ground to 1 mm thickness and the prospective viewing surface polished with diamond paste to 1  $\mu\text{m}$  finish.

Notches were sawn and loading holes drilled in the disks to form compact-tension specimens. The distance from the load points to the crack plane was 7 mm and from the line of the loading arms to the initial notch tip 15 mm. The notch root radius was 150  $\mu\text{m}$ . To enhance stability in the initial crack extension the notch was cut at an angle 28° to the surface in quasi-chevron geometry, i.e. so that the tip extended some 2 mm further on the unpolished side. A Vickers indentation starter crack of diameter  $\approx$  240  $\mu\text{m}$  (load 50 N)

---

<sup>1</sup> Amray 1830, Amray Inc., Bedford, MA.

<sup>2</sup> Sumitomo AKP-HP grade (99.995 % pure, 0.5  $\mu\text{m}$  crystallites), Sumitomo Chemical America, New York, NY.

was then placed in the polished surface with its center 200  $\mu\text{m}$  in front of the notch, in alignment with the notch plane. This starter crack was made to pop in some 300  $\mu\text{m}$  beyond the indentation center in a preliminary load cycle. The notch was then re-sawn through the indentation, leaving a pre-crack  $\approx 100 \mu\text{m}$  long. After the first crack propagation run through  $\approx 2 \text{ mm}$  (i.e. through to the end of the chevron) the specimen was removed and re-sawn, for second and third runs.

Some soda-lime glass specimens were also prepared to similar dimensions, as non-R-curve controls. After sawing the notch, these specimens were annealed for 1 hour at 550°C to remove residual stresses.

Specimens were gold coated before testing in the SEM. The evolution of bridging grains at selected sites in the crack wake was followed as the crack tip advanced. Video recordings were made along the interfaces at each of the fully propagated cracks for profile measurements. The COD measurements themselves were made only in well-behaved regions, e.g. at grain facets oriented normal to the load axis and located away from any secondary cracking around bridging sites. The cracks were rendered highly visible in the secondary electron mode by edge charging. This charging limited the absolute resolution of surface-surface separations to about 70 nm, although relative measurements could be made to better than 30 nm.

### 3. **RESULTS**

#### 3.1 Qualitative Observations of Bridging Sites

General observations in our alumina confirm the basic conclusions from earlier studies with optical microscopy [4,6]. Crack extension occurred in a discontinuous fashion, at load increments from 5 to 15 N, but remained essentially stable during the entire loading, to a maximum level of  $\approx$  300 N. The fracture mode was predominantly intergranular. Active grain bridges were observed along the entire crack trace and over the entire propagation distance. No indication of a microcrack-cloud zone was observed, even though secondary cracking of grain facet dimensions adjoining the primary crack interface was readily discernible (see below).

Specific examples of SEM observations in the alumina are shown in Figs. 2 and 3. Fig. 2 shows a bridging site in the crack wake some 1300  $\mu\text{m}$  behind the tip. That associated wake closure forces must be operative is immediately apparent from the severe disruption of individual grains at and around the bridge sites. The capacity to resolve and measure crack-opening displacements is also clear from this micrograph.

Fig. 3 depicts successive views of a second region, at two stages in the applied loading. The distances of this region behind the crack tip at these two stages are 660  $\mu\text{m}$  in (a) and 1190  $\mu\text{m}$  in (b). Two persistent contact points, at P and S, are indicated. At some load between (a) and (b) frictional tractions at P have opened up a network of secondary microfractures adjoining both sides of the primary crack interface. At S a single secondary microfracture has developed in the large grain at right prior to (a). Note

that this latter microfracture has closed significantly between (a) and (b), indicating a falloff of the frictional tractions. The grain at S may conveniently be viewed as a fixed-end cantilever beam whose deflection reflects the magnitude of the internally applied friction force.

By contrast, the cracks in the soda-lime glass propagated relatively smoothly, but at a steady rate (typically,  $\approx 1 \mu\text{m}\cdot\text{s}^{-1}$ ) at fixed load, indicating the presence of slow crack growth even in vacuum [12]. Reducing the applied load on the specimen by about 5% was sufficient to bring the crack system to equilibrium.

### 3.2 Quantitative Measurements of Crack-Opening Displacements

Crack-opening displacements,  $2u(x)$ , were measured for our specimens, with  $x$  the distance behind the crack tip as indicated in the schematic of Fig. 4. Figs. 5 and 6 show results from repeated crack propagation runs on the glass controls and the alumina, respectively.

The near-tip profiles for stress-free crack surfaces are usually represented by the Irwin K-field plane-strain displacement relation [13]

$$u(x) = (8x/\pi)^{1/2} K_A/E' \quad (1)$$

where  $E' = E/(1 - \nu^2)$  in plane strain,  $E$  Young's modulus (400 GPa for alumina and 70 GPa for glass),  $\nu$  Poisson's ratio (taken as 0.25 for both materials), and  $K_A$  the applied stress-intensity factor. Eq. 1 may be expected to remain a reasonable approximation for non-bridged cracks extending from sufficiently long notches ( $\Delta c \ll c_0$ , Fig. 4). A parabolic data fit may therefore be used to determine  $K_A$  [14]. For the glass in Fig. 5 a profile corresponding to  $K_A =$

$0.56 \text{ MPa} \cdot \text{m}^{1/2}$  (i.e. a little below the reported value  $0.7 \text{ MPa} \cdot \text{m}^{1/2}$  for crack propagation at velocity  $1 \mu\text{m} \cdot \text{s}^{-1}$  in vacuum [12]) passes through the data.

For alumina in Fig. 6, on the other hand, no such fit is possible with a single value of  $K_A$ . Bridging tractions in this material appear to have a strong modifying influence on the crack profile. The solid curve through the data is a theoretical fit allowing for this influence, to be described below (Sect. 3.3). We see that the profile in this material is closer to linear than parabolic. Included as the dashed curves in Fig. 6 are asymptotic parabolas according to Eq. 1 with  $K_A = 4.6 \text{ MPa} \cdot \text{m}^{1/2}$  at the crack mouth (notch tip) (evaluated from the externally measured load using a stress-intensity factor solution for compact tension specimens at  $\Delta c = 1.9 \text{ mm}^3$ ) and  $2.0 \text{ MPa} \cdot \text{m}^{1/2}$  at the crack tip (corresponding to the grain boundary toughness,  $T_0$  for alumina [5]).

We reiterate that the COD data in Figs. 5 and 6 correspond to measurements along the crack plane at stationary crack length ( $\Delta c = 1.9 \text{ mm}$ ). Alternatively, one may monitor the COD at the stationary notch tip as a function of variable crack extension  $\Delta c$ . Results of such measurements for the alumina are presented in Fig. 7.

### 3.3 Numerical Calculation of Closure Stresses in the Crack Wake

We indicated above that the crack profile in alumina deviates from the standard parabolic profile because of bridging tractions effective at the

---

<sup>3</sup> Using the formula for standard circular specimens [15], but with a correction factor allowing for non-standard load-point positions from a general solution for rectangular specimens [16].

crack walls. The profile may thereby be used to compute the magnitude of these bridging tractions via an integral equation for continuum slit cracks [17,18]. In the limit of small bridging zones ( $\Delta c = 1.9$  mm  $\ll c = 22$  mm) the profile may be approximated by the Barenblatt relation [17] for cracks under applied stress

$$u(x) = (8x/\pi)^{1/2} K_A/E' - (2/\pi E') \int_0^{\Delta c} p(x') \ln[(x'^{1/2} + x^{1/2})/(x'^{1/2} - x^{1/2})] dx' \quad (2)$$

with  $x$  a field point at which the displacement is to be evaluated and  $x'$  a source point for the stresses  $p(x')$ .

The problem now consists of finding a solution for a stress function  $p(x')$  consistent with the measured profile in Fig. 6. Generally, Eq. 2 is analytically untractable, so numerical analysis is required. To facilitate such an analysis, the stress function was taken to have the empirical "tail-like" form [5,7]

$$p(x') = p_M (1 - x'/\Delta c_s)^n \quad (3)$$

with  $p_M$  the peak stress,  $\Delta c_s$  the bridging zone size at steady state and  $n$  an exponent. Note that this function has limiting values  $p = p_M$  at  $x' = 0$  ( $u = 0$ ) and  $p = 0$  at  $x' = \Delta c_s$  ( $u = u_0$ ), and that  $n$  will generally be expected to vary with  $\Delta c$ . Starting with initial estimates from [7] for  $p_M$  and  $\Delta c_s$  at  $n = 1$  for an alumina with our grain size, iterative parametric adjustments were made to the stress function in Eq. 3 until the calculated crack profile  $u(x)$  in Eq. 2 deviated from the (smoothed-out) data set in Fig. 6 by less than a prescribed amount (30 nm) at any position  $x$ . This procedure yielded final values  $p_M = 70$  MPa,  $\Delta c_s = 2.5$  mm and  $n = 2.5$  for the half-chevron crack at  $\Delta c$

= 1.9 mm. The ensuing  $u(x)$  function is represented as the smooth curve in Fig. 6.

Fig. 8a plots the appropriately calibrated stress function  $p(x')$  in Eq. 3. The closure stresses decay from  $\approx 70$  MPa at the crack tip to  $\approx 2$  MPa at the crack mouth (notch tip). The corresponding stress-separation function  $p(u)$  in Fig. 8b is obtained in conjunction with Eq. 2. The crack-opening displacement at the notch tip corresponding to  $\Delta c = 1.9$  mm is  $2u_0 = 1300$  nm.

### 3.4 Calculations of the Crack-Tip Shielding Toughness and the R-Curve

Given the calibrated stress functions  $p(x')$  and  $p(u)$ , we may calculate the shielding contribution to the toughness.

Let us do this first for the crack of fixed size  $\Delta c = 1.9$  mm ( $2u_0 = 1300$  nm) in Fig. 6. We may do this in two ways:

(i) Stress-intensity factor. The material toughness consists of superposable contributions from the intrinsic (grain boundary) cohesive forces,  $T_0$ , and the extrinsic microstructural shielding,  $T_\mu$ . At equilibrium, the net toughness balances the applied  $K$ -field [19]:

$$K_A = T = T_0 + T_\mu. \quad (4)$$

The shielding term may be determined from the Greens function relation [15]

$$T_\mu = (2/\pi)^{1/2} \int_0^{\Delta c} p(x') dx' / x'^{1/2}. \quad (5)$$

Numerical integration gives  $T_\mu = 2.6 \text{ MPa} \cdot \text{m}^{1/2}$  for  $\Delta c = 1.9$  mm. This result compares with the value  $T_\mu = K_A - T_0 = 4.6 - 2.0 = 2.6 \text{ MPa} \cdot \text{m}^{1/2}$  from the

asymptotic curves in Fig. 6. \*

(ii) Mechanical-energy-release rate. The equilibrium relation Eq. 4 may be alternatively expressed as a balance between the applied mechanical-energy-release rate,  $G_A$ , and the net crack-resistance energy,  $R$ :

$$G_A = R = R_0 + R_\mu . \quad (6)$$

The shielding term is readily found from [19,20]

$$R_\mu = 2 \int_0^{u_0} p(u) du \quad (7)$$

Numerical integration gives  $R_\mu = 41.8 \text{ J} \cdot \text{m}^{-2}$ .

The values thus obtained can be checked for self-consistency through the equivalence relations [21]

$$G_A = K_A^2/E' \quad (8a)$$

$$R_0 = T_0^2/E' . \quad (8b)$$

Eliminating  $G_A$  and  $K_A$  using Eqs. 4 and 6, and inserting the above value of  $R_\mu$  obtained from Eq. 7 along with the previously cited  $E'$  and  $T_0$  for our alumina, we obtain  $T_\mu = (T_0^2 + E' R_\mu)^{1/2} - T_0 = 2.7 \text{ MPa} \cdot \text{m}^{1/2}$ , which compares with the value 2.6 from Eq. 4.

Now let us consider how we may determine the  $R$ -curve from the above analysis. From Eq. 7,  $R_\mu$ , hence  $R$ , may be evaluated directly as the area

---

\* Note that application of Eq. 5 to compute  $T_\mu$  at any other  $\Delta c$  would strictly require reevaluation of Eq. 3, specifically  $n$ , at that specific  $\Delta c$ .

under the  $p(u)$  curve in Fig. 8b. Numerical integration yields the function  $R(u)$  in Fig. 9a. This result may be converted to the more familiar R-curve function  $R(\Delta c)$  using the data points from Fig. 7. That function is plotted in Fig. 9b. Note that since  $p(u)$  is an intrinsic material function,  $R(u)$  is a unique quantity for our alumina; but  $R(\Delta c)$ , insofar as it may be dependent on the crack-profile relation  $u(\Delta c)$ , is specific to our crack geometry.

#### 4. DISCUSSION

We have sought to demonstrate that useful qualitative and quantitative information concerning the micromechanics of crack-tip shielding by grain bridging in monophase ceramics can be gained from in situ observations in the SEM. The most immediate outcome from our crack-interface observations on alumina is the confirmed existence of such bridging, pictorially in Figs. 2 and 3 and graphically in Fig. 9. Such observations usefully reinforce earlier inferences as to the efficacy of bridging as a toughening mechanism from the classic wake sawcut experiments of Knehans and Steinbrech [22]. They also allow us to make useful inferences concerning the micromechanics of grain pullout; recall our description of secondary fractures (fortuitous "internal load cells") in Fig. 3, indicative of a falloff in frictional force with increasing crack-wall separation.

Our results in Fig. 6 also show that (within experimental scatter) the crack profile at the bridged interface is closer to linear than parabolic. This is in keeping with studies on bridged cracks in fiber-reinforced cementitious composites [23]. An empirical linear COD relation is therefore

probably most appropriate for incorporation into fracture mechanics models of bridging zones for R-curve (T-curve) analysis [5,7,24].

It will be noted that evaluation of the equilibrium crack profile in Eq. 2 requires specification of  $K_A$  for the half-chevron crack.  $K_A$  determines the scale of the shielding zone displacement field, thereby avoiding the necessity of making COD measurements in the notch region. Alternatively, one could eliminate  $K_A$  altogether from Eq. 2 by substitution of Eqs. 4 and 5:

$$u(x) = (8x/\pi)^{1/2} T_0/E' + 4/\pi E' \int_0^{\Delta c} p(x') \{ (x/x')^{1/2} - \ln[(x'^{1/2} + x^{1/2})/(x'^{1/2} - x^{1/2})] \} dx' \quad (9)$$

so that, given only the intrinsic toughness term  $T_0$ , one may compute the profile without having to evaluate the applied stress-intensity factor. This is a special advantage in those cases where the macroscopic crack geometry is ill-defined. It must be reiterated that the validity of Eq. 9 is contingent on satisfaction of the small-scale bridging zone approximation,  $\Delta c \ll c$ , and therefore contains no specific information on the profile in the far field.

These considerations open the way to evaluation of  $T_0$  from the COD data. In cases (like ours) where intergranular fracture dominates, this quantity relates to the basic surface and grain boundary energies,  $\gamma_s$  and  $\gamma_{GB}$ , via  $T_0 = [(2\gamma_s - \gamma_{GB})E]^{1/2}$  [21]; the relative values of  $\gamma_{GB}$  and  $\gamma_s$  (among other things) determine whether a crack will or will not remain along an intergranular path (and hence preserve the most favorable conditions for bridge formation [7]). Access to  $T_0$  is restricted in conventional pre-crack test procedures because pop-in generally starts the system well up the R-curve. In principal,  $T_0$  should be determinable from the lower bound of the data in Fig. 6, which reflects COD measurements taken within two or three

grains behind the crack tip (i.e. within a typical bridge spacing). Thus in Fig. 6 we are able to estimate  $T_0 \approx 2.0 \text{ MPa} \cdot \text{m}^{1/2}$  for our alumina. In our case experimental scatter limits the accuracy of this approach, but optimization of the SEM resolution may provide useful estimates in materials with stronger R-curves.

Perhaps the most consequential result from the COD data in Figs. 6 and 7 is the evaluation of the bridging stress functions  $p(u)$  and  $p(x')$ . Notwithstanding the fact that our parametric fitting procedure is constrained by the empirical relation in Eq. 3, the data confirm the existence of a "tail-dominated" constitutive relation, Fig. 8; i.e. maximum restraint at the crack tip, with near-linear falloff along the crack-wake interface. Our  $p(u)$  function may be compared with an independent, indirect determination from indentation-strength data on other aluminas, shown as the dashed line in Fig. 8 [25]. The present evaluation indicates a substantially greater toughening due to bridging; the discrepancy may reflect material-to-material variations and/or uncertainties in deconvoluting the indentation data [25]. Once  $p(u)$  is established, the R-curve can be determined from Eqs. 6 and 7. The ensuing  $R(u)$  and  $R(\Delta c)$  functions in Figs. 9a and 9b show an initial sharp rise from  $\approx 10 \text{ J} \cdot \text{m}^{-2}$  at small crack openings (or extensions), to an asymptotic plateau  $\approx 50 \text{ J} \cdot \text{m}^{-2}$  at large openings (extensions). (The true plateau value could not be obtained in this study, because the crack size range covered in Figs. 6 and 7 did not extend beyond the range of the bridging zone.)

It is important to acknowledge possible sources of systematic error in the stress-function and R-curve evaluations in Figs. 8 and 9. In using Eq. 2 we have ignored the influence of finite notch length and outer specimen dimensions in our quasi-chevron configuration. Detailed analyses show that

boundary effects can be significant in determining displacement profiles in the compact-tension geometry, especially with short notches [26]. Also, we have not addressed the possible influence of path deflections (with their connotation of shear modes) on the normal crack displacements.

The present study has focussed on a monophase ceramic with moderate grain size. Our device would appear to be potentially even more useful for ceramics with coarser microstructures and multi-phase composites, where the toughening events are more dramatic and the R-curves more pronounced. Also, attention has been given only to monotonic loading. Observations in cyclic loading could provide useful clues as to fatigue mechanisms, which remain obscure in ceramic materials. Fatigue might be especially important in materials with strong R-curve behavior, due to cumulative damage to bridges on repeated unloading. COD measurements at the crack mouth (or some other stationary point of interest at the crack interface) could provide a quantitative measure of any such degradation with number of cycles.

## 5. CONCLUSIONS

- (i) A device for in situ investigation of crack interfaces in the SEM has been described.
- (ii) Micrographic evidence for evolution of bridging grains in alumina has been presented.
- (iii) COD measurements as a function of both the distance from the crack tip

and crack extension have been analyzed for alumina. The data provide a measure of the crack-tip shielding from bridging.

(iv) The bridging stress functions  $p(u)$  and  $p(x')$  have been computed self-consistently from the crack profile measurements.

(v) Crack-resistance functions  $R(u)$  and  $R(\Delta c)$  have been evaluated from the stress functions.

#### ACKNOWLEDGEMENTS

We are indebted to S.J. Bennison and M.R. Stoudt for help in the design of the fracture device, to B.N. Cox for discussions on the bridged-crack profile, and to E.R. Fuller for assistance with the numerical calculation. Funding was provided by the U.S. Air Force Office of Scientific Research.

## REFERENCES

1. R.M. McMeeking and A.G. Evans, "Mechanics of Transformation Toughening in Brittle Materials," J. Am. Ceram. Soc. 65[5] 242-46 (1982).
2. M. Rühle, A.G. Evans, R.M. McMeeking, P.G. Charalambides and J.W. Hutchinson, "Microcrack Toughening in Alumina/Zirconia," Acta Metall. 35[11] 2701-10 (1987).
3. D.B. Marshall and A.G. Evans, "Failure Mechanisms in Ceramic-Fiber/Ceramic-Matrix Composites," J. Am. Ceram. Soc. 68[5] 225-31 (1985).
4. P.L. Swanson, C.J. Fairbanks, B.R. Lawn, Y.-W. Mai and B.J. Hockey, "Crack-Interface Grain Bridging as a Fracture Resistance Mechanism in Ceramics: I. Experimental Study on Alumina," J. Am. Ceram. Soc. 70[4] 279-289 (1987).
5. Y.-W. Mai and B.R. Lawn, "Crack-Interface Grain Bridging as a Fracture Resistance Mechanism in Ceramics: II. Theoretical Fracture Mechanics Model," J. Am. Ceram. Soc. 70[4] 289-294 (1987).
6. P.L. Swanson, "Crack-Interface Traction: A Fracture-Resistance Mechanism in Brittle Polycrystals"; pp. 135-55 in Advances in Ceramics, Vol. 22, Fractography of Glasses and Ceramics. American Ceramic Society, Columbus, OH, 1988.
7. S.J. Bennison and B.R. Lawn, "Role of Interfacial Grain-Bridging Sliding Friction in the Crack-Resistance and Strength Properties of Nontransforming Ceramics," Acta Metall. 37[10] 2659-71 (1989).
8. A. Nagy, J.B. Campbell and D.L. Davidson, "High-Temperature, Cyclic Loading Stage for the Scanning Electron Microscope," Rev. Sci. Instrum. 55[5] 776-82 (1984).

9. H. Frei and G. Grathwohl, "Development of a Piezotranslator-based Bending Device for *in situ* SEM Investigations of High-Performance Ceramics," J. Phys. E: Sci. Instrum. 22[8] 589-93 (1989).
10. H. Kodama, H. Sakamoto and T. Miyoshi, "Silicon Carbide Monofilament Reinforced Silicon Nitride or Silicon Carbide Matrix Composites," J. Am. Ceram. Soc. 72[4] 551-58 (1989).
11. J. Rödel, J.F. Kelly, M.R. Stoudt and S.J. Bennison, "A Loading Device for Fracture Testing of Compact Tension Specimen in the SEM," to be published in Scanning Microscopy.
12. S.M. Wiederhorn, H. Johnson, A.M. Diness and A.H. Heuer, "Fracture of Glass in Vacuum," J. Am. Ceram. Soc. 57[8] 336-41 (1974).
13. G.R. Irwin, "Fracture"; pp. 551-94 in Handbuch der Physik, Vol. 6. Springer-Verlag, Berlin, 1958.
14. E. Sommer, "Experimental Determination of Stress Intensity Factor By COD Measurements," in Mechanics of Fracture, Vol. 7, edited by G.C. Sih, Nijhoff Publishers, 1981.
15. American Society for Testing and Materials, Vol. 3.01, E-399-83. A.S.T.M., Philadelphia, 1989.
16. H. Tada, P.C. Paris and G.R. Irwin, The Stress Analysis Handbook; Ch. 2. Paris Productions (and Del Research Corp.), St. Louis, Missouri, 1985.
17. G.I. Barenblatt, "The Mathematical Theory of Equilibrium Cracks in Brittle Fracture," Adv. Appl. Mechanics 7 55-129 (1962).
18. I.N. Sneddon and M. Lowengrub, "Crack Problems in the Classical Theory of Elasticity". Wiley, New York (1969).
19. Y.-W. Mai and B.R. Lawn, "Crack Stability and Toughness Characteristics in Brittle Materials," Ann. Rev. Mater. Sci. 16 415-39 (1986).

20. J.R. Rice, "Mathematical Analysis in the Mechanics of Fracture," in *Fracture II*, edited by H. Liebowitz, Academic Press, New York 1968.
21. B.R. Lawn and T.R. Wilshaw, Fracture of Brittle Solids; Ch. 6. Cambridge University Press, London, 1975.
22. R. Knehans and R.W. Steinbrech, "Memory Effect of Crack Resistance during Slow Crack Growth in Notched  $\text{Al}_2\text{O}_3$  Bend Specimens," J. Mat. Sci. Lett. 1[8] 327-29 (1982).
23. B. Cotterell and Y.-W. Mai, "Modelling Crack Growth in Fibre-Reinforced Cementitious Materials," Materials Forum 11 341-51 (1988).
24. R.M.L. Foote, Y-W. Mai and B. Cotterell, "Crack Growth Resistance Curves in Strain-Softening Materials," J. Mech. Phys. Solids 34[6] 593 (1986).
25. P. Chantikul, S.J. Bennison and B.R. Lawn, "Role of Grain Size in the Strength and R-Curve Properties of Alumina," J. Am. Ceram. Soc., in press.
26. B.N. Cox and D.B. Marshall, "Stable and Unstable Solutions for Bridged Cracks in Various Specimens, submitted to *Acta Metall.*

## FIGURES

1. Schematic of device for in situ SEM observations of fracture specimen under load.  $T$  = piezoelectric translator,  $C$  = load cell,  $P$  = pivot arms,  $L$  = loading arms,  $S$  = specimen. Solid circles indicate joints between pivot arms and loading arms and between pivot arms and base.
2. SEM micrograph showing grain-bridging element at crack-interface  $1260 \mu\text{m}$  behind the crack tip. Note resolution of crack-opening displacement.
3. SEM micrographs showing another grain-bridging element at crack-interface at two stages in the loading, (a)  $660 \mu\text{m}$  and (b)  $1190 \mu\text{m}$ , behind the crack tip.  $P$  and  $S$  denote frictional contact points.
4. Schematic of compact-tension specimen. Notch length  $c_0$ , crack extension  $\Delta c$ . Crack profile measured by COD  $2u$  at distance  $x$  behind crack tip,  $2u_0$  at crack mouth. Bridging tractions  $p(x')$  act to restrain crack.
5. Measured COD at crack interface in soda-lime glass, for compact-tension specimen ( $\Delta c = 1.9 \text{ mm}$ ). Different symbols designate separate crack runs. Error bars represent systematic uncertainty in COD measurement ( $\approx \pm 70 \text{ nm}$ ). Curve is Irwin parabola from Eq. 1 at  $K_A = 0.56 \text{ MPa}\cdot\text{m}^{1/2}$ .
6. Measured COD at crack interface in alumina, compact-tension specimen ( $\Delta c = 1.9 \text{ mm}$ ). Fitted profile (solid curve) from Eq. 2, Irwin parabolas for  $K_A = 4.6 \text{ MPa}\cdot\text{m}^{1/2}$  and  $T_0 = 2 \text{ MPa}\cdot\text{m}^{1/2}$  (dashed curves) from Eq. 1.

7. COD at crack mouth as a function of crack extension for alumina compact-tension specimen.
8. Bridging stress functions, (a)  $p(x')$  for compact-tension crack, and (b) corresponding  $p(u)$ , for alumina. Note cutoff in plots at  $\Delta c = 1.9$  mm,  $2u_0 = 1.3 \mu\text{m}$ , indicating limits of crack size over which COD data were obtained in our experiments. Dashed line in (b) is evaluation from indentation-strength data on other aluminas [25].
9. Crack-resistance curves, (a)  $R(u)$ , and (b)  $R(\Delta c)$  for compact-tension crack ( $\Delta c = 1.9$  mm) for alumina.

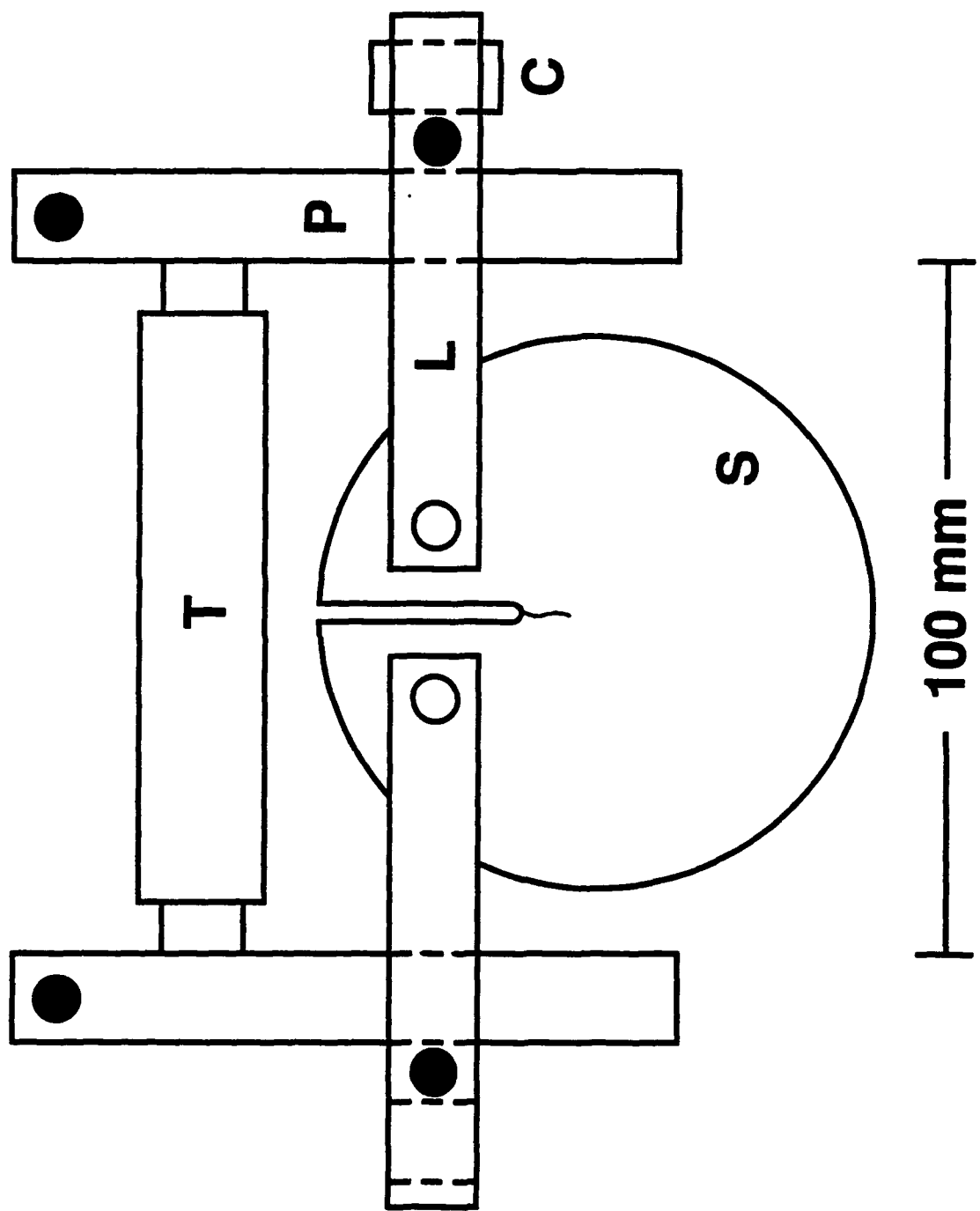
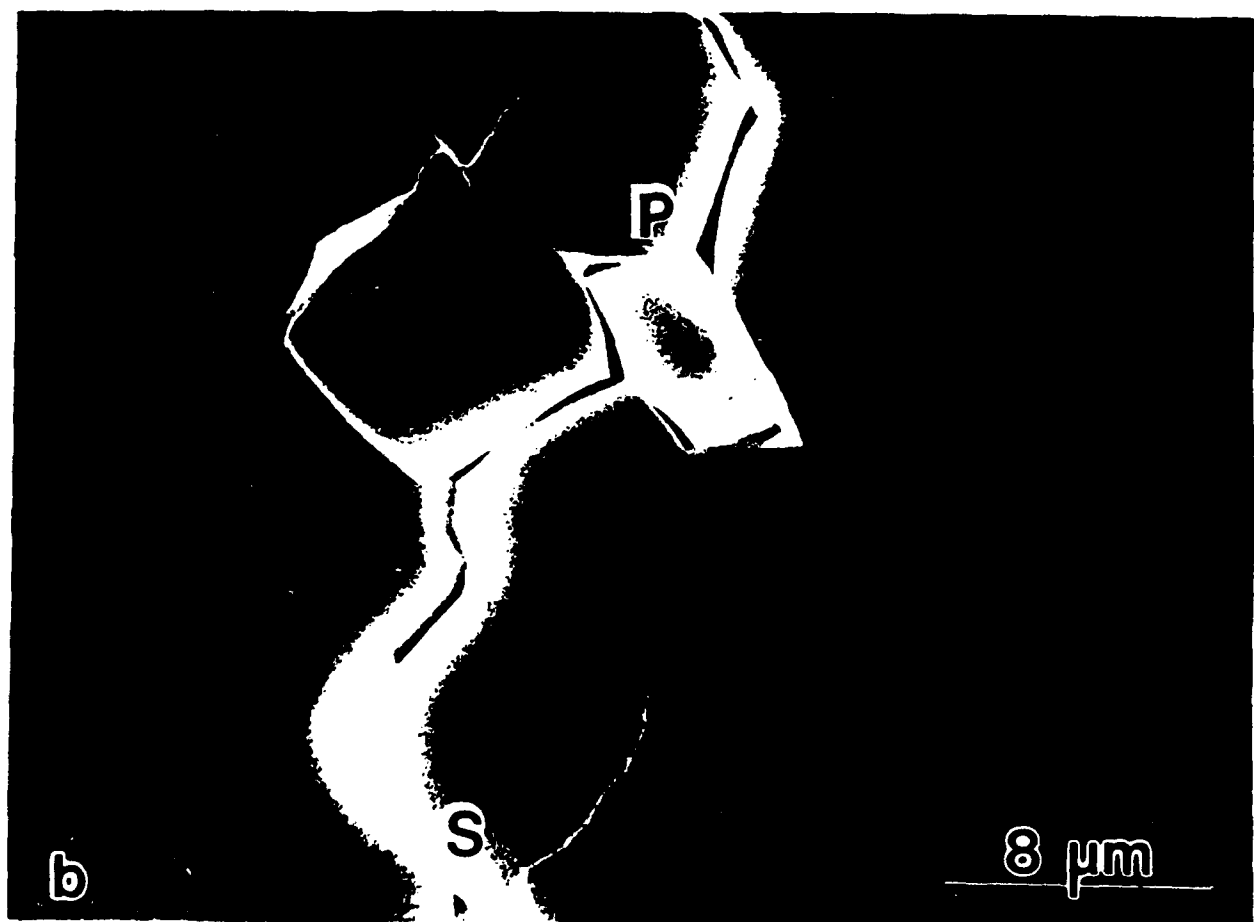
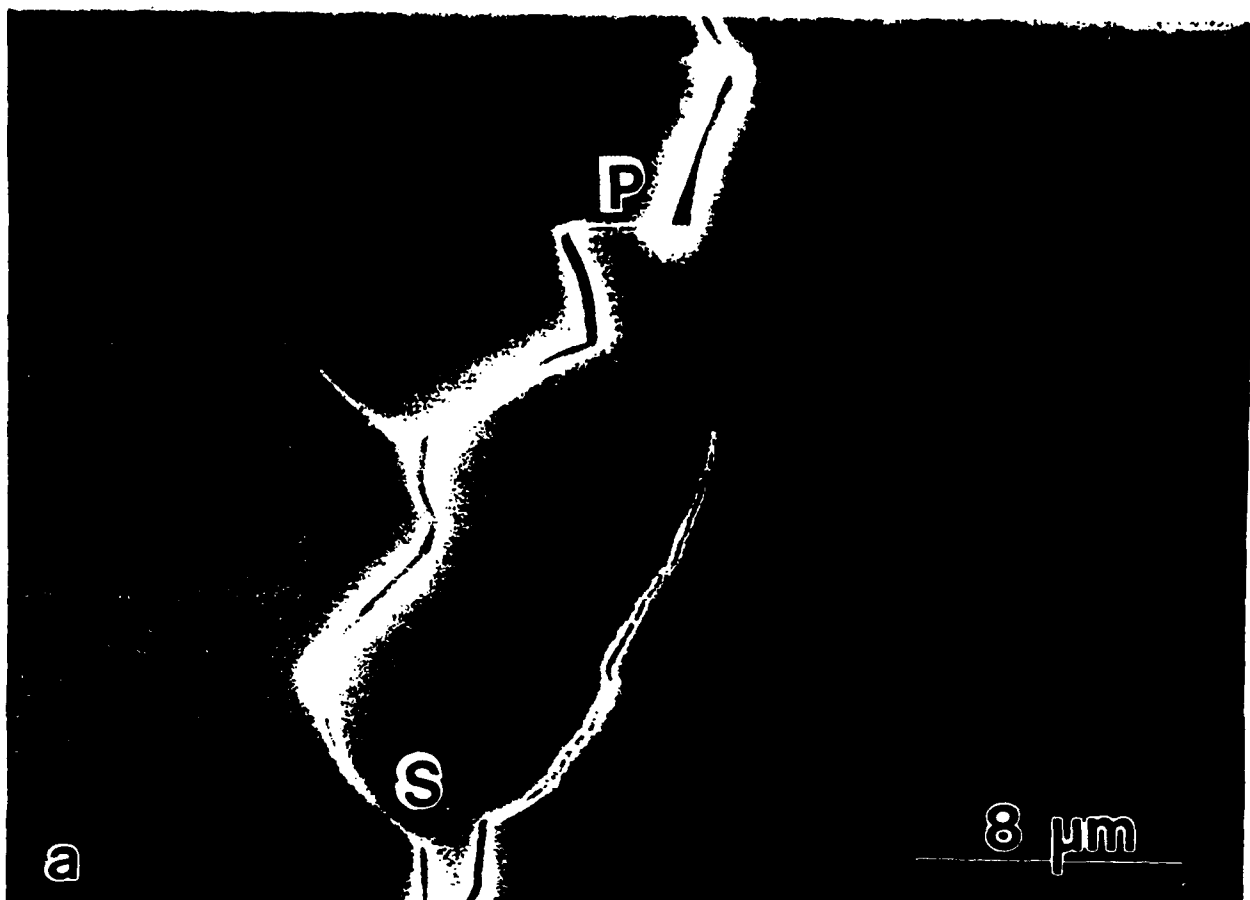


Fig. 1



Fig. 2



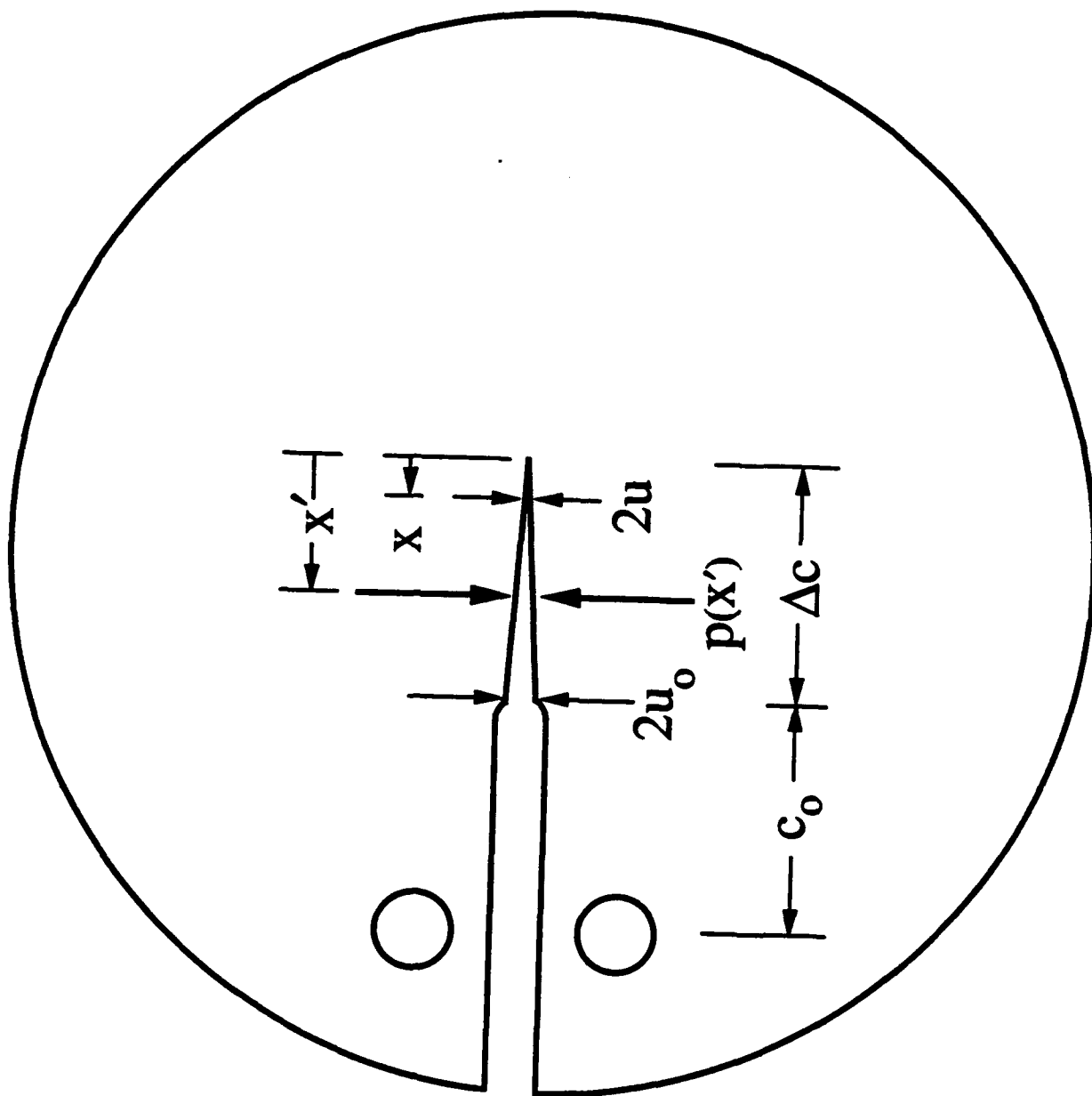


Fig. 5

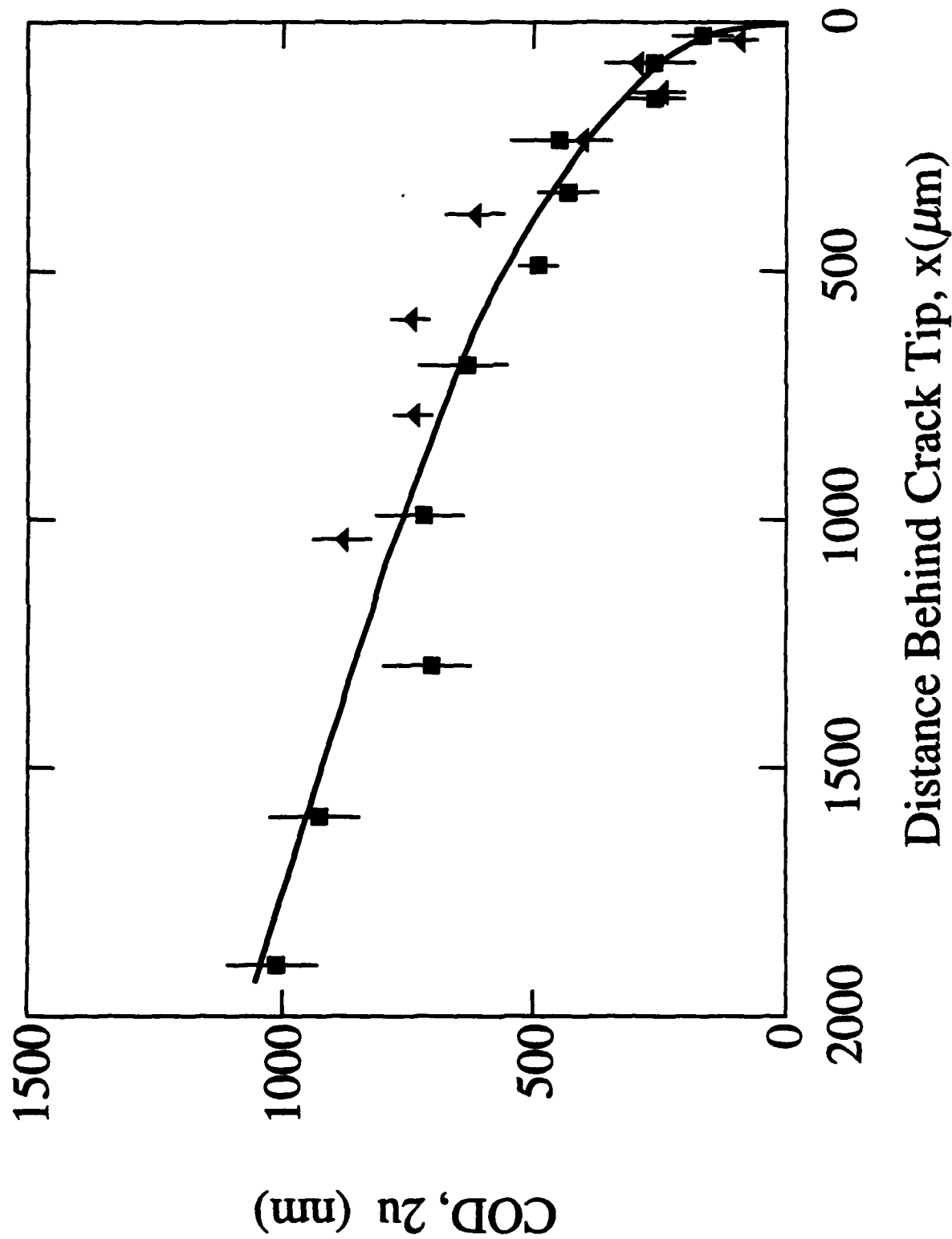
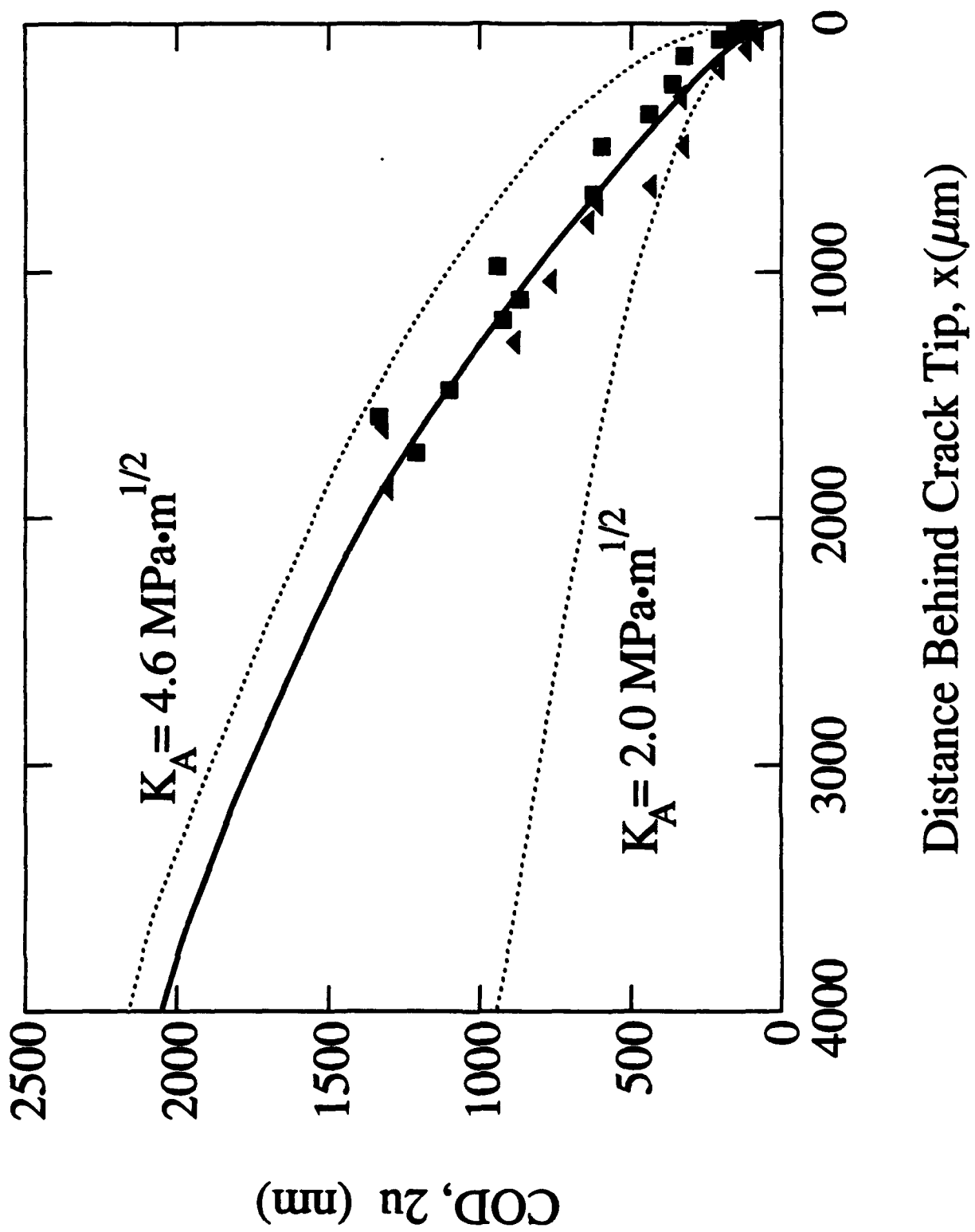
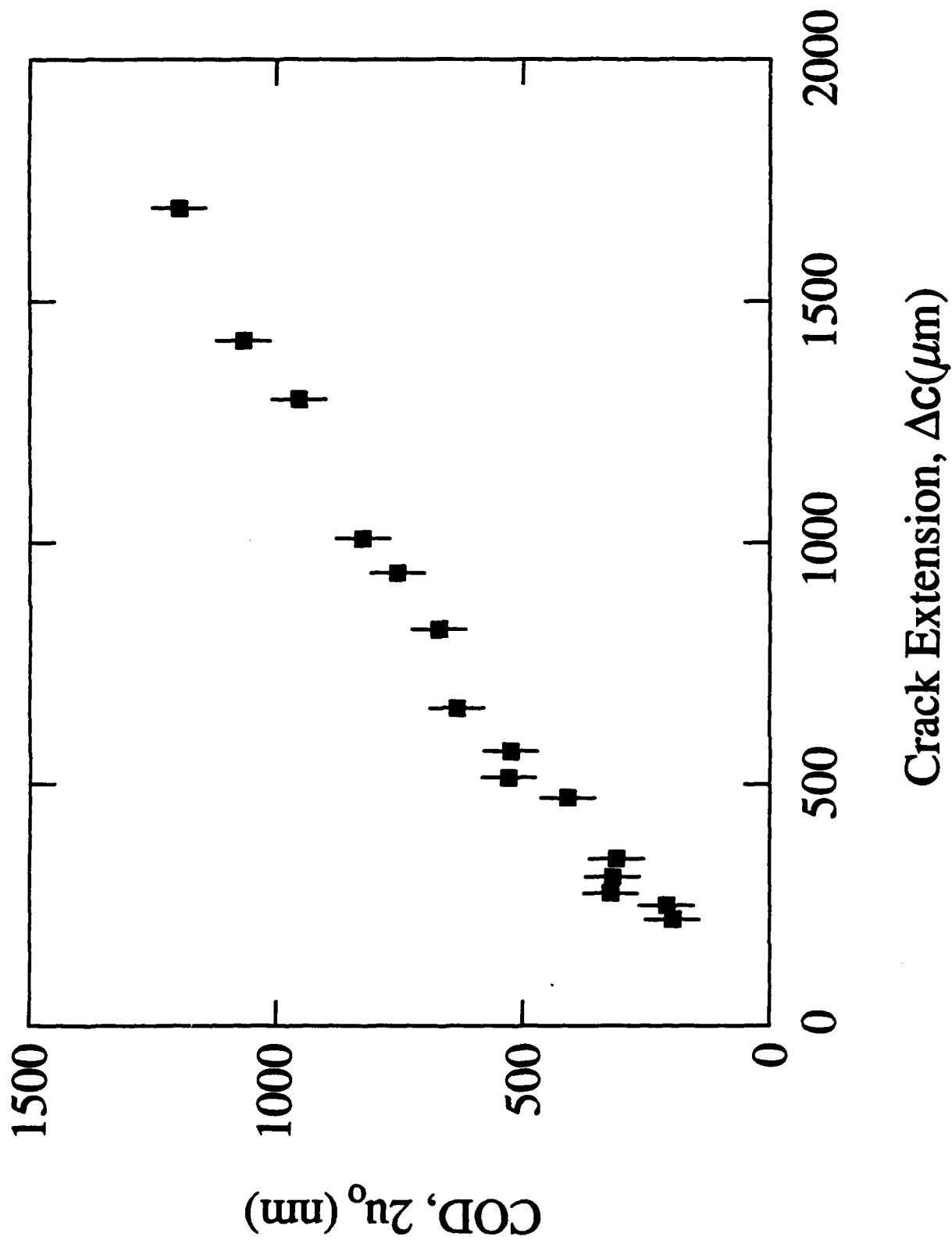


Fig. 6





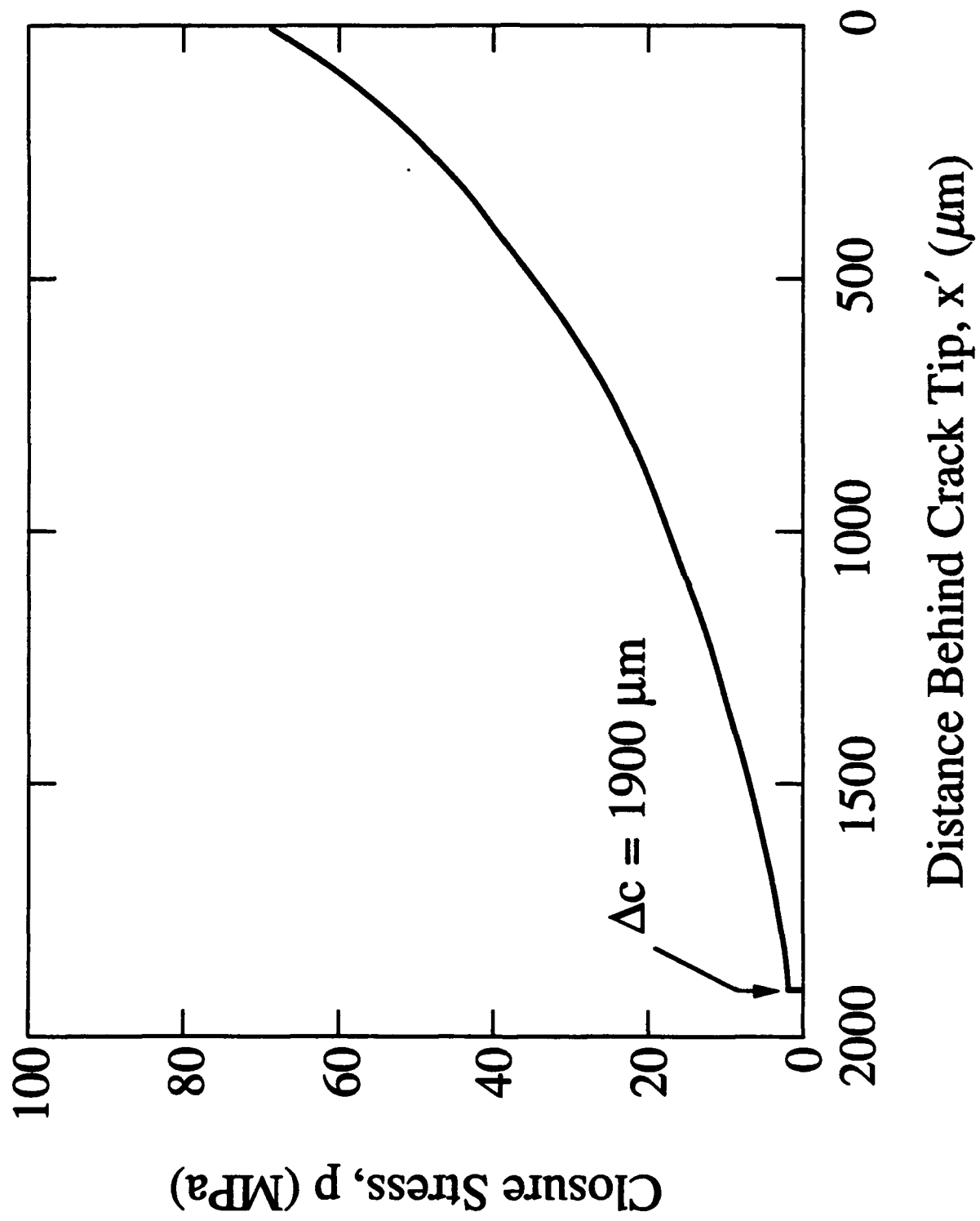


Fig. 8a

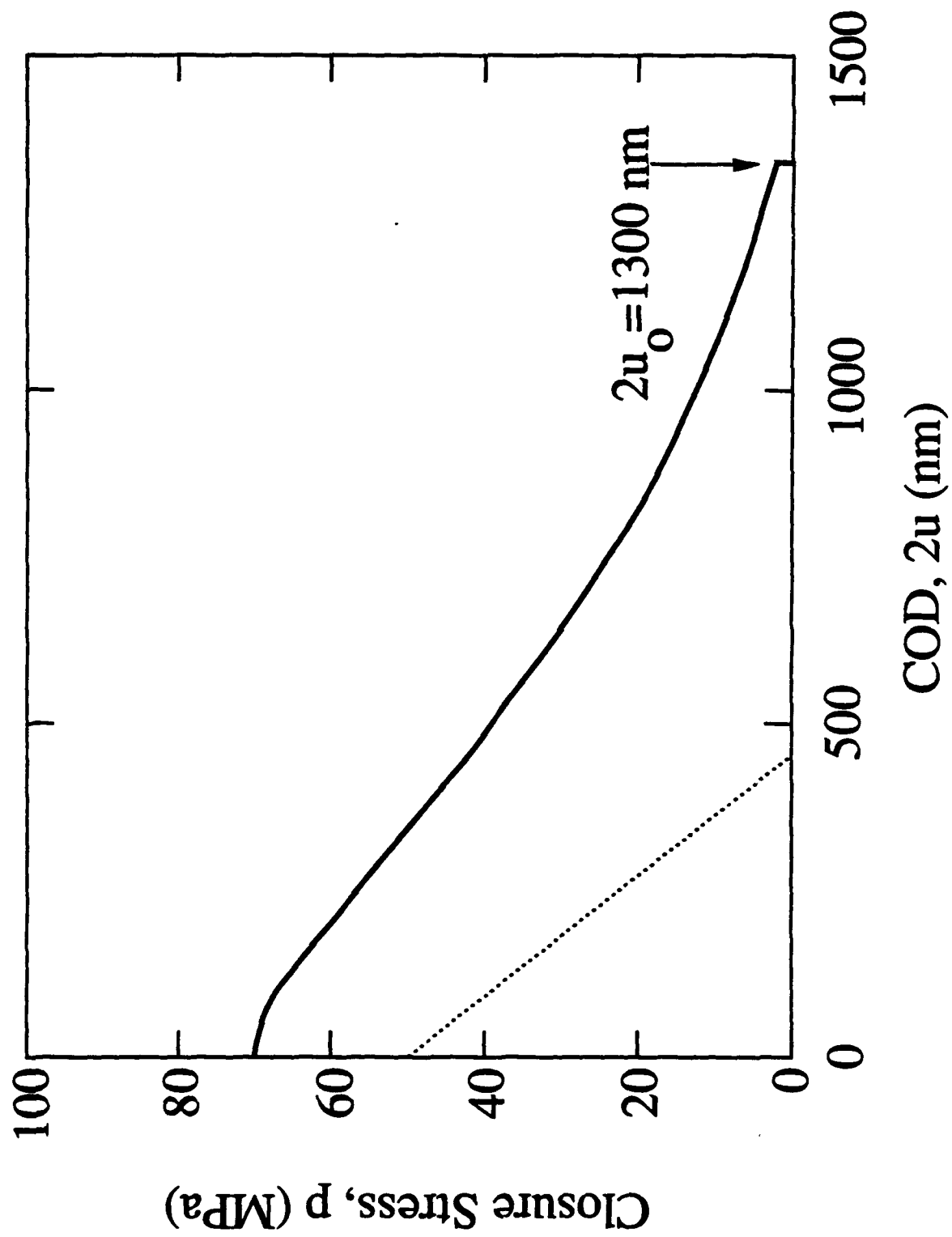


Fig. 86

Fig. 9a

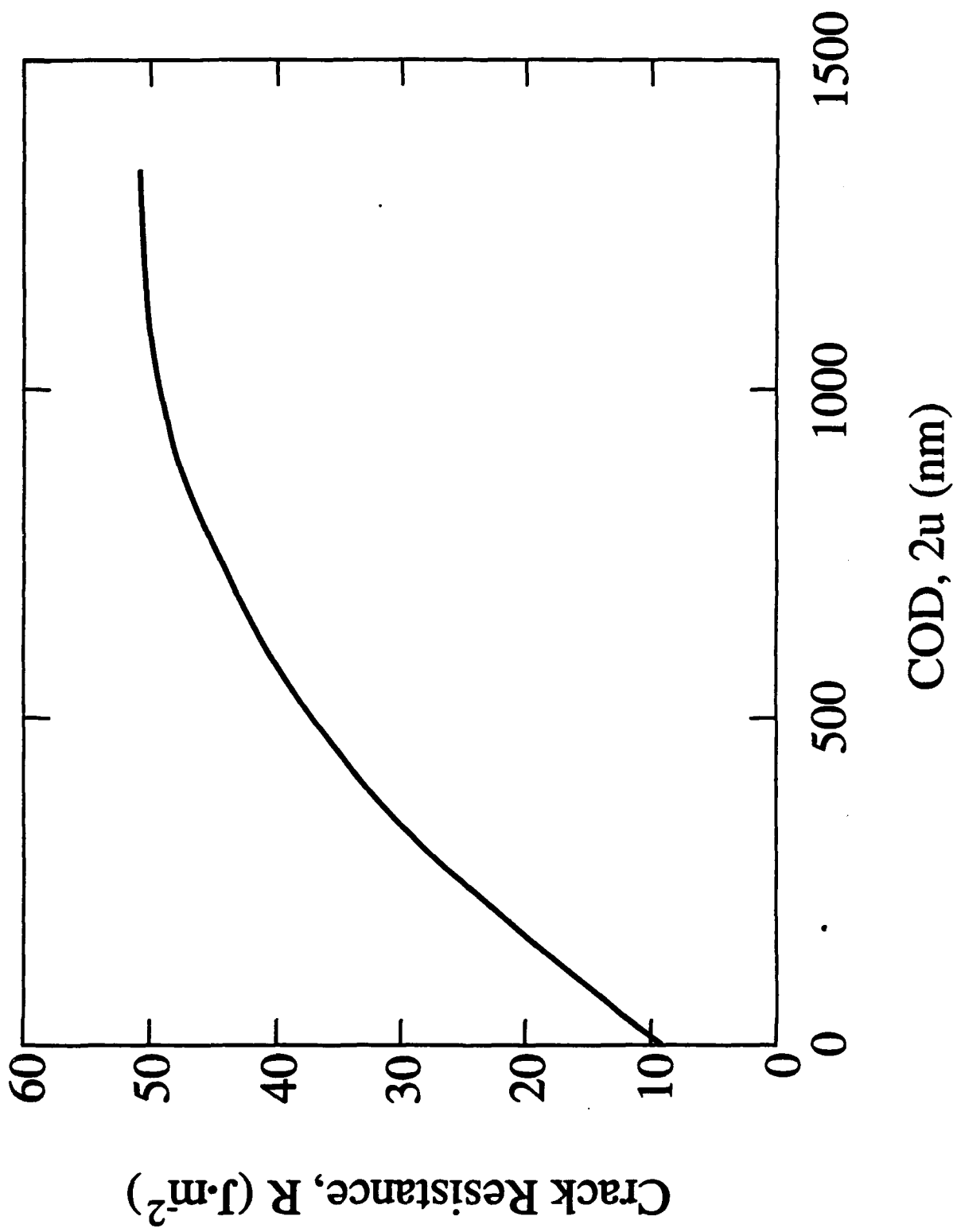
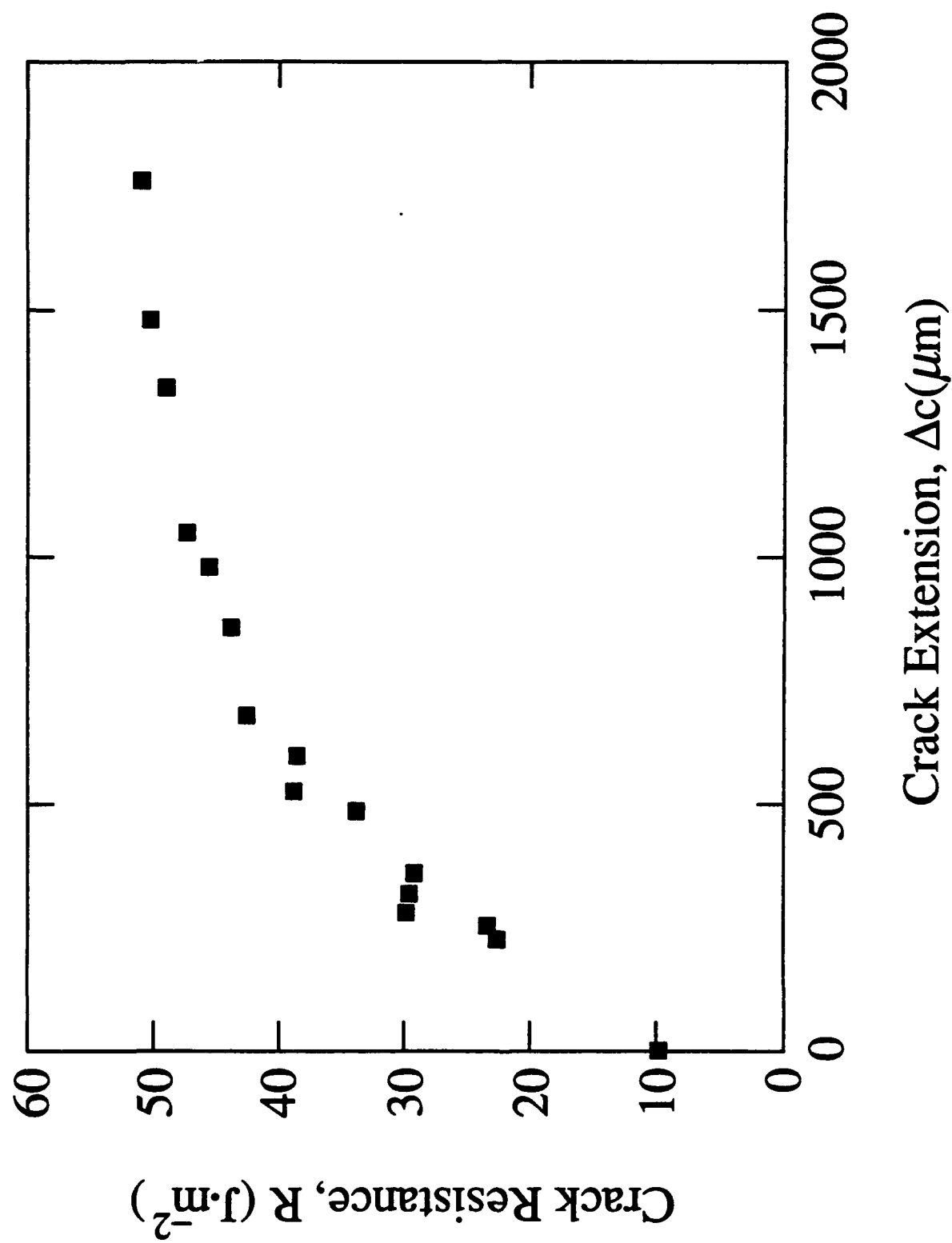


Fig. 9



**A LOADING DEVICE FOR FRACTURE TESTING OF COMPACT  
TENSION SPECIMENS IN THE SCANNING ELECTRON MICROSCOPE**

Jürgen Rödel<sup>1</sup>, James F. Kelly<sup>\*</sup>, Mark R. Stoudt and Stephen J. Bennison

Ceramics Division  
National Institute of Standards and Technology  
Gaithersburg, MD 20899

1. Guest Scientist on leave from the Department of Materials Science  
and Engineering, Lehigh University, Bethlehem, PA 18015.

**Abstract**

A loading device for performing fracture experiments on compact tension specimens in the SEM has been designed. Its key elements are a piezoelectric translator for applying controlled displacements to the loading points on the specimen and a load cell to measure applied loads. The effective transmission of displacement from the piezoelectric driver to the specimen was found to be the major mechanical design problem. The peripheral equipment includes a function generator and a high voltage amplifier that drives the piezoelectric translator as well as a video overlay and standard video equipment to record the image continuously during the course of the experiment. A case study on alumina describes qualitative observations on the toughening mechanism, crack-interface bridging, operating in this material. Quantitative information pertaining to the closure stresses associated with this toughening mode can be obtained by measuring the crack profile.

**Introduction**

The science of fractography, viz, the postmortem observation of features associated with fracture, is an important element of any investigation into mechanical behavior of materials [12]. Fractography embodies a variety of techniques which can provide invaluable insights into fracture modes, loading histories and the role of microstructure in failure for a range of different materials.

The postmortem nature of fractography, however, ultimately places a restriction on its utility. Events influencing fracture which leave no visible traces after specimen failure go undetected. A case in point is the phenomenon of crack-interface bridging which is responsible for rising crack resistance (R-curve) behavior in many monolithic ceramics such as aluminum oxide [9,11,15,16]. In this mechanism, intact grains well behind the primary crack tip bridge the crack walls, shield it from the applied stress intensity field ( $K_a$ ) and lead to increased crack resistance (toughness) with crack extension; after failure the bridges have been destroyed. Identification of grain bridging has only been attained through careful *in situ* studies of crack growth using optical microscopy [16]. Recognition that the toughness behavior of many ceramic systems may be determined by grain bridging and other wake-associated mechanisms [6] has highlighted the importance of *in situ* observations of fracture events.

The aim of the present work is to develop a fixture for *in situ* testing of materials in the scanning electron microscope (SEM). The superior resolution afforded by the SEM provides two significant advantages over existing optically based systems. First, greater detail of crack - microstructure interactions, such as grain bridging, can be obtained. Such information is critical to the development of models describing the toughening and R-curve properties of ceramics [4]. Second, quantitative information on the stress intensity fields ( $K$ -fields) can be gained from direct measurements of crack profiles. In the case of ceramics, crack opening displacements typically range from 0  $\mu\text{m}$  (at the crack tip) to 1-2  $\mu\text{m}$  (at the crack mouth) and, as such, cannot be readily

**KEY WORDS:** Scanning electron microscopy, cracks, crack profile, *in-situ*, fracture toughness, microstructure, alumina

\*Address for correspondence:  
James F. Kelly,  
National Institute for Standards and Technology  
Bldg. 223, Rm. A256  
Gaithersburg, MD 20899  
Phone No. (301) 975-5794

measured by optical techniques.

A number of SEM-based testing systems have been described before, designed for tensile loading of test bars [5], four-point bending [8], double torsion [17] and wedge-loaded DCB-type specimen [19]. Special requirements, in particular the ability to measure the propagation and the profile of long cracks, necessitated the development of a loading stage for compact tension specimens. Profile measurements of long cracks in particular, allow a calculation of the stress-separation function [14], which is the key material characteristic determining R-curve behavior [4].

In this paper a design for such an SEM-based testing system is presented. Mechanical, electrical and imaging requirements are described, and results from a case study of crack growth in aluminum oxide are detailed to demonstrate the capabilities of the loading stage.

#### Instrument Design

The fracture device was designed for use in an AMRAY<sup>1</sup> SEM<sup>2</sup>. This particular instrument offers the advantage of a large specimen chamber (more than 30 cm in each dimension) and allows easy access to the SEM stage which is connected to the door and therefore swings out when the chamber is opened.

For this case study tests were run at 20 kV accelerating voltage with the sample surface perpendicular to the beam.

#### Mechanical Considerations

The specimen geometry of choice is compact tension (round or rectangular) according to the ASTM E 399 specification [1]. This geometry was chosen for several reasons. First, the stress intensity solutions for the applied stress field ( $K_I$ ) are available. Second, for materials, like alumina, which experience closure forces due to crack-interface bridging in the crack wake [15,16], the additional requirement, that the crack be long compared to the bridging zone, can be satisfied with this geometry. Then  $K_I$  values can readily be calculated from measurements of the applied load and crack length. Third, the crack path is stable [2] (shows no deviation from a straight line). Fourth, disk-shaped specimens are readily prepared using conventional ceramics processing.

Figure 1 shows schematically the loading stage and Figure 2 is a photograph of the fixture. The heart of the device is a

<sup>1</sup> AMRAY 1830, Amray Inc., Bedford, MA.

<sup>2</sup> Certain commercial equipment are identified in this paper in order to adequately specify the experimental procedure. Such identification does not imply recommendation or endorsement by the NIST, nor does it imply that the equipment identified is necessarily the best available for the purpose.

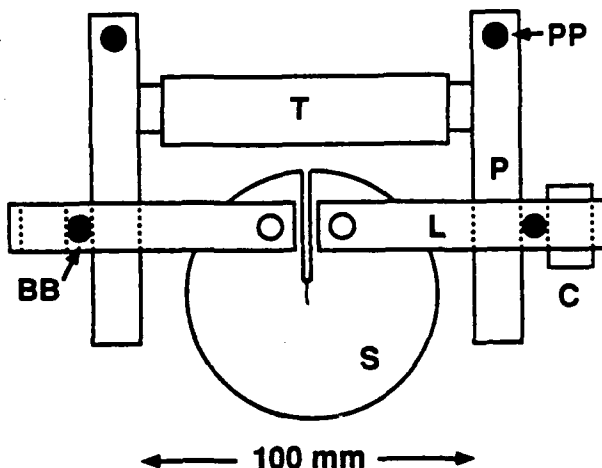


Figure 1. Schematic of device for in situ SEM observations of compact tension specimen. T = piezoelectric translator, C = load cell, P = pivot arms, L = loading arms, PP = pivot point, BB = ball bearing and S = specimen.

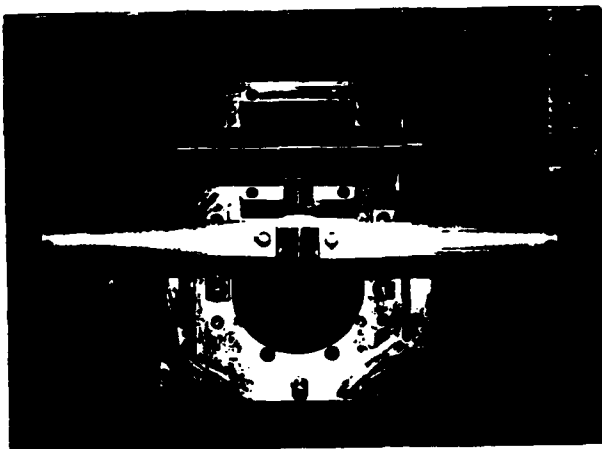


Figure 2. Photograph of the loading device containing disc compact tension specimen.

piezoelectric translator (T)<sup>3</sup> (see also [8]) capable of displacements up to 85  $\mu$ m and maximum force of 1,000 N when a voltage of 1 kV is applied. The force is transmitted to the specimen via a system of two pivot arms (P) and two loading arms (L). The pivot arms rotate on pivot points (PP) which are rigidly attached to a rectangular baseplate. The loading arms

<sup>3</sup> PI Model P-245.50, Physik Instruments, D7571 Waldbronn, FRG

connect to the pivot arms via two ball bearings (BB) which allow rotational alignment of the system and prevent the application of bending moments to the specimen. A strain gauge load cell<sup>4</sup> is placed in one loading arm and allows monitoring of the applied load between 0 and 2,300 N.

The primary mechanical design requirement is the efficient transmission of displacement from the piezoelectric translator to the specimen. Losses in displacement due to the compliance of the loading train are minimized by constructing the elements from (non-magnetic) stainless steel and fabricating the pivot points to tolerances of  $-25 \mu\text{m}$ . Despite these precautions displacement losses were considerable in our early designs. The final arrangement, presented in Figure 1, places the piezoelectric translator between the pivot points (PP) and the load application points (BB) to the loading arm (L). At first glance this may appear to give a poor mechanical advantage, with the force applied through the piezoelectric translator being reduced to 40% at the loading arms. However, the design ensures that sufficient displacement is available at the crack mouth to drive cracks in ceramics of this specimen geometry. Specimens are also routinely prestressed with two screws, which link the piezoelectric translator to the pivot arms, before placing the loading device into the SEM chamber. The load transmission characteristics result in mechanical testing effectively in a constant load mode [2] due to the stored elastic energy in the loading train.

If the loading stage is used for cyclic loading applications, a slight specimen shift is noticeable. This displacement was less than 6  $\mu\text{m}$ .

#### Electrical Considerations

The supply voltage for the piezoelectric translator, and the supply and signal voltages for the load cell (5V power supply and standard voltmeter) are connected into the specimen chamber via three electrically isolated BNC type feedthroughs mounted on a side port of the SEM. The piezoelectric translator is driven by a high voltage amplifier<sup>5</sup> which, when fed with a function generator, affords application of controlled (e.g. cyclic) loading. The relatively large capacitance (113 nF) of the translator in combination with the low current output of the power supply (1.8 mA) places an upper bound on the range of available frequencies ( $\approx 2 \text{ Hz}$ ).

<sup>4</sup> Sensotech, LFH-71, Sensotech, Columbus, OH 43212

<sup>5</sup> PI Model P-263, Physik Instruments, D7517 Waldbronn, FRG

<sup>6</sup> VT0232 Video Text Overlay, Linkam Scientific Instruments Ltd., Tadworth, UK.

#### Imaging requirements

The physical characteristics of the compact tension test fixture along with the requirement for real time imaging act to limit the image resolution in three ways: increased working distance, reduced vibrational stability, and higher specimen current. The piezoelectric driver and raised pivot rods require operating at a working distance of 30 mm to avoid contacting the secondary electron detector and the final lens. Since the best resolution obtained on this microscope is 5 nm at the minimum working distance of 5 mm, this increase in working distance alone decreases the secondary image resolution by a factor of about six. Additionally, the requisite stiffness for transmitting the load from the driver, through the loading and pivot arms, to the test specimen with minimal flexure of the arms, necessitates a large mass of nearly two kilograms which must be supported by the SEM stage. This increased load on the stage, together with the requirement that the test specimen be minimally constrained, significantly increases the vibrational sensitivity of the system. An improvement of the fixture support has been achieved by bolting the fixture to the SEM stage in addition to having the standard pin support. The third factor influencing the electron spot size is the beam current. A compromise between resolution and the ability to follow crack propagation in real time resulted in the use of a 200  $\mu\text{m}$  final aperture with the condenser lens adjusted to give a beam current of 100 pA. The combination of these operating conditions limits the resolution of the secondary image to approximately 70 nm.

Prior to full crack formation, highly polished, gold-coated specimen surfaces provide little contrast for secondary electron imaging. The charging of newly exposed non-coated material subsequent to crack extension, however, provides a readily detectable secondary electron signal. For more complex microstructures, backscattered electron imaging has proven useful in identifying the crack path relative to specific microstructural phases or grain boundaries. However, the relatively slow response time of the solid state backscatter electron detector, requiring scan times of at least 30 s/frame make this mode impractical for live time monitoring of crack propagation.

The rapid scan mode of the AMRAY Model 1830 SEM operates at a scan rate of 5 frames/s. The selected signal is processed through an integral 512 by 512 pixel frame buffer which displays the image at a standard TV rate of 30 frames/s. This capability for continuous display at TV rate enables the direct recording of the secondary image using a video cassette recorder (VCR). The SEM image is superimposed with the load cell output voltage using a video text overlay<sup>6</sup>. Photographic recording via instant film can also be done, either directly from the frame buffer, or by bypassing the buffer to obtain an increased line density in the recorded image.

Case Study

We proceed to illustrate the capabilities of the fracture device by discussing some results from a case study on crack propagation in alumina.

An alumina disk, 4 mm thick and with a diameter of 100 mm, was prepared by hot pressing alumina powder<sup>7</sup> for 3 hours at 1650°C under a uniaxial pressure of 35 MPa. The pressed slab was found to be pore-free with an average grain size of 11  $\mu\text{m}$ . It was then ground to 1 mm thickness and polished with diamond pastes of grade 15  $\mu\text{m}$  down to 1  $\mu\text{m}$ . A compact tension specimen was machined by drilling holes for the loading arms and cutting a notch. The stability of the sample with respect to crack propagation was enhanced by extending the notch at an angle of 28° to the specimen surface, which gave the geometry of a quasi-chevron notch, with the notch being extended about 2 mm on the unpolished (lower) surface. A Vickers hardness indentation ( $P = 50$  N) was placed about 200  $\mu\text{m}$  in front of the notch on the polished surface. The radial cracks emanating from the elastic-plastic zone in the direction of the notch were then extended under tension with the loading device placed on an optical microscope. Subsequently, the indented region was cut out to leave a precrack of about 100  $\mu\text{m}$  length. After the first crack propagation run (for  $\approx 2\text{mm}$ ) the specimen was removed and resawn again, for second and third runs. Etching to reveal the microstructure of the specimen was purposely avoided, since cracks following a grain boundary groove are difficult to detect in the crack tip region.

Crack propagation under applied tensile loading in the SEM was found to be stable in the quasi-chevron region. The load was increased until crack extension occurred (typically for 10 - 50  $\mu\text{m}$ ) and the crack arrested again. The required loading increments for crack instability to occur were found to be between 5 and 15 N with the total applied loading in the range between 200 and 300 N.

Microscopical observations during crack extension are classified here into two categories: events at the crack tip and events in the crack wake. In the first category, the mode of crack propagation, discontinuous in nature, in contrast to slow crack growth in glass in high vacuum [18], can be monitored. The occurrence of subsidiary cracking - either secondary cracking or microcracking in a zone [7] - can also be followed while the crack passes through a given region in the material. Microcracking in particular has been a focal point of recent considerations and has been invoked as one of the possible toughening mechanisms in ceramics [6]. The R-curve in alumina, in particular, was originally

attributed to this mechanism [13]. With the resolution now available using the loading device in the SEM, the creation of microcracks (of lengths down to at least one grain facet and openings down to about 50 nm) can be detected. No such microcracking was observed in the particular alumina studied in this case.

Observations of the crack wake focus on bridge evolution [14]. A bridge is here defined as any microstructural element connecting the crack faces which gives rise to a closure force. An example is given in Fig. 3 a,b with a closure force across the crack surfaces being applied at A. This force causes the secondary crack at location B to open. With further crack propagation the opening of the primary crack increases, the closure force diminishes and the secondary crack at B closes (Fig. 3b). Note also the creation of a new secondary crack at position C in Fig. 3b. Observations such as the one described help understand the origin of closure forces in the crack wake. The crack opening displacement of secondary cracks as a function of the opening of the primary crack can be utilized to measure the relative closure stress at given regions while the crack propagates through the material [14].

The existence of closure forces in the crack wake can further be demonstrated and, in fact, numerically evaluated by measuring the crack opening (COD) as a function of distance from the crack tip [3].

Crack opening displacements are measured by imaging cracks at a magnification of 30,000, taping the image and, after the experiment, measuring the opening from the video monitor. In ceramics we are typically concerned with crack opening displacements in the range of 50 to 2000 nm. Since standard optical techniques are not able to provide this type of resolution, SEM techniques are required. An accuracy of about 70 nm is currently obtained, although relative measurements can be made to 30 nm precision.

An example of three such measurements is given in Fig. 4 for the alumina studied. The profile is found to be linear in first approximation, which is in contrast to the parabolic profile of cracks with stress-free surfaces [10]. Closure forces arising from discrete bridges are commonly combined in a continuum description to give a continuous closure stress acting on the crack faces. This closure stress can be given as a function of distance from the crack tip [3], and, more fundamentally, as a function of the local crack opening displacement. If this description is used, the experimentally obtained profile can be related through an integral equation [14] to the closure force as a function of distance from the crack tip.

An additional route to obtaining quantitative information on the micromechanics of microstructural elements in the crack wake is given by recording crack opening displacements during loading/unloading. These measurements give further insight about the nature of the closure forces (frictional, elastic). In the

<sup>7</sup> Sumitomo AKP-HP grade (99.995% pure, 0.5  $\mu\text{m}$  crystallites), Sumitomo Chemical America, New York, NY

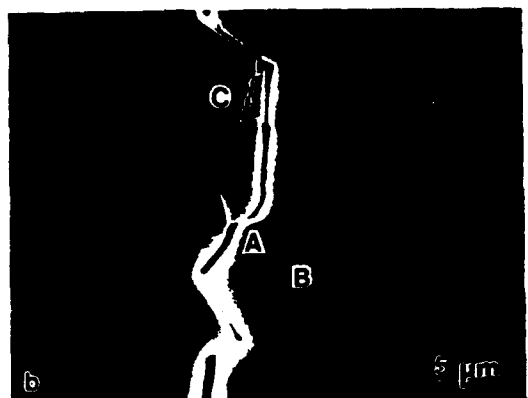
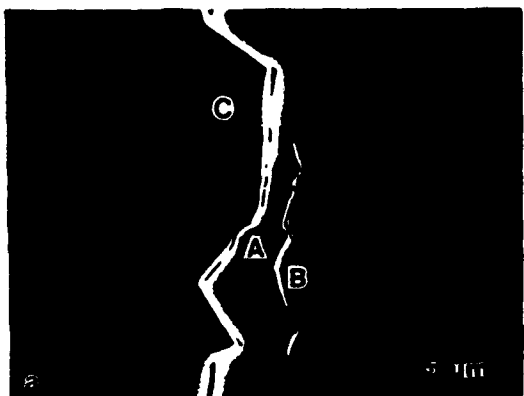


Figure 3. SEM micrographs of region showing closure force at A and secondary cracks at B and C; a) 330  $\mu\text{m}$  behind the crack tip and b) after further loading the crack grows and the region is now 660  $\mu\text{m}$  behind the crack tip.

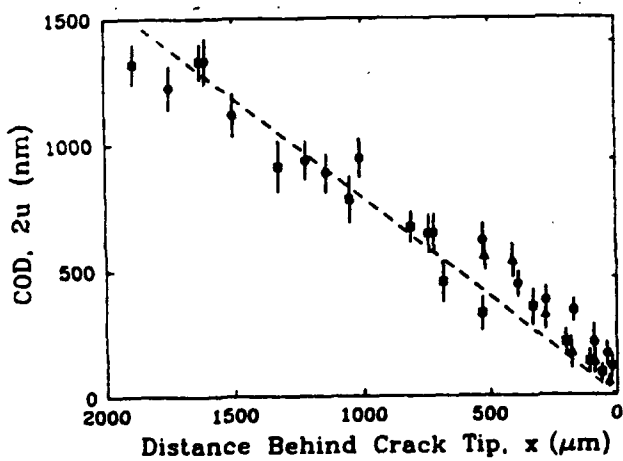


Figure 4. Examples of measured crack opening displacements as function of distance from the crack tip. Different symbols designate different runs; dashed line gives empirical linear fit.

case of the alumina studied, complete closure at a residual applied force was found. An example of a microstructural element bridging the crack faces of an equilibrated crack and a closed crack (in this case, no applied loading) is given in Fig. 5 a,b. The crack in Fig. 5b is virtually invisible and can only be visualized by following the trace of grains released from their original positions.

The case study on alumina thus demonstrates the use of the loading stage and the ability to gain valuable qualitative and quantitative information on the micromechanics operative in the crack wake and, possibly, at the crack tip. The experimental observations focus on the occurrence of microcracks or grain bridging (in other cases this might be fiber, whisker or ductile ligament bridging). Quantitative measurements focus on the crack opening displacement as a function of either applied load or distance from the crack tip.



Figure 5. SEM micrographs of areas 1000  $\mu\text{m}$  behind the crack tip showing grain release from the specimen surface; a) maximum applied load corresponding to crack equilibrium, b) zero applied load.

### Future Opportunities

The loading device in its current developmental stage is well suited for *in situ* studies of toughening mechanisms such as grain bridging, ductile ligament or whisker toughening as well as microcrack toughening.

Future advancements are sought in the areas of specimen geometry, and mode of applied loading.

In order to use K-field solutions for the standard geometries (ASTM), it is necessary to propagate a crack through a constant-thickness region. The preliminary aid of a quasi-chevron geometry should therefore be eliminated.

*In situ* observations during cyclic fatigue are currently under way. The evolution of bridges after given numbers of cycles can be monitored. The closure forces in the crack wake after cyclic loading can also be obtained by evaluating the crack opening displacements.

Further modifications of the fracture device are envisioned to provide the capability of compressive loading and therefore, also compression - compression fatigue. This would then allow inclusion of 4-pt. bend fixtures as an additional option. A separate biaxial flexure stage is currently under construction. This new device will make it possible to test indentation cracks and will thus give an opportunity to investigate short vs. long crack behavior in the SEM.

### Summary

A fracture device which allows *in situ* observations of crack propagation in brittle solids under tensile loading has been described. It affords the opportunity to study the micromechanics of microstructural elements, which, acting as an ensemble, effect an increase in toughness over samples without special toughening features. The ability to measure applied load, crack opening and crack length makes the loading stage more than an *in situ* device for qualitative observations, but allows its use as a universal fracture testing machine. Quantitative measurements of the crack opening displacement allow evaluation of the closure stresses acting in the crack wake and enable a further characterization of the closure stress. Future opportunities include cyclic fatigue testing, compressive loading and biaxial flexure.

### Acknowledgements

We are indebted to Brian R. Lawn for suggesting this project and continued discussions. We also wish to thank Michael A. Hall for his excellent machining work. Funding was provided by the U.S. Air Force Office of Scientific Research.

### References

- [1] American Society for Testing and Materials. (1989). E-399-83. pp. 506-508. A.S.T.M. Philadelphia.
- [2] Atkins AM, Mai Y-W. (1985). Elastic and plastic fracture. pp. 198-219. Ellis Harwood Limited.
- [3] Barenblatt GI. (1962). The mathematical theory of equilibrium cracks in brittle fracture. *Adv. Appl. Mech.* 7 55-129.
- [4] Bennison SJ, Lawn BR. (1989). Role of interfacial grain-bridging sliding friction in the crack-resistance and strength properties of nontransforming ceramics. *Acta metall.* 37 [10] 2659-2671.
- [5] Davidson DL, Nagy A. (1978). A low-frequency cyclic-loading stage for the SEM. *J. Phys. E: Sci. Instrum.* 11 207-210.
- [6] Evans AG. (1990). Perspective on the development of high-toughness ceramics. *J. Am. Ceram. Soc.* 73 [2] 187-206.
- [7] Evans AG, Faber KT. (1984). Crack-growth resistance of microcracking brittle materials. *J. Am. Ceram. Soc.* 67 [4] 255-260.
- [8] Frei H, Grathwohl G. (1989). Development of a piezotranslator-based bending device for *in situ* SEM investigations on high-performance ceramics. *J. Phys. E: Sci. Instrum.* 22 589-593.
- [9] Hübner H, Jillek W. (1977). Sub-critical crack extension and crack resistance in polycrystalline alumina. *J. Mat. Sci.* 12 117-125.
- [10] Irwin GRI. (1958). Fracture. *Handbuch der Physik.* 6 551-590.
- [11] Knehans R, Steinbrech R. Memory effect of crack resistance during slow crack growth in notched  $Al_2O_3$  bend specimens. *J. Mat. Sci. Lett.* 1 327-329.
- [12] Rice RW. (1988). Perspective on fractography. In: *Fractography of glasses and ceramics*. Varner JR, Frechette VD, Eds. pp. 3-53.
- [13] Rice RW, Freiman SW. (1981). Grain-Size Dependence of Fracture Energy in Ceramics: II, A Model for Noncubic Materials. *J. Am. Ceram. Soc.* 64 [6] 350-354.
- [14] Rödel J, Kelly JF, Lawn BR. (1990). *In situ* measurements of crack interfaces in the SEM. *J. Am. Ceram. Soc.* in press.
- [15] Swanson PL. (1988). Crack-interface traction: A fracture-resistance mechanism in brittle polycrystals. In: *Fractography of glasses and ceramics*. Varner JR, Frechette VD, Eds. pp. 135-155.
- [16] Swanson PL, Fairbanks CJ, Lawn BR, Mai Y-W, Hockey BJ. (1987). Crack-interface grain bridging as a fracture resistance mechanism in ceramics: I, Experimental Study on Alumina. *J. Am. Ceram. Soc.* 70 [4] 279-288.
- [17] Tait RB, Garrett GG. (1986). Direct observation of fracture in brittle materials in the SEM using a double torsion testing technique. *Scanning* 8 129-138.

[18] Wiederhorn SM, Johnson H, Diness AM, Heuer AH. (1974). Fracture of glass in vacuum. *J. Am. Ceram. Soc.* 57 [8] 336-341.

[19] Wu CC, Rice RW, Becher PF. (1981). The character of cracks in fracture toughness measurements of ceramics. In: *Fracture mechanics methods for ceramics, rocks and concrete*, ASTM STP 745, Freeman SW, Fuller ER, Eds. pp. 127-140.

Discussion with Reviewers

D.L. Davidson: If material is (virtually) elastic why doesn't COD vary with the square root of the distance behind tip (rather than distance behind the tip)? Crack bridging would be more convincing if a variation in COD were illustrated (Why not a graph of COD from Fig. 3?). This may be done in [14] but that's not accessible.

Authors: Elastic simply means non-permanent deformation. A parabolic profile describes cracks with stress-free crack walls, a non-parabolic profile points to forces applied at the crack walls, not necessarily affecting the elastic behavior of the material. Crack openings can only be meaningfully measured where no secondary cracking occurs. The resolution of our method is also not good enough to measure the effect of just one bridge, which might affect the crack opening by only a few nanometers. The closure stresses, however, are far reaching and, taken cumulatively, can be evaluated using a profile measurement [14]. Alternatively, the opening of a secondary crack at a bridge site can also give information about the closure stress [14].

H. Mueller: Can the crack jumping or slipping process be related to microstructure? Is it likely that the advancing crack was inhibited at grain boundaries or is it likely that the grain interiors contained inhomogeneities (even though appearing homogeneous) to account for the crack stick-slip behavior? Can the molecular configuration of the alumina account for this behavior?

Authors: Discontinuous crack advancement is related to variabilities in the microstructure, like variability in the local stresses, the grain boundary toughness, etc.

H. Mueller: Mention is made for obtaining quantitative information by recording COD during loading/reloading. This is essentially the procedure used for determining fracture toughness via chevron-notched methodology which is now well established. With the loading device described herein, it does seem possible to record load vs COD thereby providing a means to determine a plane strain fracture toughness. Has any consideration been given to relating the load vs COD plots to microstructure via SEM analysis. With this in mind, the chevron-notch geometry can therefore be beneficial instead of what is stated as preliminary and intended for

elimination.

Authors: The methodology mentioned does not lend itself easily to measurement of R-curve behavior. Detailed mathematical calculations of the relevant R-curves from the crack profile for this material can be found in [14].

H. Mueller: The presence of residual stresses can be compressive and tensile in nature. Mention is made of crack closure stresses which are likely due to compressive residual stresses. In the case of residual tensile stresses, can it be thought that crack opening stresses may instead be generated along the crack? If this is so, crack weakening instead of crack toughening would be operative.

Authors: The residual compressive and tensile stresses perpendicular to the crack plane indeed average out to zero. The residual stresses related to bridge formation (enhanced secondary cracking, clamping of grains etc.) allow for the generation of closure stresses.

H. Mueller: Was an angle of 28° critical for obtaining crack propagation stability? If a chevron angle of about 9 1/2° was used instead and extended to about 6 mm on the unpolished disc surface, there would have been no need to remove the samples to resaw after a crack was grown to 2 mm. If 28° was optimal, a thicker sample size of about 3 mm could also have been used to grow cracks to 6 mm in length within the quasi chevron-notched region without stopping to remove and resaw the samples.

Authors: The angle of 28° was rather arbitrarily chosen. Since the area of bridged crack walls has to be kept identical from experiment to experiment, the identical chevron geometry has to be used and the suggestion is not applicable.

H. Mueller: The COD vs distance from the crack tip plot shown in Figure 4 is apparently without crack bridging mechanisms being included. If crack bridging is included within regions along the crack, how would a typical COD vs distance plot be characterized? One might think that a parabolic profile or some other decreasing profile would be depicted in this situation and that a linear profile would be depicted with a stress-free surface (just the opposite of that mentioned).

Authors: From standard fracture mechanics theory we know [3,10]: Stress-free crack surfaces lead to a parabolic profile. Figure 4 includes crack bridging (not parabolic).

CYCLIC FATIGUE FROM FRICTIONAL DEGRADATION AT BRIDGING GRAINS IN ALUMINA

Srinivasarao Lathabai,\*† Jürgen Rödel,\* and Brian R. Lawn

Ceramics Division  
National Institute of Standards and Technology  
Gaithersburg, MD 20899

September 1990

For: J. Amer. Ceram. Soc.

-----  
\* Guest Scientist: From the Department of Materials Science  
and Engineering, Lehigh University, Bethlehem, PA 18015

† Now at Division of Materials Science, CSIRO, Clayton, VIC  
3168, Australia

## ABSTRACT

Tension-tension cyclic loading tests have been conducted on a coarse-grained alumina ceramic that exhibits toughness-curve behavior by grain-interlock bridging. Fatigue effects are observed in the regions of both short cracks, using indentation flaws, and long cracks, using compact-tension specimens. A true mechanical fatigue effect is demonstrated by running the tests below the static fatigue limit. A custom-made device for in situ observation of crack propagation in the scanning electron microscope enables us to identify bridge degradation as a cause of the fatigue process. "Wear" debris cumulates at the sliding intergranular frictional contact points, indicating a loss of traction at the junction. The basis of a fracture mechanics model describing the effect of this frictional degradation in reducing crack-tip shielding is outlined and fitted to the data. It is suggested that the bridge degradation fatigue mechanism may be widespread in polycrystalline ceramics with pronounced toughness curves.

## KEY WORDS

Ceramics, cyclic fatigue, frictional degradation, grain bridging, in situ device, scanning electron microscopy, wear debris.

## 1. INTRODUCTION

A new breed of flaw-tolerant ceramics is emerging. Flaw tolerance is a manifestation of crack-tip shielding that cumulatively toughens the material as the crack extends, resulting in an increasing toughness curve (R-curve or T-curve) [1]. Several shielding processes have been considered in the literature, most notably frontal-zone phase transformation and microcracking. But in monophase ceramics like aluminas the principal mode is bridging of the crack interface by interlocking grains [2-4]. A leading question in the potential use of such materials for structural applications is whether the elements responsible for the toughening degrade during reversed loading: do bridging materials exhibit cyclic fatigue?

Authentications of true, mechanical cyclic fatigue are remarkably sparse in the ceramics literature. Early studies on alumina [5-8] reported reduced lifetimes in cyclic relative to static loading. A fracture mechanics analysis of results on glass and porcelain (in the context of a review of some of the earlier data [5,8]), suggested that the fatigue could be explained as the integrated effect of environmentally-enhanced slow crack growth [9]. Subsequent reports of fatigue on silicon nitride [10-12] were subject to similar ambiguity, while a study on silicon carbide [13] showed no cyclic effect at all. However, more recent studies on aluminas [14,15], zirconias [16,17] and silicon nitrides [18-20] do appear to demonstrate a definite mechanical cyclic fatigue.

If authentication of the existence of true cyclic fatigue has been slow in coming, identification of the responsible mechanisms of degradation is virtually totally lacking. Some authors, drawing largely from the greater

knowledge of fatigue processes in metallic materials, have proposed very specific mechanisms for fatigue damage in ceramics [21-23]. One class of these mechanisms invokes crack "closure" <sup>1</sup>, including wedging by crack-interface asperities, debris and the like; others invoke frontal-zone microcracking or even microplasticity. However, no direct experimental evidence has yet been put forward to prove or disprove any of these hypothetical mechanisms. Surprisingly, the possibility of interfacial bridge degradation has been only very recently been given any consideration at all in the literature [24].

Our objective in the present study is to investigate the effect of cyclic tension-tension loading on an alumina ceramic with a demonstrably pronounced T-curve from bridging, in the opposite domains of "short" cracks pertinent to strength properties and "long" cracks encountered in specimens for toughness evaluations. For the short cracks we use indentation flaws, comparing lifetimes of flexure specimens under cyclic loading with those of control static specimens. In an earlier, less complete study of this kind in our laboratories [25] on a finer-grained alumina (i.e. with weaker T-curve) we were unable to detect any true degradation, over and above that due to moisture-induced slow growth, in the strength properties. For the long cracks we use a compact-tension geometry, subjecting the specimen to cyclic loading at various interruption stages in the crack extension. Evidence for modest mechanically-induced cyclic fatigue is found in both crack-size domains.

In light of the hypothetical nature of previously proposed fatigue

---

<sup>1</sup> A term coined by metallurgists to designate obstruction to closure on unloading. It means, somewhat perversely, a residual opening.

mechanisms, we use a custom-designed device [26,27] for in situ viewing of cracks in our material in the scanning electron microscope (SEM). Direct observations during cyclic loading reveal the cumulation of debris at sliding grain facets along the crack interfaces. A specific model for fatigue damage in bridging ceramics, based on frictional degradation at grain-interlock "pullout" sites, is thereby advanced. It is proposed that frictional degradation may be a dominant fatigue mechanism in a broad range of ordinary monophase and multiphase ceramics, and therefore a factor for special consideration in designing with such materials.

## 2. EXPERIMENT

The material used in this study was a commercial polycrystalline alumina, with < 0.1% additive.<sup>2</sup> The specimens were obtained as disks 22 mm in diameter and 2 mm thick, and plates 100 mm x 100 mm x 6 mm. This alumina was nominally the same as used in our earlier study [25], except that it was subjected to a heat treatment to coarsen the mean grain size, from 23  $\mu\text{m}$  to 35  $\mu\text{m}$ , and thereby strengthen the T-curve. It fractured predominantly by intergranular fracture, with some transgranular fracture through the larger grains [2,4]. Fatigue tests were run in tension-tension loading, as follows.

---

<sup>2</sup> Vistal grade  $\text{Al}_2\text{O}_3$ , Coors Ceramics Co., Golden, CO

## 2.1 Short-Crack Fatigue Tests

"Short-crack" tests were conducted on the disks. Vickers indentation flaws at a load of 30 N (immediate post-contact radial crack dimension  $\approx$  100  $\mu\text{m}$ ) were placed at the centers of the prospective tensile faces. The indented disks were mounted on a biaxial loading fixture [28], using a flat circular punch of diameter 4 mm on a three point support of diameter 19 mm. Cyclic tests were run in water, with sinusoidal loading at frequencies of 1 and 100 Hz on a digitally-controlled servo-hydraulic testing machine.<sup>3</sup> The maximum tensile stress was adjusted as required, but the minimum was maintained constant at 20 MPa. Runs were discontinued if no failure occurred within 24 to 40 hours. Control tests were carried out under static loading in water, at the same maximum levels as in the cyclic runs. Additional, "calibration" strength tests were run at the same indent load (30 N) at constant stressing rates in water, and at various loads in inert environment (silicone oil), to evaluate the intrinsic crack velocity and microstructural T-curve parameters for our material [29].

## 2.2 Long-Crack Fatigue Tests

"Long-crack" tests were conducted on two plate specimens, width 44 mm (measured from the load line), in the compact-tension geometry of ASTM E399 [30]. The viewing surfaces of these specimens were polished to 1  $\mu\text{m}$  finish, for optimal crack observation. A starter notch of length 14 mm and tip radius  $\approx$  420  $\mu\text{m}$  was machined into each specimen. To control pop-in, a half-chevron

---

<sup>3</sup> Instron Digital Servo-hydraulic Testing Machine 8502, Instron Corp., MA

slot of included angle  $\approx 28^\circ$  and radius  $\approx 200 \mu\text{m}$  was sawn at the end of the machined notch, so that the slot extended just beyond the notch on the polished surface. A Vickers indentation (50 N) was placed  $\approx 200 \mu\text{m}$  in front of the half-chevron on this latter surface. This led to a precrack of length  $\approx 250 \mu\text{m}$  on loading. After subsequent incremental extensions the crack was re-sawn to within  $\approx 300 \mu\text{m}$  of the new crack tip.

One of the specimens was then loaded in displacement-control mode in the servo-hydraulic testing machine, in laboratory atmosphere (relative humidity 50-60%). A travelling microscope was used to track the crack growth. At the first sign of slow crack growth the crack was immediately unloaded, to avoid premature failure of the system. The specimen was then transferred to a transmission optical microscope, and the crack length measured. A crack-opening-displacement (COD) gauge attached to the crack notch mouth (via steel knife edges fixed to the specimen with epoxy) enabled the load at which crack growth initiated to be readily determined as the point where the load-displacement record deviates from linearity. The applied stress-intensity factor  $K_A$  at each such point of crack growth was computed from the ASTM standard formula [30]. This procedure was repeated at various crack growth increments in monotonic loading, to allow for determination of the quasistatic toughness curve as a function of crack extension,  $K_A = T(\Delta c)$  [1].

A similar procedure was adopted for the second specimen, except that now the specimen was only partially unloaded at the interruption points, and then subjected to a specified static-cyclic loading sequence. Static loading was thus run at a stress-intensity factor  $K_A = 0.8-0.9$  times that for quasistatic extension in monotonic loading. Cyclic loading was sinusoidal, frequency 10 Hz, at maximum  $K_A^{\text{Max}} = K_A$  and amplitude  $K_A^{\text{Min}}/K_A^{\text{Max}} = 0.1$ . In these experiments

the crack length was carefully monitored via the travelling microscope, and the system once more unloaded after extensions of 500  $\mu\text{m}$  or more. After each such interval of static-cyclic loading the crack was reloaded to quasistatic extension and the toughness reevaluated.

### 2.3 In-Situ Observations of Bridging Crack

In situ fatigue tests were conducted using a custom-designed device for incorporation in the SEM [26,27], similar in design to that of Frei and Grathwohl [24]. Compact-tension specimens were prepared as above for the SEM in situ observations, except that the cracks were always contained within the initial chevron sawcut as an extra precaution against uncontrolled crack instability [26]. At the vacuum level in the SEM environmentally-induced slow crack growth was almost totally eliminated, although some was occasionally observed if this vacuum was allowed to deteriorate (e.g. after switching off the diffusion pump). The viewing surfaces were again polished to 1  $\mu\text{m}$  finish, and gold coated before insertion into the SEM. After propagating the crack to a suitable crack length the opening force was reduced to a level  $K_A = 0.8T - 0.9T$  ( $T$  the toughness at that length in monotonic loading) and the specimen subjected to an interval of cycling. This was done via a piezoelectric drive controlled remotely through a function generator outside the SEM chamber [26,27]. The frequency was limited to a maximum of 2 Hz. The load amplitude was also limited, thereby necessitating manual preload of the crack before insertion into the SEM. Several locations of interest along the crack interface could be monitored during the cycling interval by means of a videocassette recorder, and photographed at static load at any point.

### 3. RESULTS

#### 3.1 Short Crack Fatigue Tests

The lifetime data for the indentation-flaw specimens are summarized in Figs. 1-3. Fig. 1 shows the time to failure at static stresses,  $\sigma_A = \text{const.}$  "Survivors" are represented by arrows. We note that the lifetime varies dramatically with minute changes in the applied stress, indicating that the system is close to a static fatigue limit for this material: i.e. the cracks are growing close to a threshold in the intrinsic crack velocity function [29]. Thus by operating at this stress level we may conveniently minimize the role of chemically-assisted slow growth in the cyclic tests. The curve through the data represents a theoretical prediction (Sect. 4) from the calibrated microstructural T-curve and crack velocity parameters at the prescribed indentation load [25,29].

Fig. 2 shows the comparative lifetime data for cyclic loading as a function of maximum applied stress,  $\sigma_{\text{Max}}$ , at the two frequencies used. A rapid variation of lifetime with applied stress is again apparent, although in this case there does appear to be some indication of a systematic if modest falloff relative to the predicted curves for kinetic crack growth alone [25], especially at the higher frequency. The falloff is seen to better effect in Fig. 3, which replots the data as a function of cycles to failure. The fact that the data fit a more universal curve in the replotted figure is further indication that the fatigue is due to a true mechanical effect.

### 3.2 Long Crack Fatigue Tests

Results of the compact-tension toughness-curve tests are plotted in Fig. 4. Data for the two specimens overlap within experimental error, saturating at  $T \approx 5.3 \text{ MPa}\cdot\text{m}^{1/2}$ . We reemphasize that the toughness values in this plot are quasistatic, in that the tests are carried out in air and the crack does not extend in strict equilibrium; i.e. the configuration is located part way up the velocity curve in monotonic loading. Recalling that one of these specimens was subjected to interrupted static and cycling sequences; we conclude that any degradation of the shielding that might have occurred in reversed loading is insufficient, at least over the cyclic range covered, to be detectable in the toughness data.

At the same time, there is compelling evidence, from the measurements of crack extensions  $\delta c$  over the interruption intervals  $\delta t$ , that some such degradation does occur. The results of three interrupt sequences, each at specified values of  $K_A(\text{static}) = K_A^{\text{Max}}(\text{cyclic})$ , are plotted in Fig. 5. In each case  $\delta c/\delta t$  is significantly larger in cyclic relative to static loading, despite the smaller integrated stress-intensity factor. Note in particular the first two sequences at  $K_A = 4.2 \text{ MPa}\cdot\text{m}^{1/2}$  (i.e. at  $0.8T$ ): there is a total absence of crack growth in the static phase, indicating that at this  $K_A$  level the system lies below the crack velocity threshold; and yet there is significant extension in the ensuing cyclic phase, again implying some mechanical fatigue effect.

### 3.3 In Situ Observations

The in situ SEM device provided an opportunity to follow the development of bridging sites along the intergranular crack interface during cyclic loading tests. Notwithstanding the practical limitation on number of cycles, evidence for continuing bridge evolution was obtained in these tests, with and without attendant crack propagation. Selected sequences are shown in Figs. 6-10 (crack propagation top to bottom and applied loading horizontal in all cases). All bridging elements in these sequences are photographed at peak crack opening in the in situ cycle unless otherwise qualified, with number of cycles  $n$  and distance  $x$  behind crack tip indicated where appropriate:

(i) Figure 6: segmentation of a bridging grain at three stages in its development. Between (a) and (b), after a few thousand cycles and minor crack propagation, the crack closes at lower right (segment P) and redirects, releasing internal stress in the intervening grain [26]. Between (b) and (c), the crack propagates further by virtue of an increment in the applied load, and undergoes a second closure relaxation at upper right (segment Q). This example demonstrates the general capacity of bridging sites to continue their evolution in response to load perturbations well after passage of the primary crack front.

(ii) Figure 7: surface grain dislodgement from frictional rotation. Between (a) and (b) the primary crack advances under load and intergranular facet cracks link at the interlocking site, rotating the grain out of its "socket". On unloading, partially in (c) and almost completely in (d), the walls close

but the grain protrudes from the surface. Note in (d) that the opening is small,  $\approx 0.1$  times that at full load in (b) (i.e. in proportion to the reduction in  $K_A$ ), indicating that despite the grain dislodgement there is very little residual crack-interface wedging.

These first two sequences show distinctive evidence of bridge evolution in cyclic loading, but do not unequivocally establish a true mechanical degradation effect: how much of the evolution is due to inadvertent crack propagation, however small, during the cycling? Accordingly, the next sequences contain stages in which no propagation is observed during the cycling, and yet bridge degradation is still evident:

(iii) Figure 8: sliding grain boundary facet with apparently strong frictional traction. Cycling between (a) and (b) produces a secondary crack below the bridging grain (P), without detectable crack propagation. After further loading and propagation to (c), both primary and secondary cracks open up (the former almost to the point of disengagement of the sliding grain boundary facet). Subsequent static loading at constant load in a degraded SEM vacuum (by switching off the diffusion pump overnight) causes the crack to more than double its length, disengaging the bridging grain facet totally in (d). We note the dramatic "flipover" of grain segment P from the right side of the interface to the left between (c) and (d) at the point of disengagement, indicating that this segment remains permanently attached at its subsurface base to the left wall throughout the separation, like a highly sprung cantilever. The consequent release of elastic strain energy at disengagement in this case must be considerable and highly dissipative.

The following two sequences are further examples of bridge evolution in reversed loading, but with closer attention to degradation of frictional facets for extended cycling periods:

(iv) Figure 9: degradation of frictional facet. Through cycling stages (a)-(e) there is gradual cumulation of debris from the sliding grain facet interface, even between (c)-(e) where no primary crack propagation occurs. Stage (f) is after total unload; note the residual opening at upper right, indicating some small wedging in this region.

(v) Figure 10: another frictional facet. Similar to Fig. 9, with appearance of debris between (a)-(c) (no crack propagation between (b) and (c)). Stage (d) shows enhanced debris buildup after prolonged additional cycling in air.

Selective energy dispersive spectroscopy of the debris in Figs. 9 and 10 reveals strong aluminum and oxygen peaks, and trace magnesium, but no excess gold, consistent with some product from the alumina itself rather than from the surface coating or any extruded grain boundary phase.

These micrographs are representative of extensive examinations along the interfaces of three alumina specimens. The geometrical disposition of the interlocking configurations and the associated frictional degradation varies considerably from point to point. We have given some indication of wedging at incompletely closed cracks, but this was never a large effect (residual opening always  $< 0.2$  that at full load).

As in earlier studies [2,26], we find no evidence for detached frontal-zone microcrack clouds.

#### 4. MODEL

We noted from comparison of the indentation-strength data in Figs. 2 and 3 that it is total number of cycles, rather than integrated time, that is the important independent variable in the lifetime characteristics. The reduction in strength of the specimens is modest, < 20% in  $10^6$  cycles. In this context we may recall the apparent absence of any such effect in our earlier, preliminary study [25]; here we are using an alumina with a larger grain size, hence more pronounced toughness curve, and have extended the data range. Although there was little indication of any comparable reduction in toughness in the long-crack data of Fig. 4, the same tests revealed an enhancement in crack extension in cyclic loading, Fig. 5. The apparent absence of fatigue effects in control static tests (Figs. 1 and 5) is especially pertinent, implying that the (shielded) crack-tip stress-intensity factor  $K_*$  in those cases must remain below the threshold in the  $v-K_*$  curve. Taken together, these results would appear to imply a build-up of  $K_*$  during cyclic loading.

Several hypothetical mechanisms have been proposed to account for mechanical fatigue in cyclic loading. All may operate in certain materials under certain conditions, but none have hitherto been directly confirmed. In the present study we may immediately eliminate potential contributions from frontal zones [16,17], because our material is nontransforming and we see no microcracking clouds. Geometrical processes like asperity-induced secondary cracking [21], and wedging by debris [21,23,31] and surface roughness [21,23] ("closure"), have also been proposed; and we do see minor secondary cracking and residual crack openings at our crack interfaces. However, whereas some of these mechanisms do allow for an increase in the mean crack-tip stress-

intensity factor  $K_*$  in cyclic loading, none allows for an enhancement in the maximum  $K_*$  [23], as is necessary if the crack system is ever to rise above the velocity threshold.

The above SEM observations of frictional bridge activity provide a ready means of accounting for the fatigue results, via a progressive degradation of the shielding stress-intensity factor. To show this, we briefly summarize the more important elements of the toughness curve (T-curve) theory by grain-interlock bridging, referring the reader to earlier sources [25,29] for greater detail. The crack-tip stress-intensity factor is

$$K_*(c) = K_A(c) + K_R(c) + K_\mu(c) \quad (1)$$

with  $K_A(c) = \psi \sigma_A c^{1/2}$  from the applied stress ( $\psi$  a geometry term),  $K_R(c) = \chi P/c^{3/2}$  from any residual contact stresses (here relevant only to indentation cracks,  $\chi$  a contact coefficient [1,4,29]), and  $-K_\mu(c)$  a microstructural shielding term (note  $K_\mu < 0$ ) from the bridging. This last term is a function of several microstructural parameters, among them the coefficient of friction  $\mu$ , between sliding facets at grain interlock sites, i.e.  $K_\mu = K_\mu(\mu, c)$  [4,29]. As indicated earlier, these microstructural parameters (and thence the T-curve) are calibrated from control indentation strength vs load data on our material in inert environments (Sect. 2.1). To accommodate environmentally-assisted slow crack growth we define a velocity function, based on thermal activation over atomically localized energy barriers [32]

$$v(G_*) = v_0 \sinh[(G_* - W_{BEB})/2\Gamma] \quad (W_{BEB} \leq G_* \leq W_{BB}) \quad (2)$$

with a threshold ( $v = 0$ ) at  $G_* = K_s^2(1 - \nu^2)/E = W_{BEB}$ :  $E$  denotes Young's modulus,  $\nu$  Poisson's ratio,  $W_{BB}$  and  $W_{BEB}$  the reversible work to separate the

grain boundary B-B in vacuum and environmental species E, respectively. The adjustable parameters  $v_0$  and  $\Gamma$  are calibrated from strength data in water at constant stressing rates (Sect. 2.1). Eqs. 1 and 2 constitute the underlying basis of the theoretically generated plots for the appropriate stress vs lifetime functions in Figs. 1 and 2 [25].

We propose that bridge degradation with increasing cycles is manifested primarily as a progressive reduction in the friction coefficient  $\mu(n)$ , hence in the magnitude of the shielding term  $-K_\mu(n)$ . Now for any given crack length  $c$  and applied stress  $\sigma_A$  we have  $\Delta K_s = \Delta K_\mu$  from Eq. 1. Then, since  $K_\mu < 0$  for bridging, we see that reduced shielding corresponds to increased  $K_s(n)$ , in the manner of Fig. 11. Figure 12 is a plot of  $\mu(n)$  corresponding to the indentation cyclic data, obtained by treating  $\mu$  as an adjustable parameter and using a numerical algorithm to solve Eqs. 1 and 2 for a best fit at each point in Fig. 3 [25]. We note that the reduction in  $\mu$  required to explain the strength degradation is not large, i.e. < 25% over the cycle range.

Using a smoothed function through the  $\mu(n)$  data in Fig. 12, we may now calculate  $K_\mu(n)$  from Eqs. 1 and 2 for cyclic loading in long cracks, and thence attempt to explain the data in Figs. 4 and 5. Accordingly, in Fig. 13 we plot  $-K_\mu(n)$  for the loading conditions pertaining to Figs. 5a and 5b (i.e. no static growth). The peak crack-tip field  $K_s^{\max}(n)$ , although starting below the threshold at  $W_{BEB}$ , attains this level after a critical interval, after which environmentally-assisted slow crack growth can occur, consistent with the observations of nonzero  $\delta c/\delta t$  during the cyclic loading stages in Fig. 5. At the same time, the decrement  $\Delta K_\mu(n) = K_\mu(1) - K_\mu(n)$  is sufficiently small, < 0.25 MPa·m<sup>1/2</sup>, over 150000 cycles as to pass unnoticed at the interruption points in the T-curve plots in Fig. 4.

## 5. DISCUSSION

We have observed cyclic fatigue in an alumina ceramic which exhibits toughness-curve behavior by bridging. By working below the static fatigue limit, i.e. below the crack velocity threshold, we are able to attribute the fatigue to true mechanical degradation of the material. On the basis of in situ observations of cracks during cyclic loading, we have proposed a new model for this degradation. To our knowledge, this represents the first attempt to develop a specific fatigue model based on other than circumstantial evidence. Grain-interlock bridges that impart toughness can degrade in repeated unloading and reloading. The cumulation of "wear" debris at bridging sites suggests a specific mechanism of this degradation, whereby frictional tractions at sliding bridging grain boundary facets diminish progressively by persistent reversed sliding.

Notwithstanding the SEM observations, our model of a degraded frictional junction must be recognized as largely phenomenological. There are some important questions that need to be answered if we are to obtain a proper understanding of the degradation process. Thus, what is the specific nature of the friction, given that the intergranular sliding interface is initially in a chemically bonded state? What is the role of environment, particularly water, in this friction? There is evidence in the wear literature that the friction at contacting surfaces of alumina can indeed be modified by repeated sliding; and, moreover, that this sliding produces debris from chemical reaction with environmental species [33]. Thus interfacial friction is a vital factor not only in toughness [4,34], but also in lifetime.

The present study should be seen as a first step in identifying and

modelling the mechanisms of cyclic fatigue in ceramics. There would appear to be a need for further investigation into various aspects of the fatigue characterization:

(i) Data. In view of the modest scale of the fatigue degradation seen in the present study, extension of the data range to greater numbers of cycles, and to compression-tension loading, appears warranted. Also, the indication is that our model, although formulated specifically from observations on alumina, may apply to nontransforming, bridging ceramics in general. Materials with more pronounced T-curves may therefore serve as better candidates for quantifying the degradation. There is also a need to rationalize the interrelations between short- and long-crack data; thus, a null effect in one test (e.g. Fig. 4) may not translate into a null effect in another (cf. Figs. 3 and 5), making general conclusions and extrapolations suspect in the absence of a proper degradation model.

(ii) In situ SEM. Direct observations are a crucial element of any proper identification of the fatigue processes in ceramic microstructures. This will inevitably be so in the more complex, multiphase ceramic composites, where multiple mechanisms may operate. Further confirmation of the frictional process, e.g. using more detailed surface analysis of the bridge debris in the immediate bridging zone, would seem desirable. Further SEM observations, e.g. by monitoring the crack-wall openings for hysteresis as a function of distance behind the crack tip [26] during unloading-reloading sequences, could be useful in quantifying the frictional properties [34].

(iii) Modelling. With more positive confirmation of friction as the major microstructural variable in the degradation mechanism of cyclic fatigue, one might ultimately attempt to express the model more closely in terms of documented frictional properties of interfaces, especially in regard to environmental interactions. This would open up the possibility of predetermining fatigue characteristics and tailoring interfaces for optimal resistance to degradation.

Finally, it is apparent that cyclic fatigue becomes an important design consideration in any application with moving ceramic parts. Such design will inevitably involve trade-offs. On the one hand, strong shielding is needed to promote flaw tolerance [4] and to enhance static fatigue limits [29]. It is the degradation of this same shielding that leads to fatigue.

#### ACKNOWLEDGEMENTS

The authors wish to thank Y-W. Mai for discussions, J.F. Kelly and D.E. Roberts for assistance with the experiments, and S. Derby for machining the specimens. Thanks are also due to J. Sibold of Coors Ceramics for providing the alumina. Funding was provided by the U.S. Air Force Office of Scientific Research.

## REFERENCES

1. Y-W. Mai and B.R. Lawn, "Crack Stability and Toughness Characteristics in Brittle Materials," Ann. Rev. Mat. Sci. 16 415-39 (1986).
2. P.L. Swanson, C.J. Fairbanks, B.R. Lawn, Y-W. Mai and B.J. Hockey, "Crack-Interface Grain Bridging as a Fracture Resistance Mechanism in Ceramics: I. Experimental Study on Alumina," J. Am. Ceram. Soc. 70[4] 279-89 (1987).
3. Y-W. Mai and B.R. Lawn, "Crack-Interface Grain Bridging as a Fracture Resistance Mechanism in Ceramics: II. Theoretical Fracture Mechanics Model," J. Am. Ceram. Soc. 70[4] 289-294 (1987).
4. S.J. Bennison and B.R. Lawn, "Role of Interfacial Grain-Bridging Sliding Friction in the Crack-Resistance and Strength Properties of Non-Transforming Ceramics," Acta Metall. 37[10] 2659-71 (1989).
5. L. S. Williams, "Stress Endurance of Sintered Alumina," Trans. Br. Ceram. Soc. 55[5] 287-312 (1956).
6. R. Sedlacek and F.A. Halden, "Static and Cyclic Fatigue of Alumina," pp. 211-20, in Structural Ceramics and Testing of Brittle Materials, edited by S.J. Acquaviva and S.A. Bortz, Gordon and Breach, New York (1967).
7. B.K. Sarkar and T.G.T. Glinn, "Fatigue Behavior of High Alumina Ceramics," Trans. Br. Ceram. Soc. 69[5] 199-203 (1970).
8. D.A. Krohn and D.P.H. Hasselman, "Static and Cyclic Fatigue Behavior of a Polycrystalline Alumina," J. Am. Ceram. Soc. 55[4] 208-11 (1972).
9. A.G. Evans and E.R. Fuller, "Crack Propagation in Ceramic Materials Under Cyclic Loading Conditions," Met. Trans. 5[1] 27-33 (1974).

10. Y. Matsuo, Y. Hattori, Y. Katayama, and I. Fukura, "Cyclic Fatigue Behavior of Ceramics," pp. 515-22, in *Progress in Nitrogen Ceramics*, edited by F. L. Riley, Martinus Nijhoff Publishers, The Hague, Netherlands (1983).
11. T. Kawakubo and K. Komeya, "Static and Cyclic Fatigue Behavior of a Sintered Silicon Nitride at Room Temperature," *J. Am. Ceram. Soc.* 70[6] 400-405 (1987).
12. M. Masuda, T. Toma, M. Matsui and I. Oda, "Cyclic Fatigue of Sintered Silicon Nitride," presented at the 12th Annual Conference on Composites and Advanced Ceramics, January 17-20, Cocoa Beach (1988).
13. S. Horibe and M. Sumita, "Fatigue Behavior of Sintered SiC; Temperature Dependence and Effect of Doping with Aluminum," *J. Mater. Sci.* 23[9] 3305-13 (1988).
14. L. Ewart and S. Suresh, "Crack Propagation in Ceramics under Cyclic Loads," *J. Mater. Sci.* 22[4] 1173-92 (1987).
15. M.J. Reece, F. Guiu and M.F.R. Sammuri, "Cyclic Fatigue Crack Propagation in Alumina Under Direct Tension-Compression Loading," *J. Am. Ceram. Soc.* 72[2] 348-52 (1989).
16. R.H. Dauskardt, W. Yu, and R.O. Ritchie, "Fatigue Crack Propagation in Transformation-Toughened Zirconia Ceramic," *J. Am. Ceram. Soc.* 70[10] C248-C252 (1987).
17. R.H. Dauskardt, D.B. Marshall, and R.O. Ritchie, "Cyclic Fatigue Crack Propagation in Ceramics: Behavior in Overaged and Partially-Stabilized MgO-Zirconia," in *Fracture Mechanics/Structural Ceramics*, Materials Research Society, Philadelphia, to be published.

18. C.-W. Li, D.J. Lee, J. Yamanis and I. Palley, "Cyclic Fatigue Properties of Silicon Nitride with Strong R-Curve Behavior". Paper presented at the 92nd Annual Meeting of the American Ceramic Society, Dallas, Texas, 1990.
19. J.T. Beals and I. Bar-On, "Fracture Toughness and Fatigue Crack Propagation of Silicon Nitride with Two Different Microstructures", Paper presented at the 14th Annual Conference on Composites and Advanced Ceramics, Cocoa Beach Florida, January 1990.
20. C.-W. Li and J. Yamanis, "Super-Tough Silicon Nitride with R-curve Behavior, Ceram. Eng. Sci. Proc. 10[7-8] 632-45.
21. A.G. Evans, "Fatigue in Ceramics," Int. J. Fract. 16[6] 485-98 (1980).
22. S. Suresh and J.R. Brockbrough, "Theory and Experiments of Fracture in Cyclic Compression: Single-Phase Ceramics, Transforming Ceramics and Ceramic Composites," Acta Metall. 35[6] 1455-70 (1988).
23. R.O. Ritchie, "Mechanisms of Fatigue Crack Propagation in Metals, Ceramics and Composites: Role of Crack Tip Shielding," Mater. Sci. Eng. A103 15-28 (1988).
24. H. Frei and G. Grathwohl, "Das Bruchverhalten Keramischer Hochleistungswerkstoffe bei In-situ Experimenten im REM," Beitr. Elektronenmikroskop. Direktabb. Oberfl. 22 71-78 (1989).
25. S. Lathabai, Y-W. Mai, and B.R. Lawn, "Cyclic Fatigue Behavior of an Alumina Ceramic With Crack-Resistance Curves," J. Am. Ceram. Soc. 72[9] 1760-63 (1989).
26. J. Rödel, J.F. Kelly, and B.R. Lawn, "In Situ Measurements of Bridged Crack Interfaces in the SEM", J. Am. Ceram. Soc., in press.

27. J. Roedel, J.F. Kelly, M.R. Stoudt and S.J. Bennison, "A Loading Device for Fracture Testing of Compact Tension Specimens in the SEM," Scanning Microscopy, in press.
28. D.B. Marshall, "An Improved Biaxial Flexure Test for Ceramics," Am. Ceram. Soc. Bull. 59[5] 551-53 (1980).
29. S. Lathabai and B.R. Lawn, "Fatigue Limits in Noncyclic Loading of Ceramics With Crack-Resistance Curves," J. Mater. Sci. 24[12] 4298-306 (1989).
30. American Society for Testing and Materials, Vol. 3.01, E-399-83, A.S.T.M., Philadelphia, 1989.
31. C.J. Beevers, K. Bell, R.L. Carlson, and E.A. Starke, "A Model for Fatigue Crack Closure," Eng. Fract. Mech. 19[1] 93-100 (1984).
32. K-T. Wan, S. Lathabai, and B.R. Lawn, "Crack Velocity Functions and Thresholds in Brittle Solids," J. Europ. Ceram. Soc., in press.
33. X. Dong, S. Jahanmir, and S.M. Hsu, "Tribological Characteristics of  $\alpha$ -Alumina at Elevated Temperatures," J. Am. Ceram. Soc.
34. D.B. Marshall and A.G. Evans, "Failure Mechanisms in Ceramic-Fiber/Ceramic-Matrix Composites," J. Am. Ceram. Soc. 68[5] 225-31 (1985).

## FIGURE CAPTIONS

1. Lifetimes in static loading of alumina in water, Vickers indentations ( $P = 30$  N). Most data points are results of individual tests; those with arrows are means of interrupted tests for minimum 5 specimens. Solid curve is theoretical prediction. Note fatigue limit.
2. Lifetimes in cyclic loading of alumina in water, Vickers indentations ( $P = 30$  N). Data points are individual tests, open symbols 1 Hz, closed symbols 100 Hz; arrows are interrupted tests, minimum 5 specimens. Solid line is theoretical prediction assuming environmentally-assisted slow crack growth without mechanical degradation.
3. Replot of data in Fig. 2 as function of cycles to failure. Symbols as in Fig. 2.
4. Toughness curves for two alumina compact-tension specimens (distinguished by open and closed symbols) in air. Unlabelled points represent quasi-equilibrium crack extension in monotonic loading. Labelled points a, b, c represent similar extension but after interruption static-cyclic sequence (see Fig. 5 for details).
5. Crack extensions during intervals in static-cyclic (10 Hz) interruption sequences at points labelled in Fig. 4: (a)  $K_A = K_A^{\text{Max}} = 4.2 \text{ MPa}\cdot\text{m}^{1/2}$ ; (b) same; (c)  $K_A = K_A^{\text{Max}} = 4.75 \text{ MPa}\cdot\text{m}^{1/2}$ .

6. SEM micrograph of crack in alumina, showing grain-bridging element: (a) after initial crack propagation (distance  $x = 860 \mu\text{m}$  behind crack tip); (b) after cycling in SEM ( $n = 7000$  at 2 Hz,  $K_A^{\text{Max}} = 0.85\text{T}$ ) and minor crack propagation ( $x = 880 \mu\text{m}$ ); (c) after increasing  $K_A$  and further propagation ( $x = 1080 \mu\text{m}$ ).
7. SEM micrographs of grain facet: (a) after initial crack propagation ( $x = 170 \mu\text{m}$ ), showing bridge; (b) after further loading and cycling ( $n = 7200$  at 2 Hz,  $K_A^{\text{Max}} = 0.8\text{T}$ ), with attendant propagation ( $x = 740 \mu\text{m}$ ); (c) after partial unload to  $K_A = 0.6\text{T}$ ; (d) at near-complete unload,  $K_A = 0.1\text{T}$ . Note near dislodgement of grain.
8. SEM micrographs of frictional grain facet: (a) after initial crack propagation ( $x = 290 \mu\text{m}$ ); (b) after cycling ( $n = 7200$  at 2 Hz,  $K_A^{\text{Max}} = 0.8\text{T}$ ), with no propagation; (c) after loading and cycling ( $n = 54000$  at 2 Hz,  $K_A^{\text{Max}} = 0.9\text{T}$ ), with accompanying propagation ( $x = 850 \mu\text{m}$ ); (d) after static loading in degraded SEM vacuum for 16 hr at  $K_A = 0.9\text{T}$ , with further propagation ( $x = 2120 \mu\text{m}$ ). Note appearance of secondary crack at segment P in (b) as result of cycling only, and ultimate "flip" of this segment from right to left side of interface between (c) and (d).

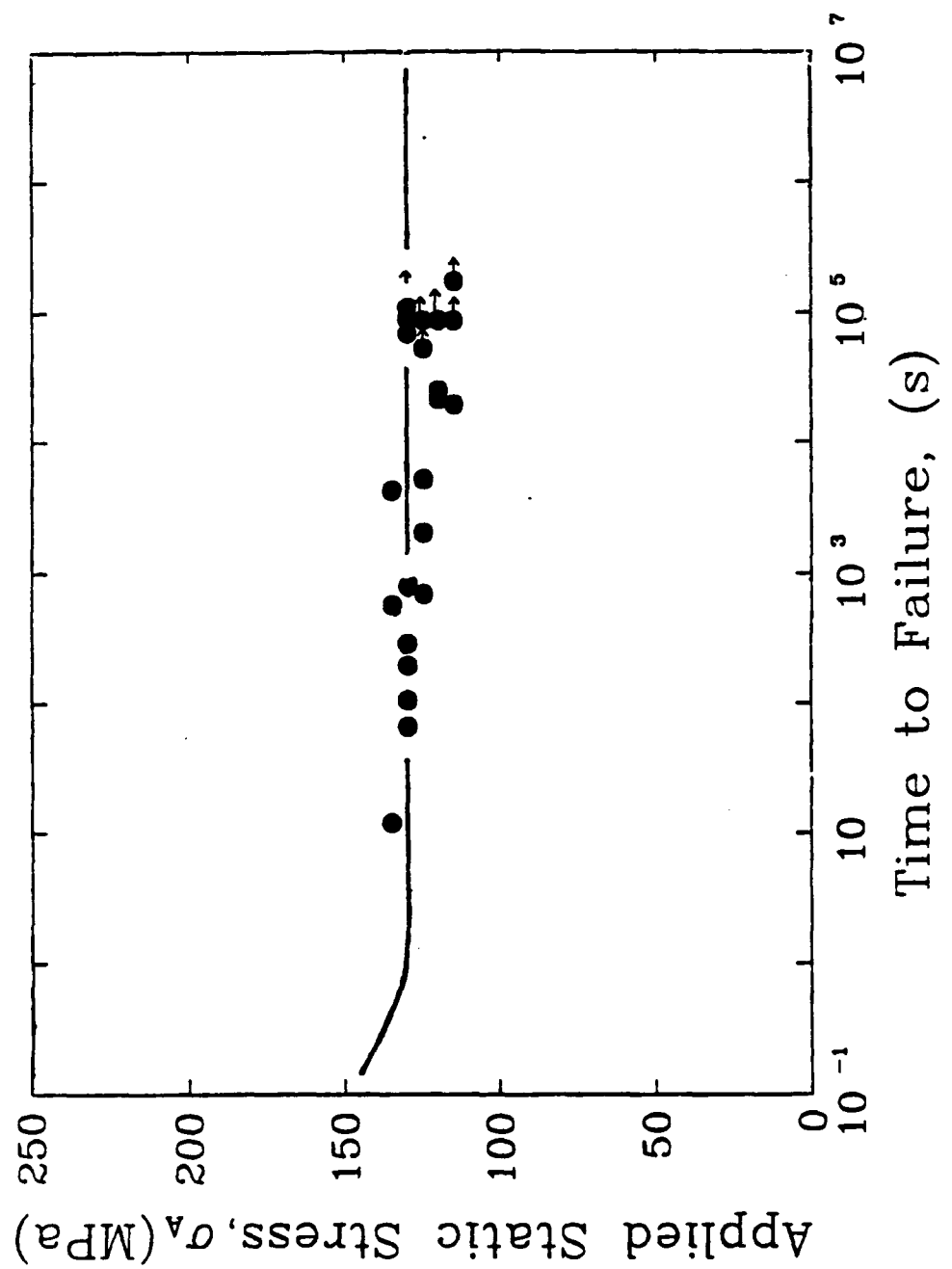
9. SEM micrographs of frictional grain facet at various stages of cycling (all cycles at 2 Hz,  $K_A^{Max} = 0.85T$ ): (a) after initial crack propagation ( $x = 610 \mu\text{m}$ ); (b) after  $n = 7000$ , with minor propagation ( $x = 630 \mu\text{m}$ ); (c) at  $n = 20000$  and additional propagation ( $x = 700 \mu\text{m}$ ); (d) at  $n = 27000$ , no propagation; (e) after  $n = 45000$ , no propagation; (f) total unload. Note cumulation of frictional debris at facet.

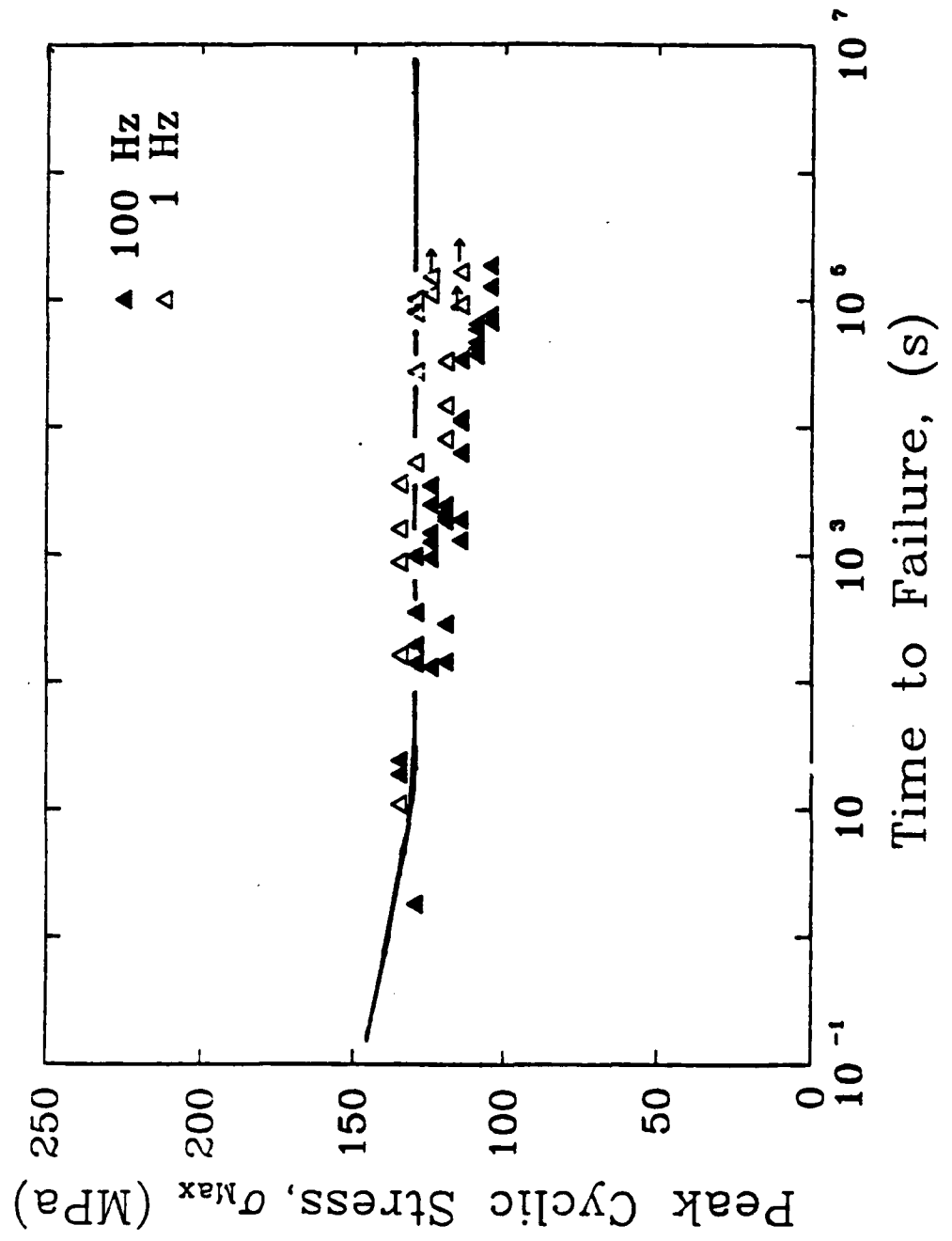
10. SEM micrographs of another frictional grain facet at various stages of cycling (all cycles at  $K_A^{Max} = 0.85T$ ): (a) after initial propagation ( $x = 820 \mu\text{m}$ ); (b) after  $n = 20000$  (2 Hz), crack propagation ( $x = 910 \mu\text{m}$ ); (c) after  $n = 45000$  (2 Hz), no propagation; (d) after  $n = 50000$  (10 Hz) in air, minor propagation ( $x = 930 \mu\text{m}$ ). Note debris.

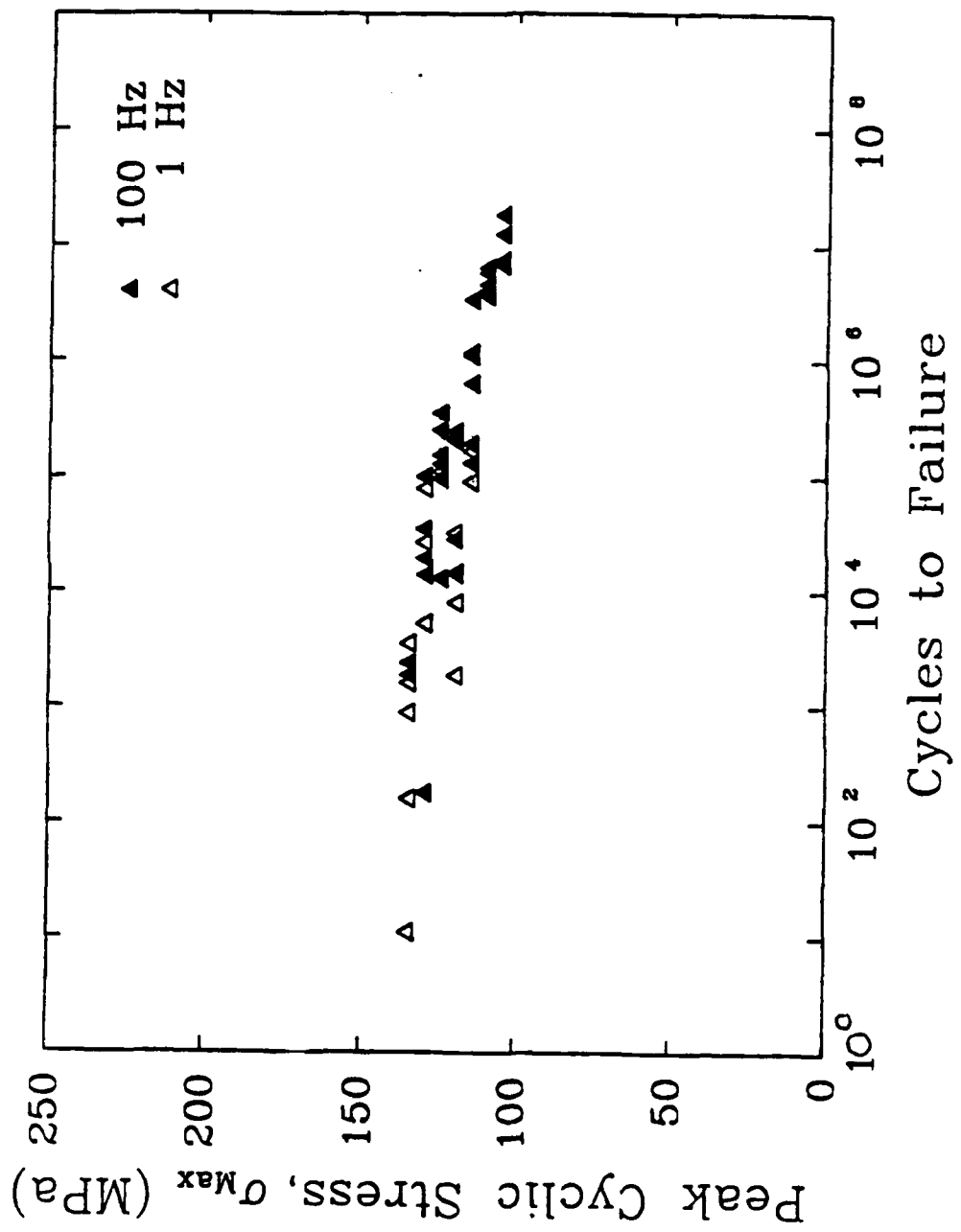
11. Schematic illustrating possible cyclic fatigue mechanism due to frictional degradation of bridges. As shielding term diminishes with cycling, crack-tip  $K_*$  steadily increases (solid curve), until sufficient to take system above threshold on velocity curve.

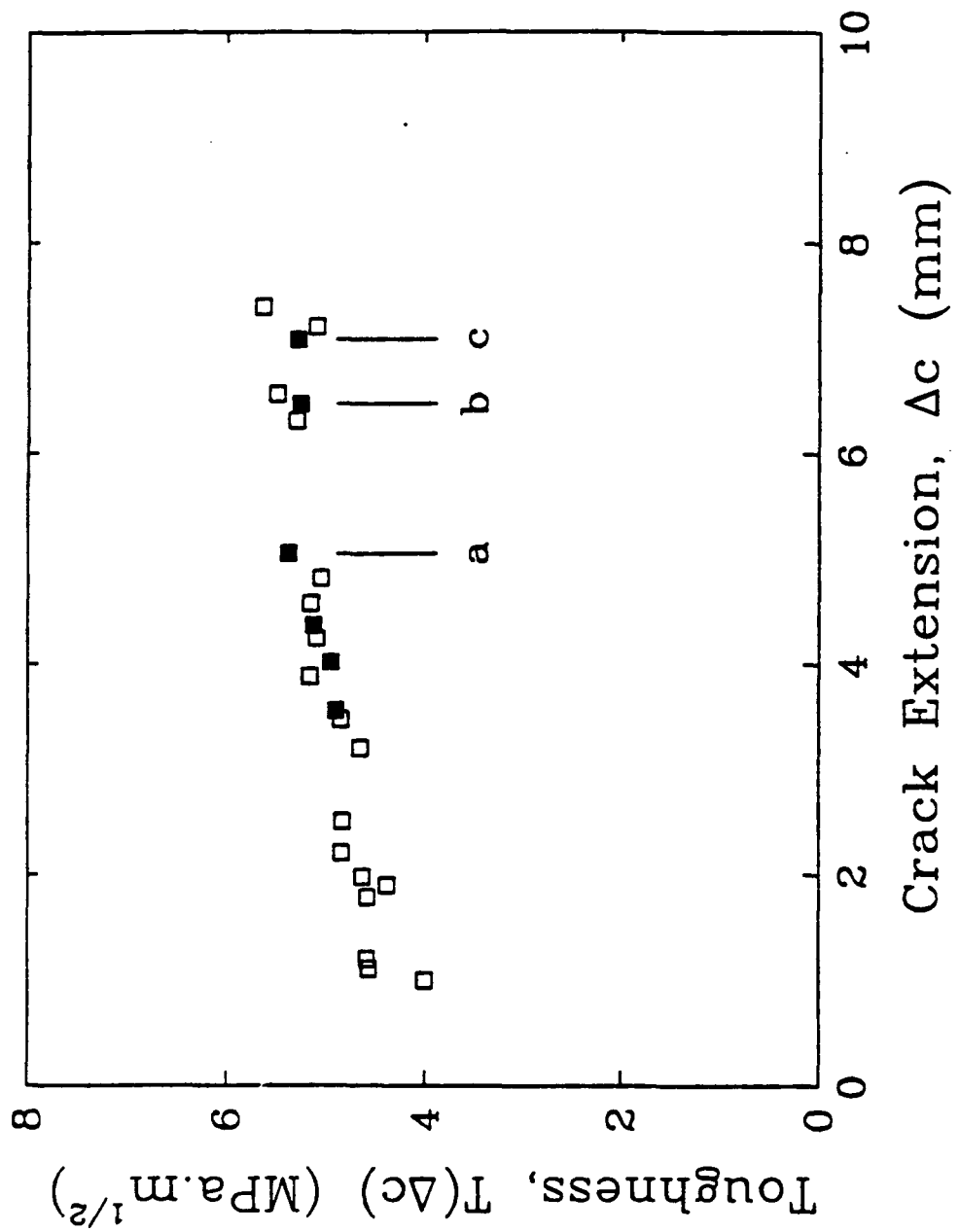
12. Computed degradation of friction coefficient with number of cycles required to account for fatigue effect in data for alumina in Fig. 3. Dashed line is calibrated friction coefficient for monotonic loading.

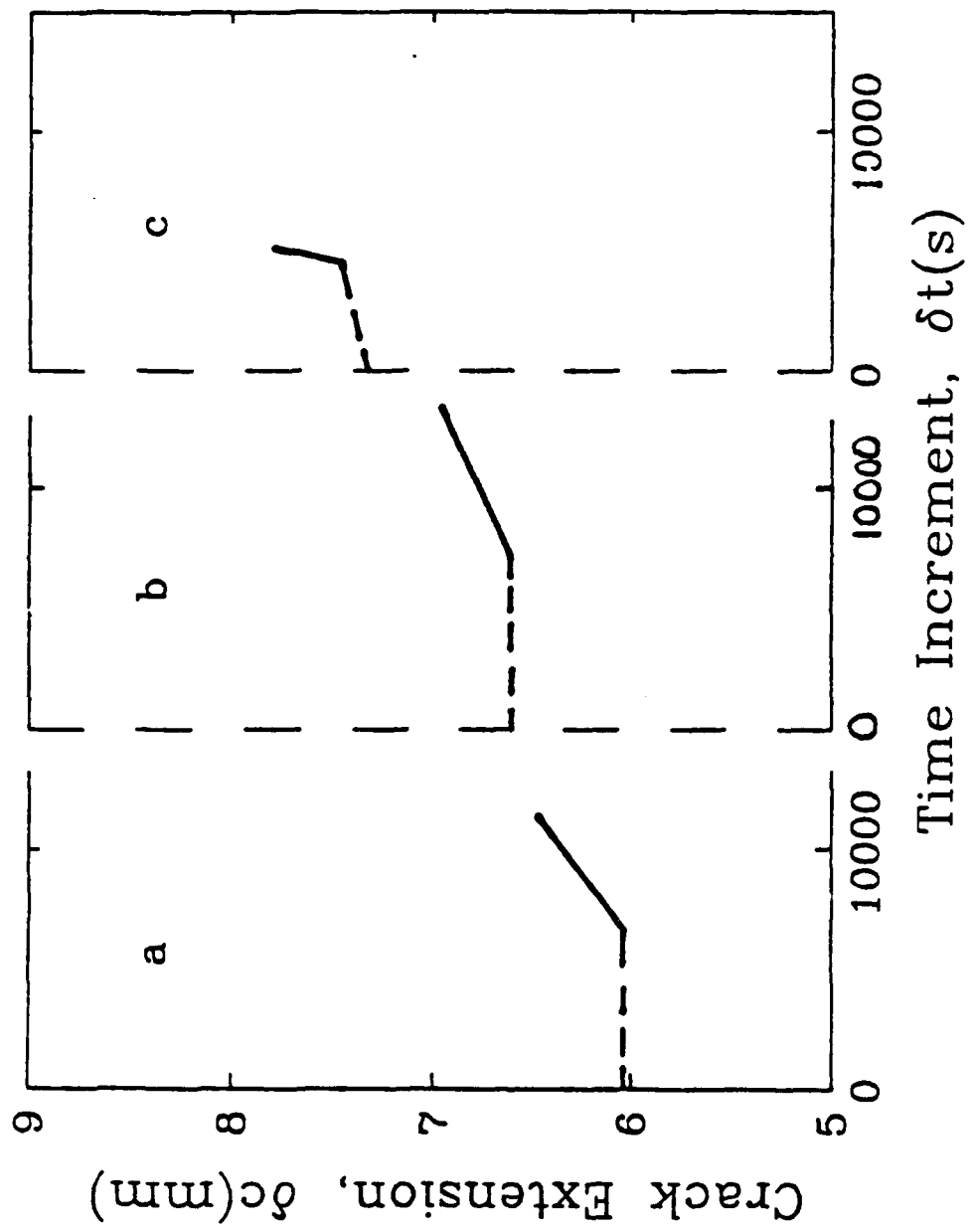
13. Plot predicting decreasing bridging field,  $-K_\mu(n)$ , for cyclic loading in alumina.

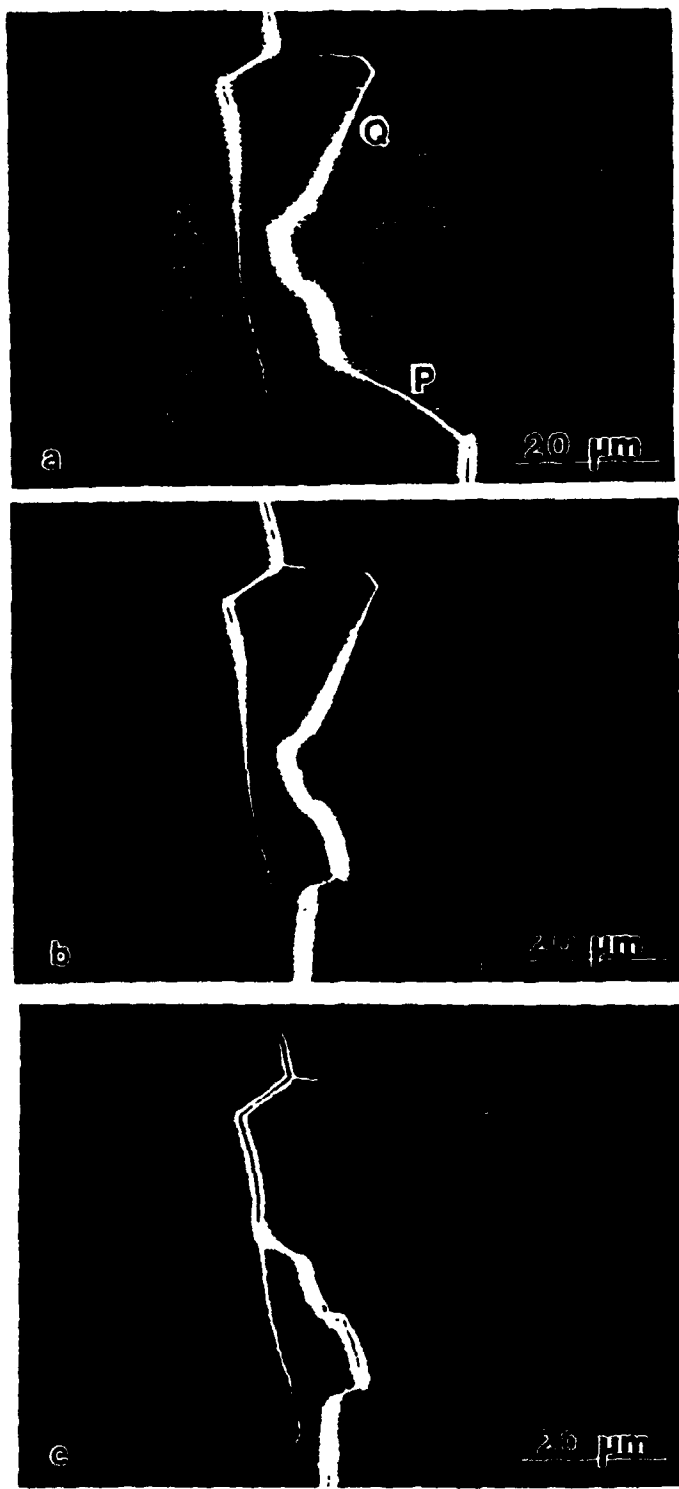


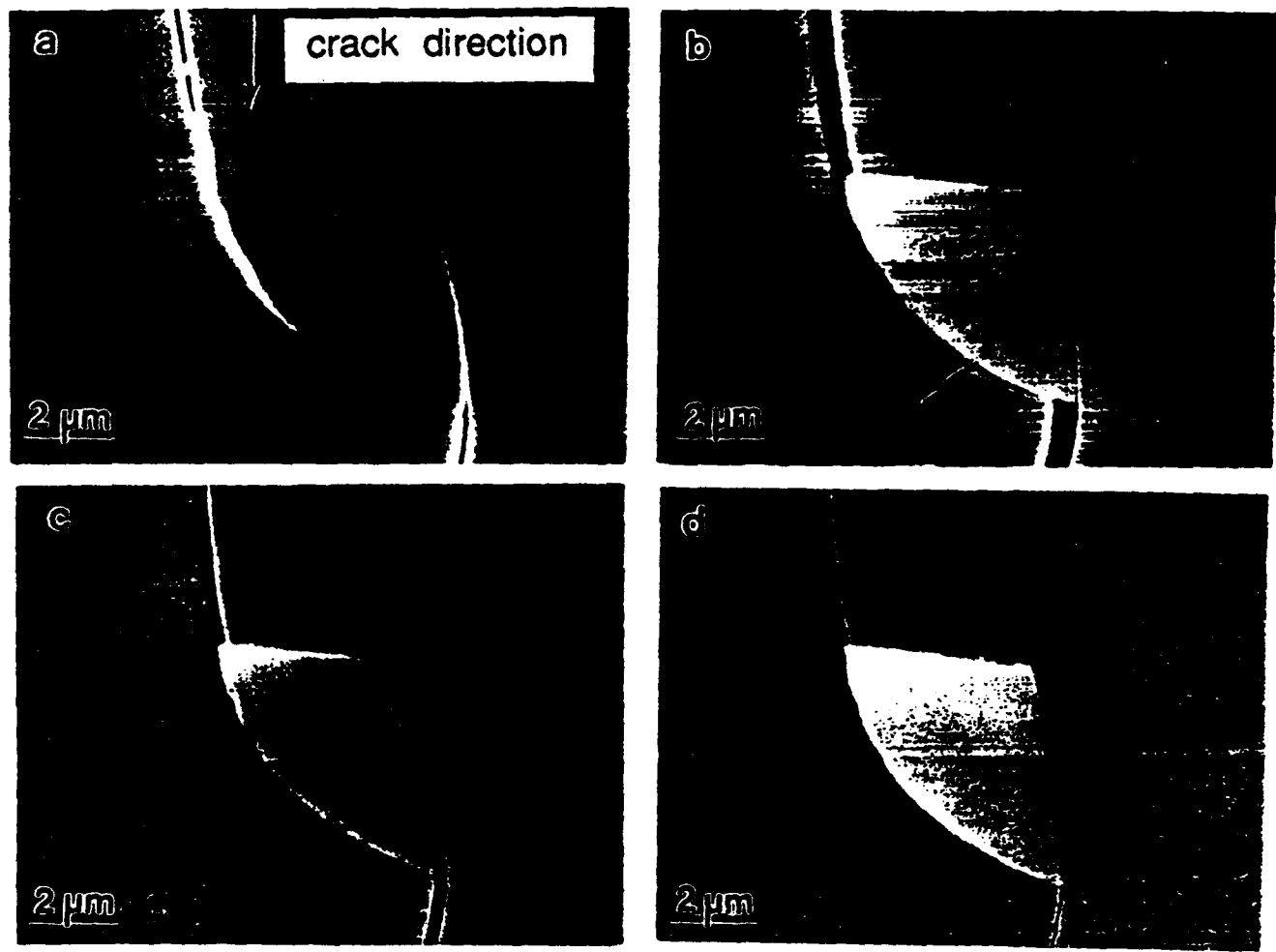


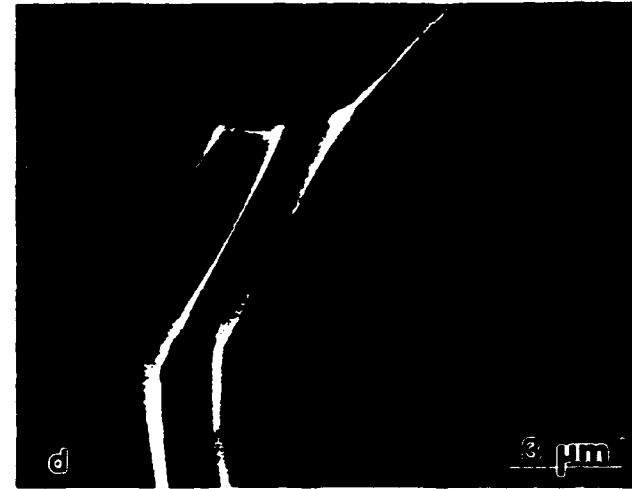
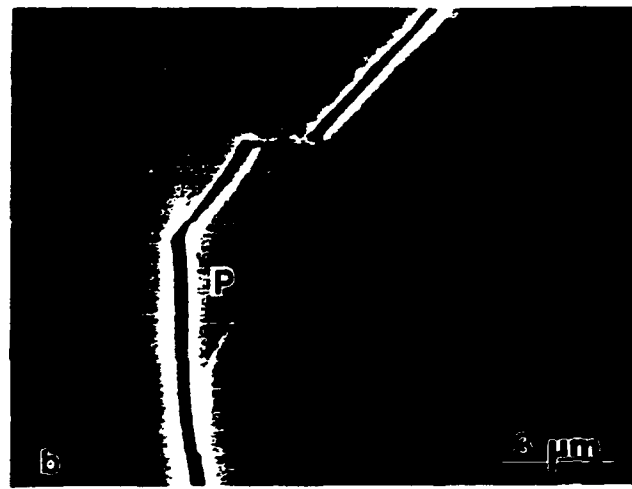
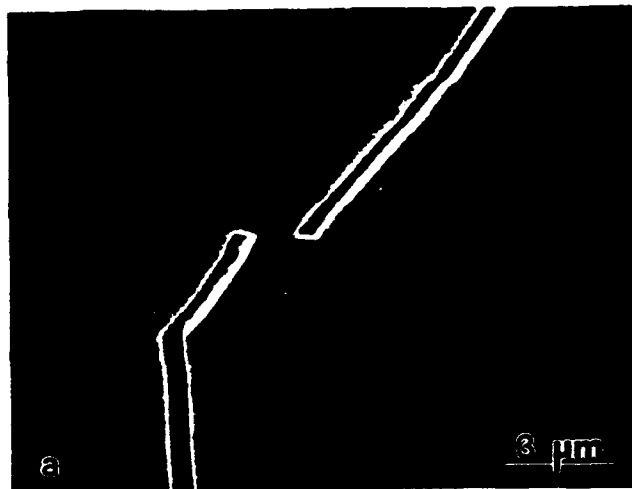


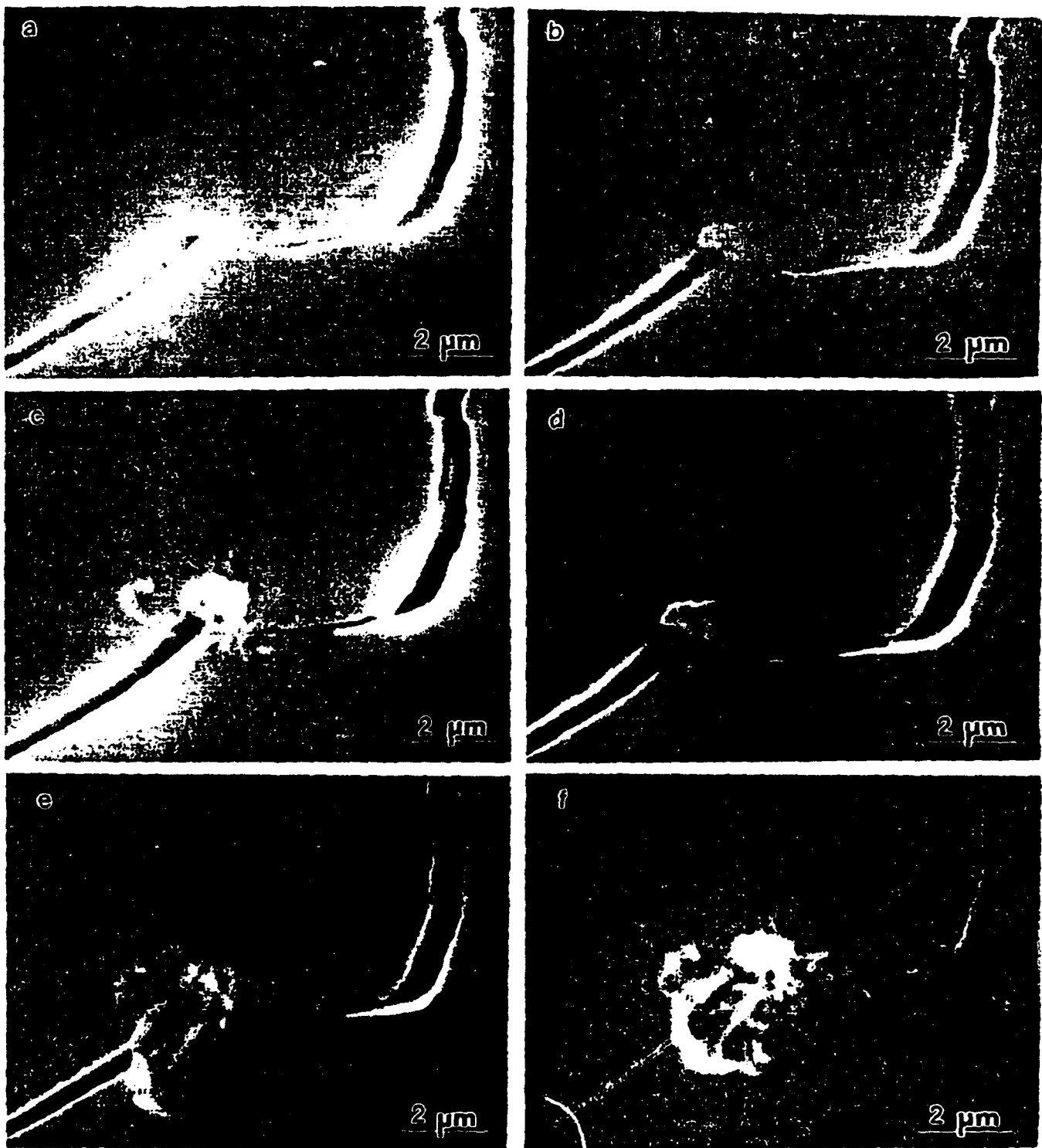


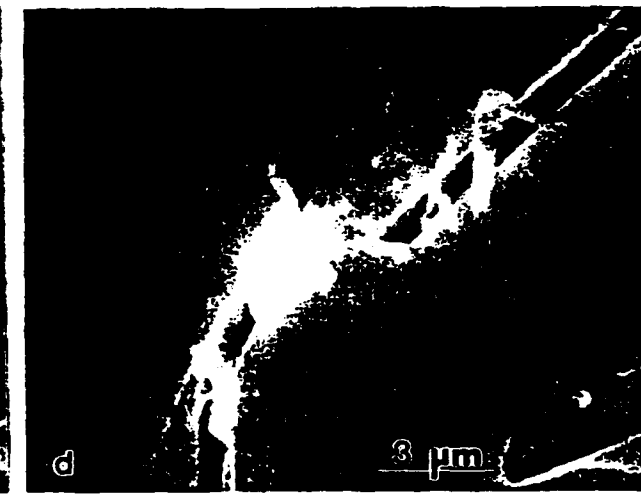
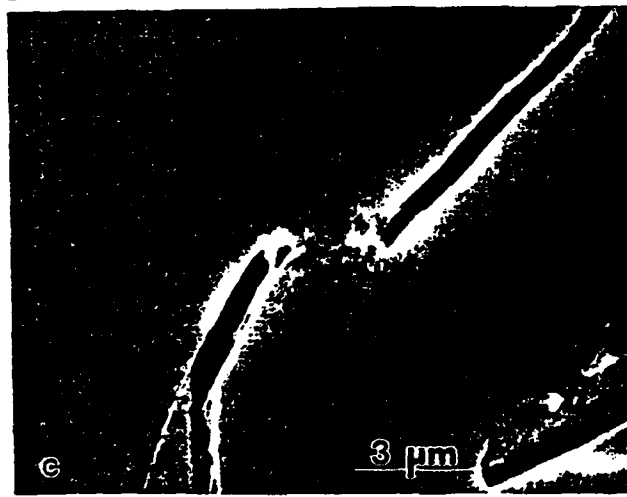
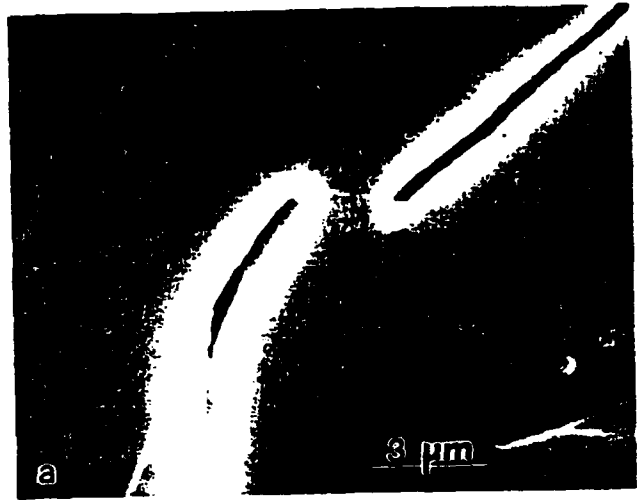


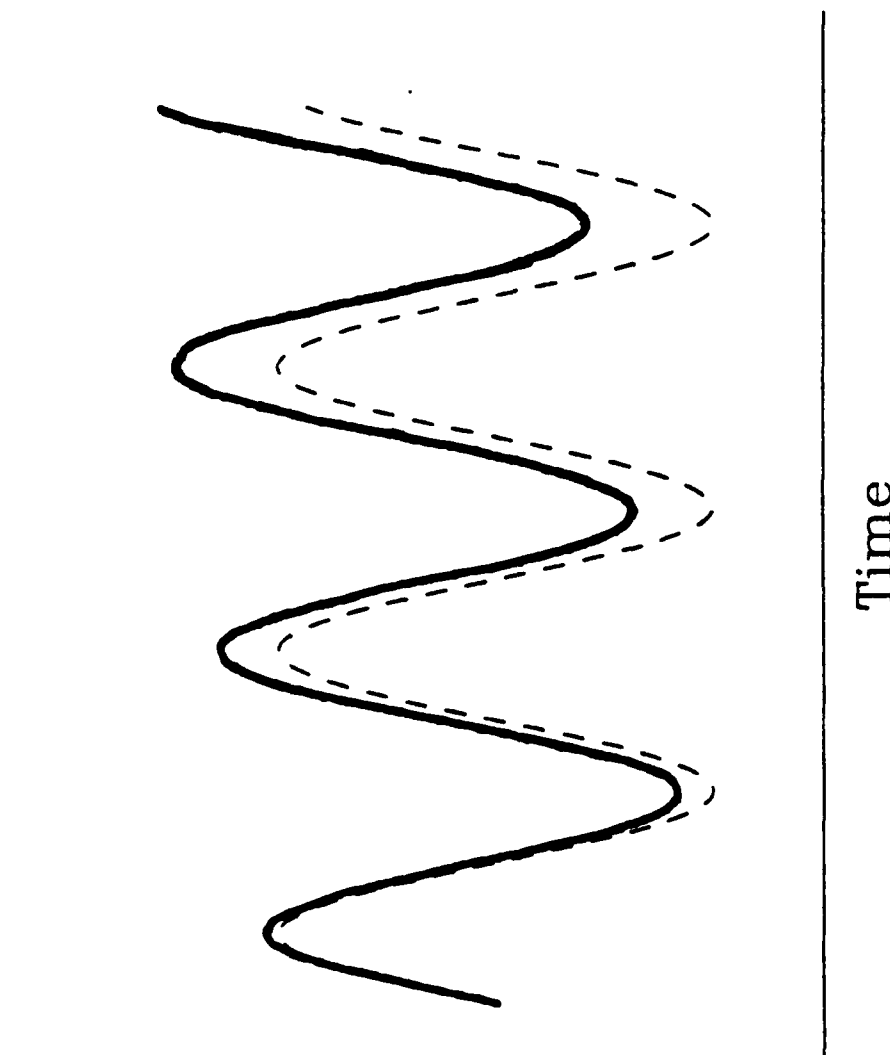


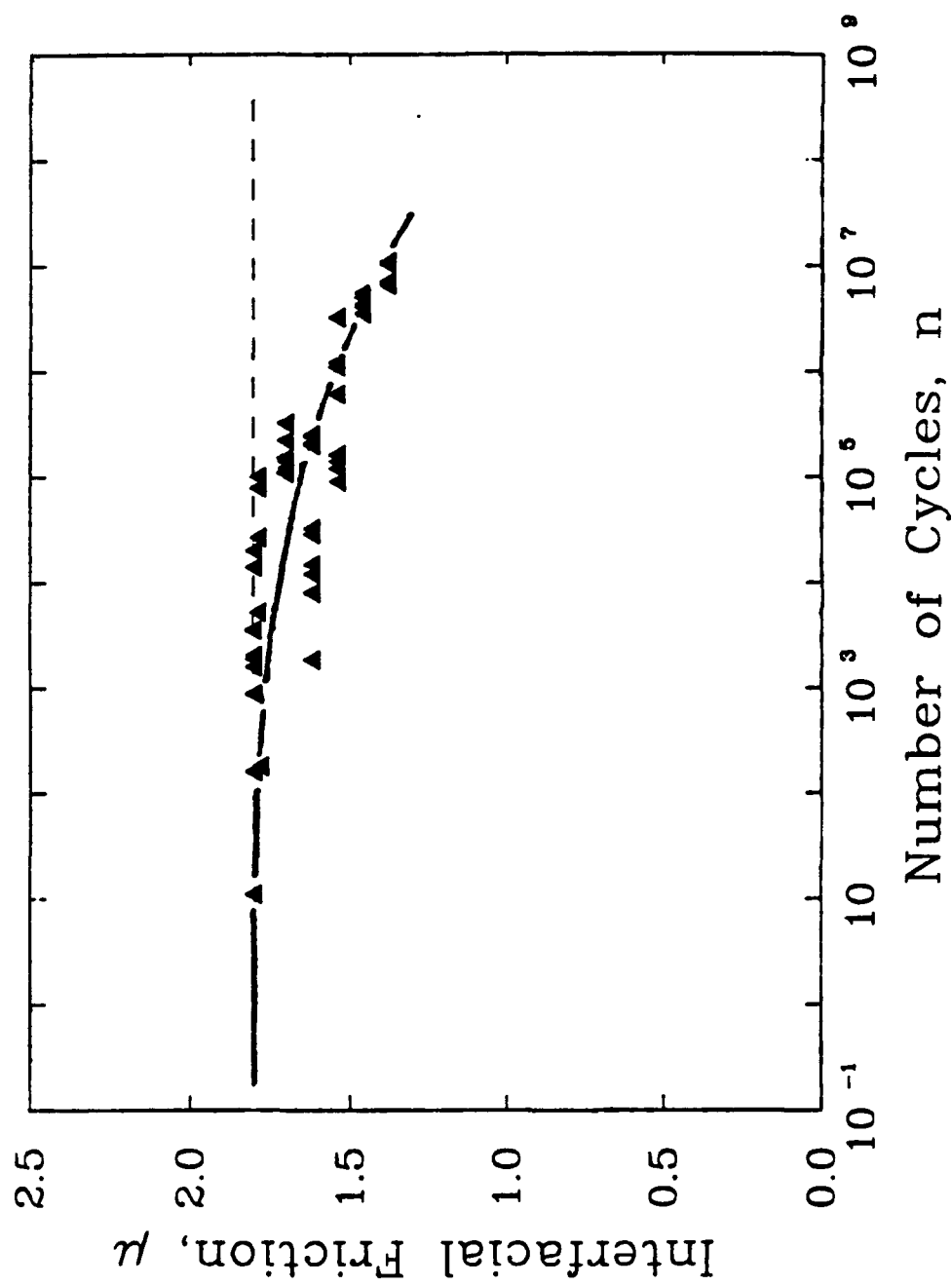


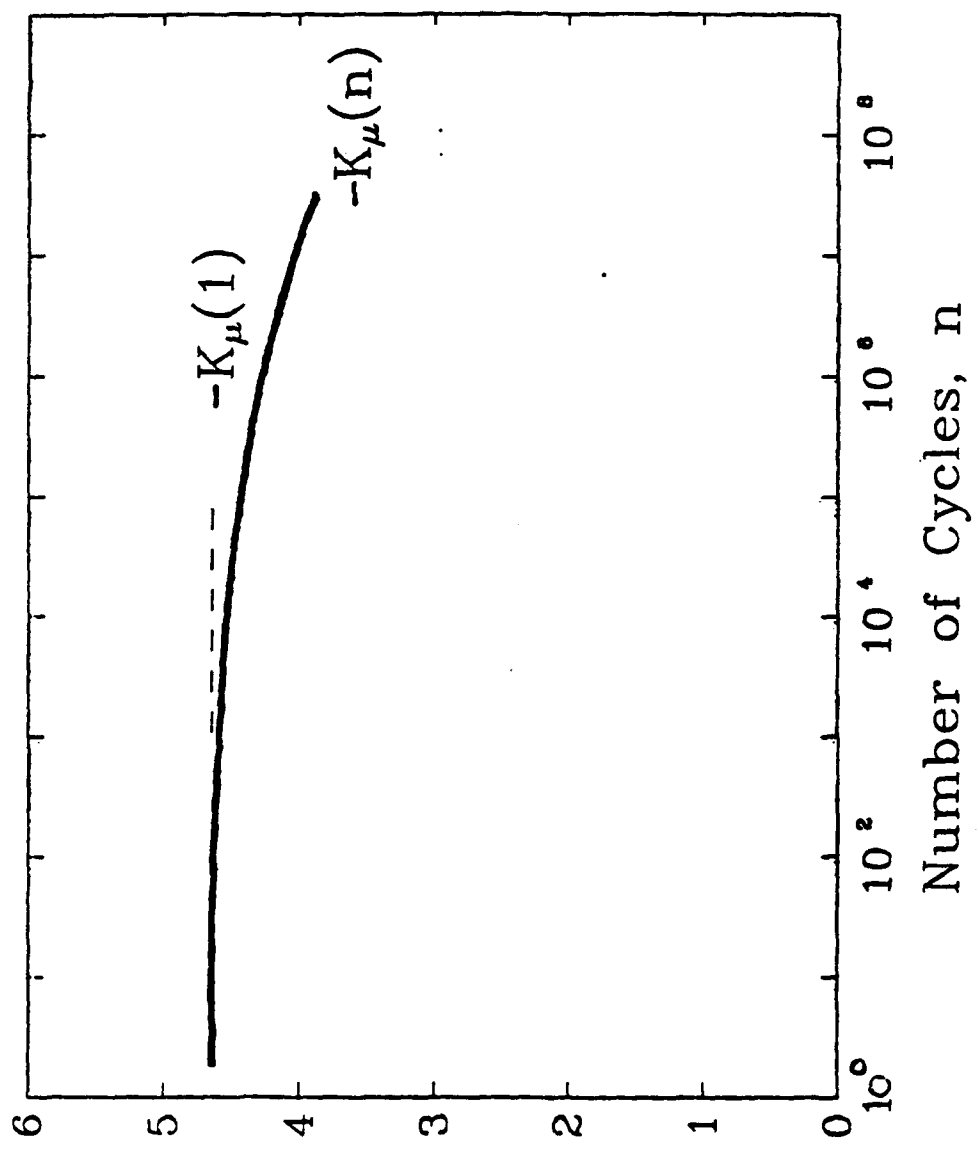












## Role of Grain Size in the Strength and R-Curve Properties of Alumina

Prapaipan Chantikul,<sup>1</sup> Stephen J. Bennison,<sup>\*,‡</sup> and Brian R. Lawn\*

Ceramics Division, National Institute of Standards and Technology, Gaithersburg, Maryland 20899

An investigation of the interrelationships between strength, crack-resistance (R-curve) characteristics, and grain size for alumina ceramics has been carried out. Results of indentation-strength measurements on high-density aluminas with uniform grain structures in the size range 2 to 80  $\mu\text{m}$  are presented. A theoretical fit to the data, obtained by adjusting parameters of a constitutive frictional-pullout relation in a grain-bridging model, allows determination of the critical microstructural parameters controlling the R-curve behavior of these aluminas. The primary role of grain size in the toughness characteristic is to determine the scale of grain pullout at the bridged interface. It is shown that the strength properties are a complex function of the bridged microstructure, governed at all but the finest grain sizes by the stabilizing effect of the R-curve. The analysis confirms the usual negative dependence of strength on grain size for natural flaws that are small relative to the grain size, but the dependence does not conform exactly to the  $-1/2$  power predicted on the basis of classical "Griffith-Orowan" flaws. The analysis provides a self-consistent account of the well-documented transition from "Orowan" to "Petch" behavior. [Key words: grain size, strength, R-curve, alumina, bridging.]

### I. Introduction

THE influence of grain size on the strength of intrinsically brittle solids, particularly of aluminas and other noncubic ceramics, has been well documented.<sup>1-14</sup> Generally, the strength is observed to decline with coarsening of the grain structure. An understanding of the strength/grain-size dependence is an important element in the microstructural design of structural ceramics.

The earliest nonempirical accounts of the observed trends<sup>9</sup> were based on the simplistic Griffith concept of spontaneous failure from a dominant flaw. If it is assumed that the intrinsic flaw scales with grain size and that the toughness is single-valued, a so-called "Orowan" relation ensues in which the strength is proportional to the inverse square root of grain size.<sup>15</sup> Most data can be force-fitted reasonably well with this relation down to "intermediate" grain sizes (10 to 40  $\mu\text{m}$  in alumina), at which point the size dependence is markedly reduced.<sup>9,10</sup> This latter region is manifested as a secondary, "Petch" branch of low slope and nonzero intercept on a strength versus (grain size) $^{-1/2}$  diagram.<sup>16</sup> Various interpreta-

tions of the transition have been proposed: a precursor "microplasticity" stage in crack initiation from the flaw<sup>9,10</sup> (from literal adaptations of the original metals-based Hall-Petch model); the stabilizing influence of local (machining, thermal expansion mismatch) residual stresses in the flaw extension<sup>10,17</sup>; the dominance of extrinsic (e.g., machining) flaws in the small-grain-size region,<sup>10,12</sup> with any microstructural dependence attributable to a monocrystal-to-polycrystal increase in the crack resistance.<sup>10,17,18</sup> A common feature of these proposals is that the supporting evidence cited is invariably circumstantial: i.e., the evolution of the critical flaw to final instability is never observed directly. Indeed, there is a persistent school of thought that dismisses all of the above explanations, suggesting instead that (with proper attention to distributions in grain size) the fine-grain region can be represented adequately by an Orowan relation with simple grain-size-independent, extrinsic flaw cutoff.<sup>14</sup>

Central to the continuing debate are the issues of non-unique toughness and crack stability. In the early 1980s efforts were made to construct broad-based models which took into account both these factors.<sup>20-22</sup> Those models used empirical functions to represent a monocrystal-polycrystal transition in toughness and thereby predicted a stable region of crack growth prior to failure. Again, little or no attempt was made to confirm the models with direct experimental observations of flaw micromechanics. The lack of definitive experiments on materials with well-characterized toughness/crack-size properties and properly controlled flaws has not helped to resolve the debate.<sup>14,19,23</sup>

More recently, direct evidence for departures from single-valued toughness in polycrystalline ceramics, predominantly in aluminas<sup>24-29</sup> but also in other (noncubic) materials, has become available. (Typically, for an alumina of grain size  $\approx 20 \mu\text{m}$ , the toughness increases from a value of  $\approx 2$  to  $6 \text{ MPa} \cdot \text{m}^{1/2}$  over a crack extension  $\approx 5 \text{ mm}$ .) This rising toughness, termed "R-curve" (or "T-curve") behavior, becomes more pronounced as the grain size increases.<sup>26,27</sup> Further studies using controlled indentation flaws in alumina<sup>30-35</sup> demonstrate that the R-curve strongly stabilizes crack growth, such that the critical flaw may extend several times its original dimension prior to failure.<sup>31</sup> In situ observations of the indentation flaws (as well as of other well-defined crack geometries) during applied loading unequivocally identify the underlying cause of this stabilization as crack-interface bridging by interlocked grains behind the crack tip.<sup>31,34</sup> These same observations reveal that the crack first propagates through one or two grain diameters and then arrests ("pop-in"), and thereafter grows erratically during the prefailure growth.<sup>31</sup> The failure condition shows strong departures from Griffith behavior, with a pronounced tendency for the strength to become independent of indentation load in the small-flaw domain ("flaw tolerance").<sup>30,33,35,36</sup>

Theoretical fracture mechanics treatments of the crack-bridging process have been developed on the basis of frictional grain pullout.<sup>32,33,36</sup> The most recent analysis<sup>36</sup> makes a special effort to incorporate essential elements of the microstructure into the fundamental constitutive relation for the pullout, especially the role of thermal expansion anisotropy

R. Cook—contributing editor

Manuscript No. 197864. Received December 21, 1989; approved May 2, 1990.

Presented at the 92nd annual Meeting of the American Ceramic Society, Dallas, TX, April, 1990.

Supported by a grant from the U.S. Air Force Office of Scientific Research.

\*Member, American Ceramic Society.

<sup>†</sup>Guest Scientist, on leave from the Physics Department, Faculty of Science, Chulalongkorn University, Bangkok, Thailand BKK10330.

<sup>‡</sup>Guest Scientist, on leave from the Department of Materials Science and Engineering, Lehigh University, Bethlehem, PA 18015.

stresses in augmenting grain-boundary friction. The model is thereby able to account for the observed tendency to more pronounced *R*-curves with coarsening microstructure. More appropriately, it has the necessary ingredients for a universal characterization of the grain-size dependence of strength, over a broad spectrum of flaw sizes (subgrain to multigrain) and types ("natural" as well as indentation).<sup>36</sup> Interestingly, the predicted dependence for natural flaws in the coarse-grained region can be significantly less than the power  $-1/2$  of Griffith-Orowan. A preliminary comparison with some literature data on alumina appeared to substantiate this predicted departure from ideal behavior.<sup>36</sup>

In the present study we investigate the interrelationship between strength and grain size in greater depth. Indentation-strength experiments are conducted on high-density aluminas with uniform grain structures in the size range 2 to 80  $\mu\text{m}$ . The surfaces of the specimens are finely polished to minimize the intrusion of extrinsic flaws. It is confirmed that strength is a multiregion function of grain size, governed at all but the finest microstructures ( $\leq 5 \mu\text{m}$  in our alumina) by the stabilizing effect of the *R*-curve. Analysis of the data in terms of the grain-bridging model provides a self-consistent account of the strength properties. For very small flaws the negative grain-size dependence of strength indeed differs (if only slightly) from power  $-1/2$ ; for very large flaws the dependence is the same in the coarse-grain region, somewhat lower but still negative in the intermediate-grain region, and is actually predicted to become slightly positive in the fine-grain region. A fit of the grain-bridging model to the data, obtained by adjusting microstructural quantities in the constitutive frictional pullout law, allows deconvolution of the critical *R*-curve parameters for the alumina.

## II. Experimental Procedure

### (1) Preparation of Alumina Specimens

A fabrication procedure based on the Lucalox<sup>8</sup> process<sup>37,38</sup> was used to produce high-density, single-phase  $\alpha\text{-Al}_2\text{O}_3$  specimens with homogeneous, equiaxed grain structures. Powder preparation was carried out in class A-100 clean-room conditions. Ultra-high-purity  $\text{Al}_2\text{O}_3$  powder<sup>9</sup> was doped with trace  $\text{MgO}$  ( $\text{Mg}/\text{Al} = 500$  at. ppm, i.e., below the solid solubility limit for Mg in  $\text{Al}_2\text{O}_3$  at the firing temperatures used below)<sup>39</sup> by addition of a magnesium nitrate solution in methanol. The slurry was continuously stirred during drying and then deagglomerated by crushing. Disks 25 mm in diameter and 5 mm in thickness were fabricated by uniaxial pressing at 50 MPa using a high-purity graphite die, punch, and spacer assembly. Removal of any textural defects associated with nonhydrostatic pressures was achieved by subsequent wet-bag isostatic pressing at 350 MPa. A green density  $\approx 55\%$  of the theoretical limit was attained by this procedure.

The green disks were packed in loose powder of identical composition in high-purity alumina crucibles for heat treatment. Two firing stages were employed. The first consisted of calcining at 1150°C in air for 24 h followed by sintering at 1550°C for 30 min ( $\text{MoSi}_2$  resistance furnace). This yielded specimens of  $\geq 99\%$  density with 1.8- $\mu\text{m}$  grain size. The second stage involved postsintering heat treatments under reducing conditions ( $\text{N}_2$  gas, graphite-element furnace), in separate batches at prescribed hold times and at temperatures between 1550° and 1800°C. This promoted grain growth, producing specimens in the grain-size range 2 to 80  $\mu\text{m}$ . All heating cycles were carried out at a maximum heating/cooling rate of 500°C/h.

Sample specimens from each batch were subjected to microstructural characterization. Densities were measured by the

Archimedes method using water as the immersion medium.<sup>40</sup> Surfaces were prepared for optical microscopy by diamond polishing to 1  $\mu\text{m}$ . The microstructures were revealed by thermal etching (air, 1550°C, 12 min) and the grain diameters measured using the linear intercept technique.<sup>41</sup> Unetched specimens were examined in transmitted light for the incidence of spontaneous microcracking.

### (2) Indentation-Strength Testing

Prior to testing, each remaining disk was machined to a thickness of 2.5 mm and the prospective tensile face diamond-polished to a 1- $\mu\text{m}$  finish. Most specimens were indented at their face centers with a Vickers diamond pyramid at contact loads between 0.2 and 200 N. Some were left unindented as controls. All indentations were made in laboratory ambient and allowed to stand for 10 min. Biaxial strength tests were then made using a flat circular punch (4-mm diameter) on a three-point support (15-mm diameter).<sup>42</sup> A drop of silicone oil was placed onto the indentations prior to testing, and failure times were kept below 20 ms, to minimize effects from moisture-assisted kinetic crack growth. "Inert" strengths were calculated from the breaking loads and specimen dimensions using thin-plate formulas.<sup>42</sup> Special care was taken to examine all specimens after failure in the optical microscope to verify the contact site as the origin of failure. Breaks that did not pass through the indentations were incorporated into the data pool for unindented controls.

Optical and scanning electron microscopy was also used to examine the fracture surfaces to determine the relative amounts of intergranular and transgranular cracking.

## III. Experimental Results

### (1) Characterization of Microstructure and Fracture Surfaces

Figure 1 shows representative microstructures of two aluminas, at opposite extremes of grain size. The grain structures are equiaxed and of narrow size distribution (maximum diameter  $<$  twice mean diameter—"Hillert's criterion"<sup>43</sup>), as is appropriate to an investigation of a size effect. Such equiaxed structures may be taken as circumstantial evidence for the lack of any intergranular glassy phases.<sup>44</sup> The defect population in Fig. 1 appears to consist predominantly of surface-intersected pores at triple-point junctions (seen to better advantage in Fig. 1(B)) and occasional grain pullouts due to polishing (e.g., at upper right in Fig. 1(A)). The small scale of the defects indicates that we have attained high density: actual measurements yield  $\geq 99\%$  of theoretical density at all grain sizes.

The translucence of our materials also allowed the internal flaw population to be investigated in the bulk material, using transmitted light. Figure 2 is an example. Small pores are again evident on a substantial fraction of the triple-point sites. Such pores can be effective sources of grain-facet cracking and are thereby believed to constitute a principal component of the intrinsic flaw population in our materials. More apparent are extended microcracks, on the order of two to three grain-facet dimensions, which have generated spontaneously under the action of local thermal expansion anisotropy stresses during the processing. The first incidence of such microcracks was observed at grain sizes as low as 35  $\mu\text{m}$ , beyond which the number density increased markedly with coarsening of the microstructure.

Figure 3 shows fracture surfaces of the same aluminas in Fig. 1, after biaxial strength testing. These micrographs reveal a mixture of fracture modes,  $\approx 70\%$  intergranular and  $\approx 30\%$  transgranular in our aluminas. This represents a somewhat larger proportion of transgranular mode than noted in our previous studies using a commercial alumina, which was characterized by a distinctly less uniform grain structure.<sup>45,46</sup>

<sup>8</sup>Polymers Product Division, General Electric Co., Pittsfield, MA.

<sup>9</sup>AKP-HP grade (99.995% pure, 0.5- $\mu\text{m}$  crystallites), Sumitomo Chemical America, New York.

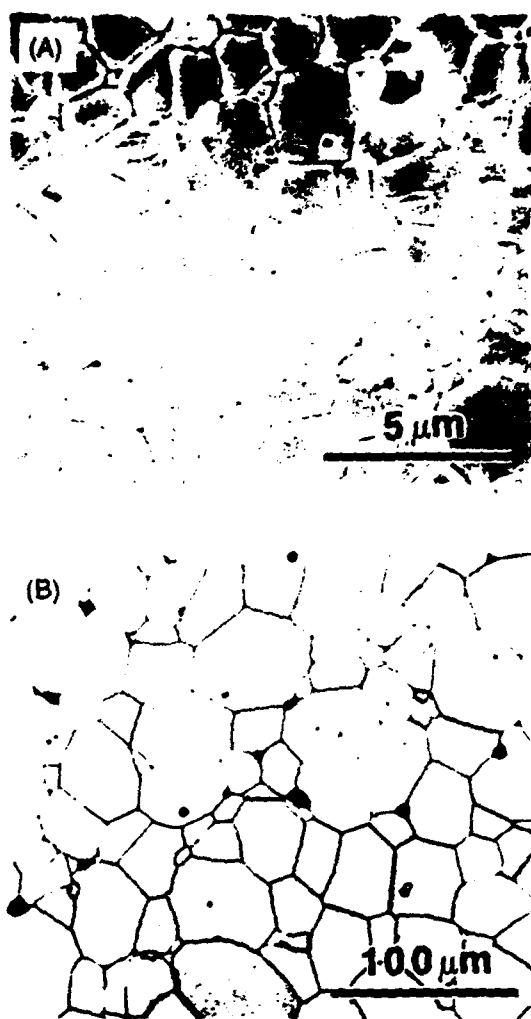


Fig. 1. Microstructure of polished alumina surfaces: (A) SEM,  $\ell = 2.5 \mu\text{m}$ ; (B) optical, reflected light,  $\ell = 79.8 \mu\text{m}$ . Surfaces have been thermally etched to reveal grain structure.

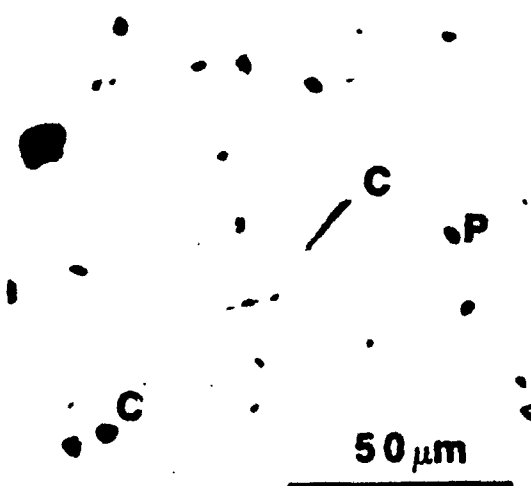


Fig. 2. Optical micrograph of alumina of grain size  $\ell = 35 \mu\text{m}$ , transmitted light. Note the triple-point pores (P) and extended microcracks (C-C).

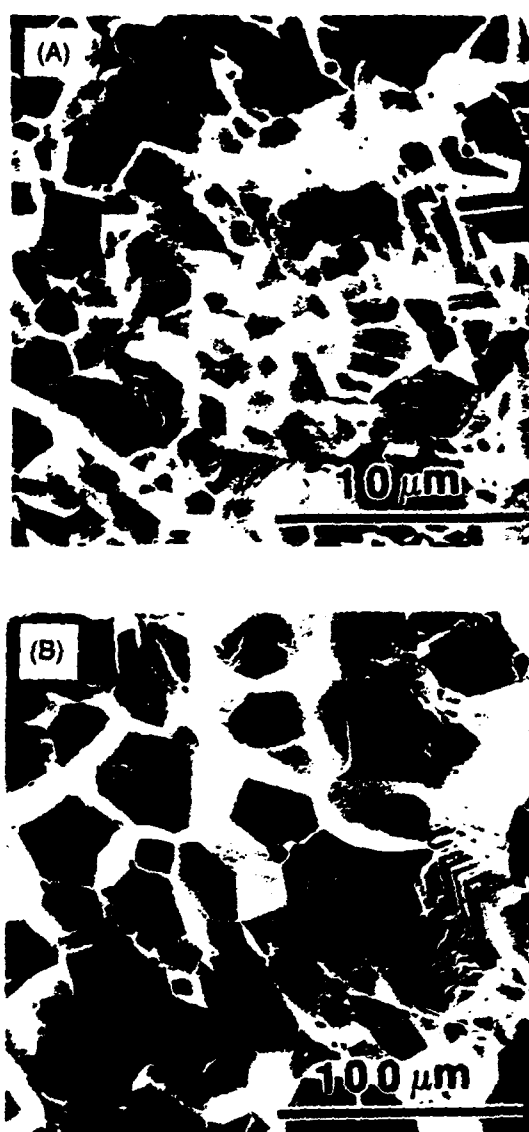


Fig. 3. Scanning electron micrographs of alumina fracture surfaces, grain sizes (A)  $\ell = 2.5$  and (B)  $\ell = 79.8 \mu\text{m}$  (same specimens as Fig. 1).

Again, we may note the presence of pores at the grain-boundary junctions in Fig. 3.

#### (2) Indentation-Strength Data

Figure 4 plots the measured inert strength as a function of indentation load for each grain size. Each data point represents the mean and standard deviation of an average four indentation-flaw failures; the hatched region at left represents failures from natural flaws. The solid curves through the data are best-fit predictions from the theoretical model, to be described below (Sections IV and V).

The strength data in the individual plots are marked by a distinctive tendency to a plateau at smaller indentation loads.<sup>11</sup> This tendency is a manifestation of the *R*-curve;<sup>30,31,33,34</sup> for materials with single-valued toughness, the strength should follow a simple power-law (load)<sup>-1/3</sup> dependence.<sup>45-47</sup> The

<sup>11</sup>Note that the plateaus in Fig. 4 are asymptotic to the strength levels for natural flaws (hatched regions at left), for all but the finest grain size, i.e.,  $\ell = 2.5 \mu\text{m}$  (Fig. 4(A)). Such gradual, asymptotic transitions are a definitive characteristic of *R*-curve behavior.<sup>11</sup> The more abrupt, nonasymptotic cutoff in Fig. 4(A) is indicative of the dominance of extrinsic flaws. We return to this point in the Discussion.

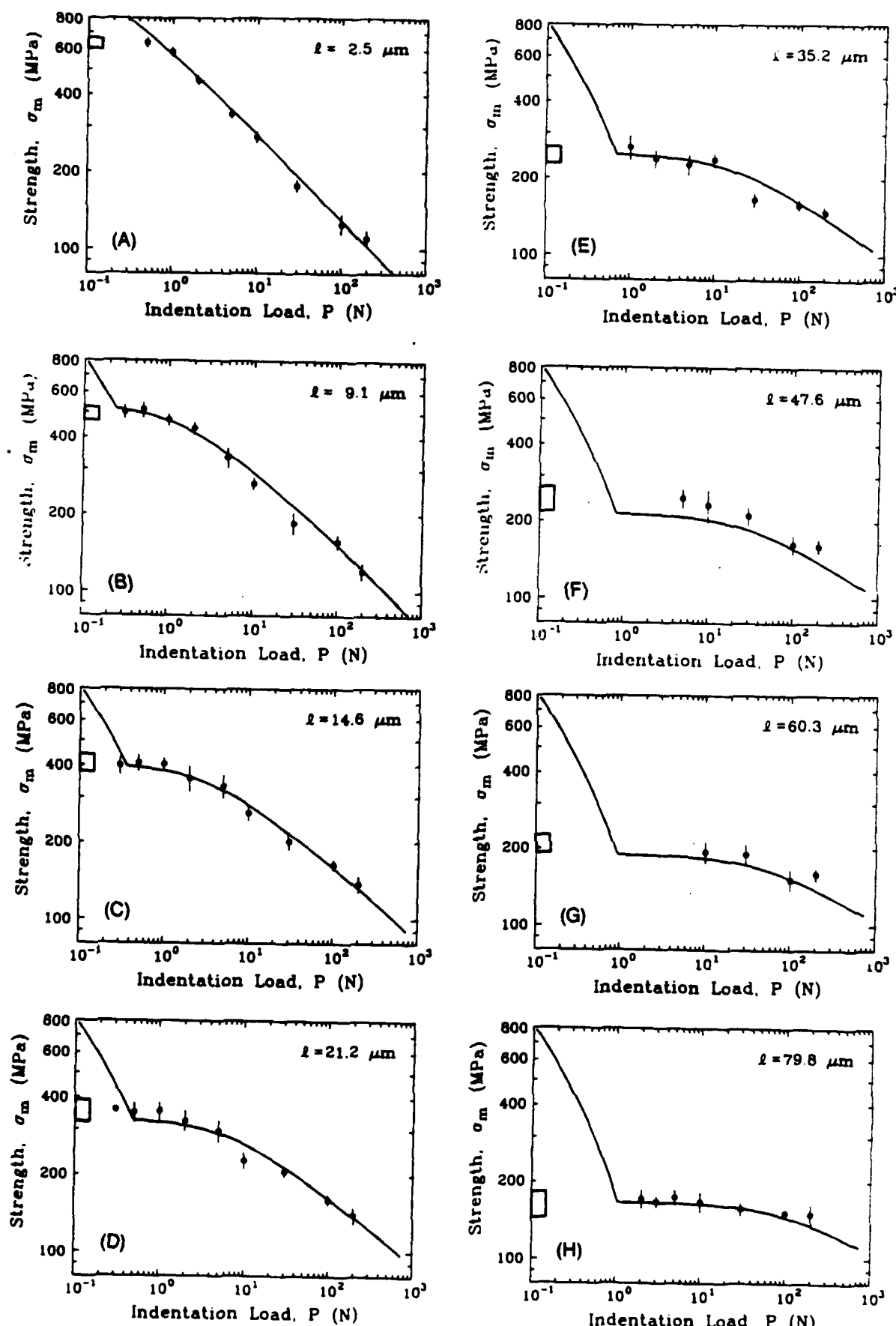


Fig. 4. Plots of inert strength  $\sigma_m$  versus indentation load  $P$ , for aluminas of grain size (A)  $\ell = 2.5 \mu\text{m}$ , (B)  $\ell = 9.1 \mu\text{m}$ , (C)  $\ell = 14.6 \mu\text{m}$ , (D)  $\ell = 21.2 \mu\text{m}$ , (E)  $\ell = 35.2 \mu\text{m}$ , (F)  $\ell = 47.6 \mu\text{m}$ , (G)  $\ell = 60.3 \mu\text{m}$ , and (H)  $\ell = 79.8 \mu\text{m}$ . Curves are best fit from bridging model in Sections IV and V.

strength plateau is lower, but stronger (i.e., persists over a greater range of contact load), at larger grain sizes. One may also note a disposition for the data sets at any two grain sizes to cross each other at some point along the load axis. We shall discuss these trends in relation to transitions from Orowan to Petch behavior in Section V.

#### IV. Theory

We summarize here the essence of the grain-bridging theory of  $R$ -curve ( $T$ -curve) and strength characteristics in monophase ceramics as it pertains to grain size.<sup>36</sup> It is implicit in this endeavor that the principle of similitude applies to our materials, i.e., that the microstructure scales geometrically with grain size.

##### (A) Grain-Bridging and $T$ -Curve ( $R$ -Curve)

Begin by defining a general stress intensity factor condition for the equilibrium of a crack subject to an applied tensile loading field,  $K_a(c)$ , a flaw-localized residual nucleation field,  $K_n(c)$ , and a microstructure-associated field,  $K_\mu(c)$ .<sup>32,48,49</sup> Equilibrium obtains when the net crack-tip field,  $K_0(c)$ , just balances the toughness associated with the creation of (intergranular or transgranular) surfaces,  $T_0$ :

$$K_0(c) = K_a(c) + K_n(c) + K_\mu(c) = T_0 \quad (1)$$

This requirement can be restated by considering  $K_a$  and  $K_n$  as part of the net applied mechanical field,  $K_A$ , and  $K_\mu = -T_\mu$  as part of the internal toughness,  $T$ , i.e.

$$\begin{aligned} K_A(c) &= K_a(c) + K_n(c) \\ &= T_0 + T_\mu(c) = T(c) \end{aligned} \quad (2)$$

The toughness function  $T(c)$  constitutes the so-called  $T$ -curve, the  $K$ -field equivalent of the  $R$ -curve.

Our principal aim is to express  $T_\mu(c)$  in terms of grain size and other microstructural variables.<sup>36</sup> The stress-separation micromechanics are assumed to be governed by thermal expansion mismatch stresses, which "clamp" the interlocking bridging grains into the matrix. (We have already noted the manifestations of such internal stresses in relation to the microcracks in Fig. 2.) As the crack walls move apart, the bridging grains debond along the constrained boundary facets and then slide out against frictional tractions at these boundaries until final "rupture" at some critical strain.<sup>31,34</sup> Ignoring the debond stage (which consumes relatively little energy<sup>36</sup>), the constitutive relation between the closure stress  $p$  and (half) crack-opening displacement  $u$  may be written<sup>32,36</sup>

$$p(u) = p_M(1 - u/u_t) \quad (3)$$

where  $p_M$  is the maximum resistance stress (at  $u = 0$ ) and  $2u_t$  is the wall-wall displacement at bridge-matrix disengagement (at  $p = 0$ ). For geometrically similar microstructures, these last two quantities may be determined more explicitly in terms of the grain size  $\ell$ :<sup>36</sup>

$$2u_t = \epsilon_t \ell \quad (4a)$$

$$p_M = (4\epsilon_t \mu \sigma_R)(1 - 1/2\alpha_s^2) \quad (4b)$$

with bridge rupture strain  $\epsilon_t$ , coefficient of sliding friction  $\mu$ , magnitude of internal stress  $\sigma_R$ , and ratio of bridge-spacing to grain-size  $\alpha_s = d/\ell$  all scale-independent parameters. Schematic plots of the constitutive relation are given for different grain sizes in Fig. 5. Note that  $\ell$  enters the formalism exclusively through the grain pullout distance  $u_t$ , and not through the closure stress  $p_M$ .

Now consider the evolution of a half-penny crack, radius  $c$ , through the microstructure, Fig. 6. The solution for  $T_\mu(c)$  may be subdivided into three domains.<sup>36</sup>

(A) Small Cracks: ( $c < d$ ), no bridge intersections. The crack is assumed to initiate in a region of local matrix tensile

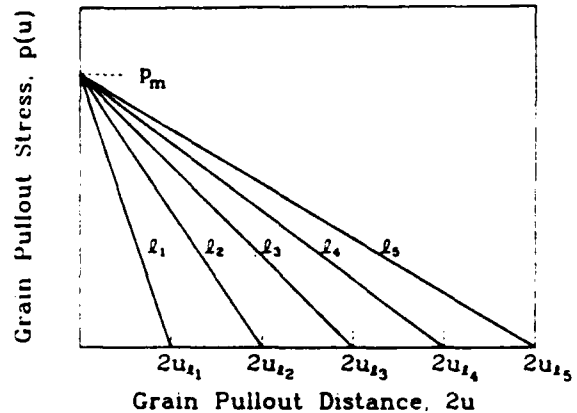


Fig. 5. Schematic plots of constitutive relation Eq. (3) for different grain sizes ( $\ell_1 < \ell_2 < \ell_3 < \ell_4 < \ell_5$ ). Note that pullout distance  $u_t$  in Eq. (4a) scales linearly with grain size  $\ell$ , but that corresponding stress  $p_M$  in Eq. (4b) is completely independent of  $\ell$ .

residual stress, assumed uniform at  $+\sigma_R$ , whence

$$T_\mu(c) = -\psi \sigma_R c^{1/2} \quad (5)$$

with  $\psi$  a geometry coefficient.

(B) Intermediate Cracks: ( $c > d$ ,  $0 \leq 2u \leq \epsilon_t \ell$ ), bridges intersected. There are two contributions in this region,  $T_\mu(c) = T'_\mu(c) + T''_\mu(c)$ . The first is a persistent, opening post-intersection component from the tensile stress  $+\sigma_R$  in (A); a Green's function integration yields

$$T'_\mu(c) = -\psi \sigma_R c^{1/2} [1 - (1 - \alpha_s^2 \ell^2/c^2)^{1/2}] \quad (6)$$

The second is a countervailing closing component due to the bridging tractions in Eq. (3). One may use the  $J$ -integral to determine the corresponding crack resistance component  $R''_\mu$  in terms of crack-opening displacements.<sup>50</sup>

$$\begin{aligned} J_\mu &= 2 \int_0^{u_z} p(u) du \\ &= 2p_M u_z (1 - u_z/\epsilon_t \ell) = R''_\mu(u_z) \end{aligned} \quad (7)$$

where the displacement  $u_z = u_z(c)$  at the edge of the bridging zone (i.e., point of first bridge intersection at  $c = d = \alpha_s \ell$ , Fig. 6) may be evaluated separately from the approximate

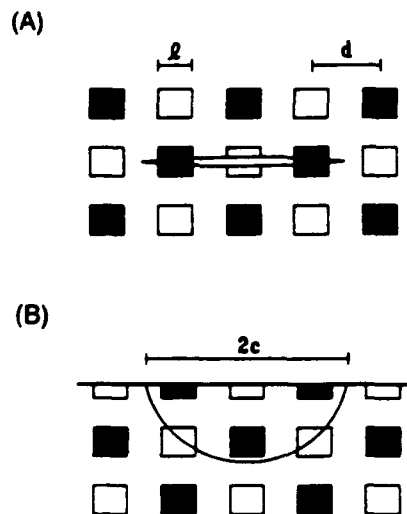


Fig. 6. Schematic of growth of pennylike crack in bridging field: (A) side view, (B) projection view. (Open squares are out-of-plane bridging grains.)

### Sneddon crack profile relation

$$u_z(c) = (\psi K_A/E') [(c^2 - \alpha_d^2 \ell^2)/c]^{1/2} \quad (8)$$

to give  $R''_u(c)$ . The toughness  $T''_u$  may be related to the crack resistance  $R''_u$  by eliminating  $J_A$  and  $K_A$  from the equivalent equilibrium relations  $J_A = T_0^2/E' + R''_u$  and  $K_A = T_0 + T''_u$  (Eq. (2)) via  $J_A = K_A^2/E'$ .<sup>30</sup>

$$T''_u(c) = [E'R''_u(c)]^{1/2} [(1 + T_0^2/E'R''_u(c))]^{1/2} - [T_0^2/E'R''_u(c)]^{1/2} \quad (9)$$

Equation (9) is an implicit function in  $T''_u$ , so Eqs. (2) and (7) to (9) must be solved simultaneously.<sup>30</sup>

(C) *Large Cracks:* ( $c \gg d$ ,  $2u_z \geq \epsilon_c \ell$ ), bridging zone translates with crack, and  $T_u = T'_u + T''_u$  becomes invariant with crack size.

We shall consider the explicit form of  $T(c)$  in specific relation to our aluminas later. For the present we simply emphasize that the contribution to the toughness from the local matrix tensile residual stress is negative (Eqs. (5) and (6)) and thereby diminishes the stability at small crack sizes, whereas the contribution from the frictional pullout is positive (Eq. (9)) and strongly enhances the stability at large crack sizes.<sup>32,33</sup> It is these opposite tendencies at extremes of crack size that account for the spontaneous initiation and arrest of the microcracks in Fig. 2.

### (2) Flaws and Strength Characteristics

Now consider the evolution of flaws through the bridging field under the action of a uniform applied stress  $\sigma_a$ , corresponding to a stress-intensity factor<sup>30,33</sup>

$$K_a = \psi \sigma_a c^{1/2} \quad (10)$$

so that Eq. (2) transposes to

$$\sigma_a(c) = (1/\psi c^{1/2}) [T(c) - K_a(c)] \quad (11)$$

The strength response may then be determined by properly applying the crack instability condition  $d\sigma_a(c)/dc \geq 0$  (equivalent to  $dK_a(c)/dc \geq dT(c)/dc$ ).<sup>48</sup> In relation to Griffith flaws ( $T = T_0 = \text{const}$ ,  $K_a = 0$ ), for which Eq. (11) reduces to a single, monotonically diminishing branch, the stabilizing influence of the  $T(c)$  and  $K_a(c)$  fields is manifest as maxima in the  $\sigma_a(c)$  function.<sup>33,36</sup> Ultimate failure at  $\sigma_a = \sigma_m$  corresponds to the greatest of these maxima.

It remains to specify the quantities  $K_a$  in Eq. (11) and initial sizes  $c$ , for the flaw types of interest. For the controlled Vickers flaws used to obtain the data in Fig. 4, we have<sup>45,51</sup>

$$K_a = \chi P/c^{3/2} \quad (12)$$

with  $P$  the indentation load and  $\chi$  an elastic-plastic contact coefficient;  $c$ , is then determined by the condition  $\sigma_a = 0$  in Eq. (11). For the grain-facet processing flaws which determine the *intrinsic* strength characteristics, we simply set  $K_a = 0$ . According to the observations in Section III(1), the initial size of these flaws is on the order of one grain facet but, to allow conservatively for the possibility of preexisting extended microcracks (Fig. 2), we assume one bridge spacing,  $c = \alpha_d \ell$ . Finally, for *extrinsic* flaws we again set  $K_a = 0$ ; in this case the values of  $c$ , are to be specified independently.

### V. Analysis of Alumina Data in Terms of Bridging Model

Now let us apply the theory of the previous section to obtain fits to the data in Fig. 4 and thence to determine the  $T$ -curves for our aluminas. We do this by choosing initial values for the microstructural parameters and then adjusting these parameters using an iterative algorithm.

#### (1) Regression Algorithm

We begin by specifying first values for the material and geometrical parameters in the strength formulation, using estimates from a previous analysis on a commercial alumina.<sup>36</sup>

Some of these parameters are regarded as invariants in the regression: geometry coefficient  $\psi = 1.24$  (penny cracks),<sup>48</sup> Young's modulus  $E' = 409$  GPa, and indentation flaw parameter  $\chi = 0.018$  ("pure" alumina).<sup>33</sup> Other starting parameters are treated as adjustable:  $T_0 = 2.5 \text{ MPa} \cdot \text{m}^{1/2}$  for the grain-boundary toughness and  $\sigma_R = 155 \text{ MPa}$  for the internal stress; bridge rupture strain  $\epsilon_c = 0.14$  and (normalized) bridge spacing  $\alpha_d = 1.5$ ; and friction coefficient  $\mu = 1.8$ .

The regression algorithm for best fitting the  $\sigma_m(P)$  data is based on a matrix search routine:<sup>33,36</sup> (i) compute trial  $T$ -curve based on starting values of parameters; (ii) evaluate function  $\sigma_a(c)$  in Eq. (11), using all individual (rather than mean) test points, at each indentation load and grain size for which experimental data are available; (iii) determine the inert strength  $\sigma_m$  as the largest maximum in each such  $\sigma_a(c)$  function; (iv) compare predicted strengths with measured values for each set of parameters, and evaluate the net variance in  $\sigma_m$  over all loads and grain sizes; (iv) adjust the floating parameters ( $T_0$ ,  $\sigma_R$ ,  $\epsilon_c$ ,  $\alpha_d$ ,  $\mu$ ), with increasing refinement in the increment size in successive iterations, and thence determine the parameter set with minimum variance.

#### (2) Data Fits and Deconvolution of $T$ -Curves

The best fit to the strength data for our alumina corresponds to the following material parameters:  $T_0 = 2.75 \text{ MPa} \cdot \text{m}^{1/2}$ ,  $\sigma_R = 380 \text{ MPa}$ ,  $\epsilon_c = 0.040$ ,  $\alpha_d = 1.0$ , and  $\mu = 1.6$ ; the standard deviation in  $\sigma_m$  over all data is 17 MPa. This parameter fit is represented by the solid curves in Fig. 4. (Compared with the above starting values from our earlier data fit, we may note an increase in  $T_0$  and  $\sigma_R$ , a decrease in  $\epsilon_c$ .) It can be seen that the theory accounts for the major grain-size dependencies in the indentation-strength data sets, particularly the relative positions and widths of the plateaus and the crossover tendencies. For ready comparison, the curves for the various grain sizes are plotted on the composite diagram of Fig. 7.

Deconvoluted  $T$ -curves resulting from the parameter fit are shown in Fig. 8. The strongly decreasing toughness with crack extension at small crack sizes (negative branch) reflects the high level of local (thermal expansion anisotropy) tensile stress acting on the flaw. After the first bridge intersection at  $c = \alpha_d \ell$  the toughness curves rise markedly (positive branch), especially for the coarser grain structures, reflecting the scaling effect in the grain pullout length. It is this rising por-

<sup>48</sup>Strictly,  $\psi$  should be a function of the ratio of crack length to specimen thickness. In our experiments the maximum crack size at failure was  $\sim 0.5 \text{ mm}$ , i.e., about 20% of the specimen thickness, which leads to a maximum error of  $\sim 7\%$ .<sup>48</sup> This error is considerably smaller than the shifts in strength values from grain size to grain size in Fig. 4 and is neglected here.

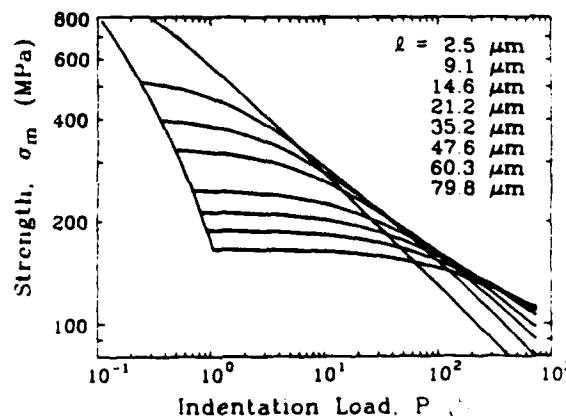


Fig. 7. Composite plot of best-fit  $\sigma_m(P)$  curves for the aluminas in Fig. 4. Note tendency for curves at different grain size to cross over at intermediate indentation loads.

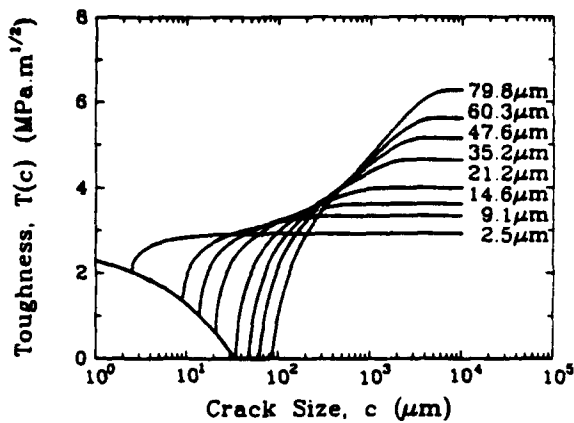


Fig. 8. Toughness curves for aluminas of grain sizes, deconvoluted from theoretical fits in Fig. 7.

tion of the curves that largely determines the strength properties. A flaw which becomes unstable at applied load  $K_A = K_c = \psi\sigma_c c^{1/2}$  (Eq. (10)) on the negative branch just to the left of the minimum propagates unstably and arrests on the positive branch; this accounts for the "pop-in" behavior observed experimentally.<sup>31</sup> The particular curve for which the condition  $c = \alpha_d \ell$  coincides with the abscissa ( $K_A = T = 0$  in Eq. (2)) determines the critical grain size for spontaneous pop-in; from Fig. 8 we estimate  $\ell = 30 \mu\text{m}$  for our alumina, consistent with the first observation of microcracking in Fig. 2.

From the parameter fits in Fig. 4 we determine the strength/grain-size characteristic for *intrinsic* flaws ( $K_c = 0$ ) shown in Fig. 9. Recall our assumption of an initial size  $c_i = \alpha_d \ell$  for such flaws; in fact, the computed strength curve is insensitive to wide variations in this initial flaw size,<sup>32</sup> as befits a truly intrinsic property. The predicted curve has a slope close to, but not exactly,  $-1/2$ ; nor, indeed, is the curve linear on the logarithmic plot. Note that only the data point corresponding to the very smallest grain size deviates significantly from this curve, suggesting that the stabilizing influence of the  $T(c)$  function exerts a controlling influence in all but the finest microstructures.

## VI. Discussion

The bridging model accounts for the main features of the indentation strength-load response for our aluminas. It explains, in particular, the flaw tolerance qualities apparent in the data of Fig. 4 and thereby accentuates the inadequacy of the simple Griffith flaw concept. It is no longer valid to consider toughness  $T$  as a material constant (although the intrin-

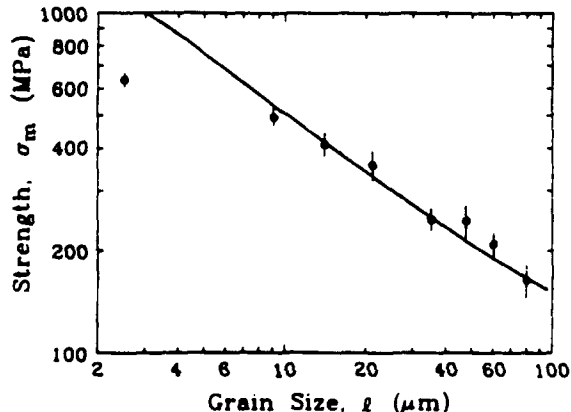


Fig. 9. Strength versus grain size for alumina. Data points are breaks from specimens without indentations; solid curve is prediction for intrinsic, microstructure-controlled flaws using indentation-strength parameters from Fig. 4.

sic grain-boundary toughness  $T_0$  is invariant) or the critical flaw size at final instability to be proportional to grain size: the stabilizing influence of the  $T$ -curve fundamentally and dramatically transforms the micromechanics of failure.

We noted the capacity of the bridging theory to fit all the major trends in the alumina indentation-strength data of Fig. 4, over the entire range of grain sizes covered. Because there are several adjustable parameters involved in this fit, the "agreement" cannot be taken as "proof" of the model.<sup>33</sup> The validity of the bridging concept rests with the direct observations of crack evolution reported elsewhere.<sup>31</sup> Once "calibrated", the formalism allows us to quantify the role of grain size (as well as other microstructural variables) in the strength characteristics. Thus we recall that the grain-size exponent in the strength curve for intrinsic flaws in Fig. 9 is close, but not exactly equal, to the value  $-1/2$  for ideal Griffith flaws: there is nothing in the bridging theory to suggest that this exponent should necessarily assume any universal value or indeed that the relation should be power law at all.

In this context it is interesting to compare the fit to the present alumina data with the earlier fit to a commercial alumina.<sup>34</sup> There, a forced power-law fit yielded an exponent closer to  $-1/2$ . Two experimental observations distinguish our material from that used in the earlier study: the microstructure is considerably more uniform in size and shape (the commercial material showed evidence of some abnormal grain growth), and the fracture mode has a stronger transgranular component. This may be correlated with the relatively high grain-boundary toughness  $T_0$  and internal residual stress  $\sigma_R$ , and low bridge rupture strain  $\epsilon_t$ , indicators of grain boundaries which are less susceptible to debonding, hence pullout. Here is an example where an element of control in microstructural development could be counterproductive: comparative examination of the indentation-strength data sets confirms that the present materials have less pronounced  $T$ -curves and are therefore less flaw tolerant. The implication is that inhomogeneity and nonuniformity in the microstructure, e.g., elongate grains (to increase  $u$ , in Eq. (4a)<sup>34</sup>), may actually be desirable features from the structural standpoint.

The bridging model also provides insights into the role of flaw states in the Orowan-Petch transition referred to in Section I. To illustrate, we replot from Fig. 9 the strength data for unindented surfaces as a function of inverse square root grain size in Fig. 10. Included in Fig. 10 are the corresponding predicted responses for intrinsic flaws (solid curve,  $K_c = 0$ ,  $c_i = \alpha_d \ell$ ) and extrinsic flaws (dashed curve,  $K_c = 0$ ,  $c_i$  as

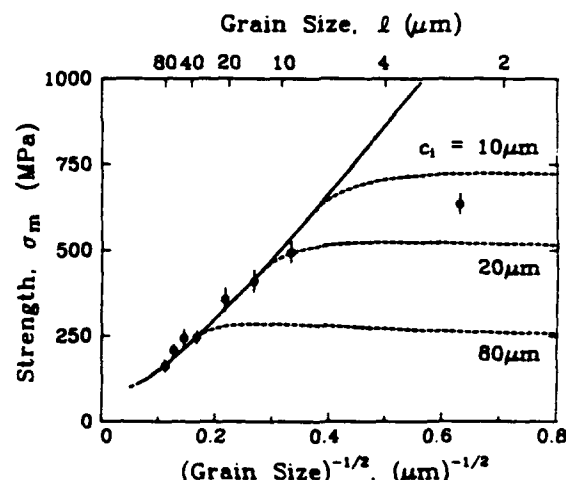


Fig. 10. Similar to Fig. 9, but with abscissa replotted as inverse square root of grain size, with data points again for unindented specimens and solid curve for intrinsic flaws. Also included as dashed curves are predictions for extrinsic flaws of specified initial size  $c_i$ . Note insensitivity of strength to flaw characteristics in large-grain-size domain.

specified). We note that the dashed and solid curves merge in the large grain-size (Orowan) domain. The insensitivity of the predictions to any assumptions concerning type or size of initial flaw in this domain (attributable to the *T*-curve stabilization) indicates a failure condition determined exclusively by material properties. Note again that the solid curve is not exactly linear in this region, as would obtain if true Griffith-Orowan behavior were to prevail.<sup>46</sup> On the other hand, in the small-grain-size (Petch) domain the strengths are highly flaw sensitive, and the dashed curves diverge substantially from the Orowan branch, the more so as  $c$ , increases. On passing into this region, the extrinsic flaws become increasingly larger than their microstructural counterparts and thereby traverse the upper reaches of the *T*-curves in Fig. 8 where precursor stable crack growth prior to failure no longer occurs.<sup>32,48</sup> We note that only one of the data points in Fig. 10, that at the finest grain size ( $\ell = 2.5 \mu\text{m}$ ), appears to fall into the extrinsic domain: this result implies an initial flaw size  $c_i \approx 15 \mu\text{m}$  for our polished surfaces. For the larger extrinsic flaws, the dashed curves in Fig. 10 pass through a slight maximum at fine grain sizes (i.e., into a region in which  $\sigma_m$  actually increases with respect to  $\ell$ ), reflecting the crossover to positive dependence of steady-state toughness on grain size at right in Fig. 8.

The results of the present study have some intriguing implications concerning microstructural design for improved structural materials. We have already alluded to the potential for engineering grain-boundary structures (as they affect  $T_0$ ,  $\sigma_R$ ,  $\epsilon_t$ , etc.) and grain texture (elongate grains) to impart respectable toughness properties to otherwise inherently brittle single-phase ceramics.<sup>36</sup> Perhaps the most far-reaching conclusion to emerge from the analysis is the relatively benign role of processing flaws in ceramics with strong *T*-curve behavior. The relentless elimination of every last defect, as advocated by some,<sup>14,53-55</sup> is not necessarily the ultimate in processing strategies.

Our study has focused on alumina, for which the mechanism of toughening is bridging grain pullout. However, we would emphasize that similar grain-size dependencies are to be expected in any material which exhibits *T*-curve (*R*-curve) behavior, e.g., whether due to incorporated second phases (e.g., fibers, whiskers), phase transformations, microcrack cloud formation, or any other subsidiary energy-dissipative process. This is not to preclude the possibility of ceramics without an *R*-curve, e.g., single-phase cubic ceramics, exhibiting an Orowan-Petch transition; but there the Orowan branch can no longer be defined exclusively by material properties and requires additional detailed specification of the intrinsic-flaw micromechanics.

**Acknowledgments:** The authors acknowledge discussions on different aspects of this work with several colleagues, including T.-J. Chuang, R. F. Cook, E. R. Fuller, Jr., Y.-W. Mai, and D. B. Marshall. We are also grateful to S. Darby for assistance with specimen preparation.

## References

1. B. Cutler, "Strength Properties of Sintered Alumina in Relation to Porosity and Grain Size," *J. Am. Ceram. Soc.*, **40** [1] 20-23 (1957).
2. F. P. Knudsen, "Dependence of Mechanical Strength of Brittle Polycrystalline Specimens on Porosity and Grain Size," *J. Am. Ceram. Soc.*, **42** [8] 376-87 (1959).
3. W. B. Crandall, D. H. Chung, and T. J. Gray, "The Mechanical Properties of Ultra-Fine Hot-Pressed Alumina," pp. 349-76 in *Mechanical Properties of Engineering Ceramics*, Edited by W. W. Kriegel and H. Palmour III, Interscience Publishers, New York, 1961.
4. R. J. Charles and R. R. Shaw, "Delayed Failure of Polycrystalline and Single-Crystal Alumina," General Electric Report No. 62-RL-3081 M, 1962.
5. R. M. Spriggs and T. Vasilos, "Effect of Grain Size on Transverse Bend Strength of Alumina and Magnesia," *J. Am. Ceram. Soc.*, **46** [5] 224-28 (1963).
6. R. M. Spriggs, J. B. Mitchell, and T. Vasilos, "Mechanical Properties of Pure, Dense Aluminum Oxide as a Function of Temperature and Grain Size," *J. Am. Ceram. Soc.*, **47** [7] 323-27 (1964).
7. E. M. Passmore, R. M. Spriggs, and T. Vasilos, "Strength-Grain Size-Porosity Relations in Alumina," *J. Am. Ceram. Soc.*, **48** [1] 1-7 (1965).
8. D. B. Banns and P. Popper, "Mechanical Properties of Some Commercial Alumina Ceramics," *Proc. Br. Ceram. Soc.*, **6**, 71-82 (1966).
9. S. C. Carniglia, "Reexamination of Experimental Strength-vs-Grain Size Data for Ceramics," *J. Am. Ceram. Soc.*, **55** [5] 243-49 (1972).
10. R. W. Rice, "Strength/Grain Size Effects in Ceramics," *Proc. Br. Ceram. Soc.*, **20**, 205-57 (1972).
11. A. G. Evans and G. Tappin, "Effects of Microstructure on the Stress to Propagate Inherent Flaws," *Proc. Br. Ceram. Soc.*, **20**, 275-97 (1972).
12. R. E. Tressler, R. A. Langensiepen, and R. C. Bradt, "Surface-Finish Effects on Strength vs Grain Size Relations in Polycrystalline  $\text{Al}_2\text{O}_3$ ," *J. Am. Ceram. Soc.*, **57** [5] 226-27 (1974).
13. E. Dörre and H. Hübner, *Alumina: Processing, Properties and Applications*; Ch. 3, Springer-Verlag, New York, 1984.
14. N. McN. Alford, K. Kendall, and J. D. Birchall, "Strength/Microstructure Relation in  $\text{Al}_2\text{O}_3$  and  $\text{TiO}_2$ ," *Adv. Ceram. Mater.*, **3** [2] 113-17 (1988).
15. E. Orowan, "Fracture and Strength of Solids," *Rep. Prog. Phys.*, **12**, 186-232 (1948).
16. N. J. Petch, "Cleavage Strength of Polycrystals," *J. Iron Steel Inst., London*, **174** [1] 25-28 (1953).
17. R. W. Rice, S. W. Freiman, R. C. Pohanka, J. J. Mecholsky, Jr., and C. C. Wu, "Microstructural Dependence of Fracture Mechanics Parameters in Ceramics"; pp. 849-76 in *Fracture Mechanics of Ceramics*, Vol. 4, Edited by R. C. Bradt, D. P. H. Hasselman, and F. F. Lange, Plenum Press, New York, 1978.
18. R. W. Rice, S. W. Freiman, and J. J. Mecholsky, "Dependence of Strength-Controlling Fracture Energy on the Flaw Size to Grain Size Ratio," *J. Am. Ceram. Soc.*, **63** [3-4] 129-36 (1980).
19. V. D. Krstic, "Grain-Size Dependence of Fracture Stress in Anisotropic Brittle Solids," *J. Mater. Sci.*, **23** [1] 259-66 (1988).
20. J. P. Singh, A. V. Virkar, D. K. Shetty, and R. S. Gordon, "Strength-Grain Size Relations in Polycrystalline Ceramics," *J. Am. Ceram. Soc.*, **62** [3-4] 179-83 (1979).
21. A. G. Evans, "Dimensional Analysis of the Grain-Size Dependence of Strength," *J. Am. Ceram. Soc.*, **63** [1-2] 115-16 (1980).
22. A. V. Virkar, D. K. Shetty, and A. G. Evans, "Grain-Size Dependence of Strength," *J. Am. Ceram. Soc.*, **64** [3] C-56-C-57 (1981).
23. R. W. Rice and D. Lewis, "Limitations and Challenges in Applying Fracture Mechanics to Ceramics"; pp. 659-76 in *Fracture Mechanics of Ceramics*, Vol. 5, Edited by R. C. Bradt, A. G. Evans, D. P. H. Hasselman, and F. F. Lange, Plenum Press, New York, 1983.
24. H. Hübner and W. Jillek, "Sub-Critical Crack Extension and Crack Resistance in Polycrystalline Alumina," *J. Mater. Sci.*, **12** [1] 117-25 (1977).
25. R. Knehans and R. W. Steinbrech, "Memory Effect of Crack Resistance During Slow Crack Growth in Notched  $\text{Al}_2\text{O}_3$  Bend Specimens," *J. Mater. Sci. Lett.*, **1** [8] 327-29 (1982).
26. R. W. Steinbrech, R. Knehans, and W. Schaarwächter, "Increase of Crack Resistance During Slow Crack Growth in  $\text{Al}_2\text{O}_3$  Bend Specimens," *J. Mater. Sci.*, **18** [10] 265-70 (1983).
27. R. Knehans and R. W. Steinbrech, "Effect of Grain Size on the Crack Resistance Curves of  $\text{Al}_2\text{O}_3$  Bend Specimens"; pp. 613-19 in *Science of Ceramics*, Vol. 12, Edited by P. Vincenzini, Ceramurgia, Imola, Italy, 1984.
28. M. V. Swain, "R-Curve Behavior in a Polycrystalline Alumina Material," *J. Mater. Sci. Lett.*, **5** [12] 1313-15 (1986).
29. R. W. Steinbrech and O. Schmenkel, "Crack-Resistance Curves of Surface Cracks in Alumina," *J. Am. Ceram. Soc.*, **71** [5] C-271-C-273 (1988).
30. R. F. Cook, B. R. Lawn, and C. J. Fairbanks, "Microstructure-Strength Properties in Ceramics: I, Effect of Crack Size on Toughness," *J. Am. Ceram. Soc.*, **68** [11] 604 (1985).
31. P. L. Swanson, C. J. Fairbanks, B. R. Lawn, Y.-W. Mai, and B. J. Hockey, "Crack-Interface Grain Bridging as a Fracture Resistance Mechanism in Ceramics: I, Experimental Study on Alumina," *J. Am. Ceram. Soc.*, **70** [4] 279-89 (1987).
32. Y.-W. Mai and B. R. Lawn, "Crack-Interface Grain Bridging as a Fracture Resistance Mechanism in Ceramics: II, Theoretical Fracture Mechanics Model," *J. Am. Ceram. Soc.*, **70** [4] 289-94 (1987).
33. R. F. Cook, C. J. Fairbanks, B. R. Lawn, and Y.-W. Mai, "Crack Resistance by Interfacial Bridging: Its Role in Determining Strength Characteristics," *J. Mater. Res.*, **2** [3] 345-56 (1987).
34. P. L. Swanson, "Crack-Interface Traction: A Fracture-Resistance Mechanism in Brittle Polycrystals"; pp. 135-55 in *Advances in Ceramics*, Vol. 22, *Fractography of Glasses and Ceramics*, American Ceramic Society, Columbus, OH, 1988.
35. S. J. Bennison and B. R. Lawn, "Flaw Tolerance in Ceramics with Rising Crack-Resistance Characteristics," *J. Mater. Sci.*, **24** [9] 3169-75 (1989).
36. S. J. Bennison and B. R. Lawn, "Role of Interfacial Grain-Bridging Sliding Friction in the Crack-Resistance and Strength Properties of Nontransforming Ceramics," *Acta Metall.*, **37** [10] 2659-71 (1989).
37. R. L. Coble, "Sintering of Crystalline Solids—II. Experimental Test of Diffusion Models in Porous Compacts," *J. Appl. Phys.*, **32** [5] 793-99 (1961).
38. S. J. Bennison and M. P. Harmer, "A History of the Role of  $\text{MgO}$  in the Sintering of  $\alpha\text{-Al}_2\text{O}_3$ ," *Ceramic Transactions*, Vol. 7, *Sintering of Advanced Ceramics*, Edited by C. A. Handwerker, J. E. Blendell, and W. A. Kayser.

<sup>46</sup>At very large grain sizes the strength is actually predicted to fall to zero, corresponding to unlimited unstable extension of the intrinsic flaws. Material compacts with microstructures on this scale will tend to fail spontaneously on cooling from the processing temperature.

American Ceramic Society, Westerville, OH, 1989.

<sup>10</sup>S. K. Roy and R. L. Coble, "Solubilities of Magnesia, Titania, and Magnesium Titanate in Aluminum Oxide," *J. Am. Ceram. Soc.*, 51(1) 1-6 (1968).

<sup>11</sup>E. C. M. Pennings and W. Grellner, "Precise Nondestructive Determination of the Density of Porous Ceramics," *J. Am. Ceram. Soc.*, 72(2) 1268-70 (1989).

<sup>12</sup>J. C. Wurst and J. A. Nelson, "Lineal Intercept Technique for Measuring Grain Size in Two-Phase Polycrystalline Ceramics," *J. Am. Ceram. Soc.*, 55(2) 109 (1972).

<sup>13</sup>D. B. Marshall, "An Improved Biaxial Flexure Test for Ceramics," *Am. Ceram. Soc. Bull.*, 55(5) 551-53 (1980).

<sup>14</sup>M. Hillert, "Theory of Normal and Abnormal Grain Growth," *Acta Metall.*, 13(3) 227-38 (1965).

<sup>15</sup>C. A. Bateman, S. J. Bennison, and M. P. Harmer, "Mechanism for the Role of Magnesia in the Sintering of Alumina Containing Small Amounts of a Liquid Phase," *J. Am. Ceram. Soc.*, 72(7) 1241-44 (1989).

<sup>16</sup>D. B. Marshall and B. R. Lawn, "Residual Stress Effects in Sharp-Contact Cracking: I. Indentation Fracture Mechanics," *J. Mater. Sci.*, 14(9) 2001-12 (1979).

<sup>17</sup>D. B. Marshall, B. R. Lawn, and P. Chantikul, "Residual Stress Effects in Sharp-Contact Cracking: II. Strength Degradation," *J. Mater. Sci.*, 14(9) 2225 (1979).

<sup>18</sup>B. R. Lawn, "The Indentation Crack as a Model Indentation Flaw," pp. 1-25 in *Fracture Mechanics of Ceramics*, Vol. 5. Edited by R. C. Bradt,

A. G. Evans, D. P. H. Hasselman, and F. F. Lange. Plenum Press, New York, 1983.

<sup>19</sup>Y.-W. Mai and B. R. Lawn, "Crack Stability and Toughness Characteristics in Brittle Materials," *Annu. Rev. Mater. Sci.*, 16, 415-39 (1986).

<sup>20</sup>B. R. Lawn and T. R. Wilshaw, *Fracture of Brittle Solids*; Ch. 3. Cambridge University Press, London, U.K., 1975.

<sup>21</sup>R. F. Cook, "Transient Fracture Resistance in the Weak Toughening Limit," pp. 2747-55, in *Advances in Fracture Research*, I.C. F. 7. Edited by K. Salama, R. Ravi-Chandra, D. M. R. Taplin, and P. Rama-Rao. Pergamon Press, New York, 1989.

<sup>22</sup>B. R. Lawn, A. G. Evans, and D. B. Marshall, "Elastic/Plastic Indentation Damage in Ceramics: The Median/Radial Crack System," *J. Am. Ceram. Soc.*, 63(9-10) 574-81 (1980).

<sup>23</sup>J. C. Newman, Jr., and I. S. Raju, "An Empirical Stress-Intensity Factor Equation for the Surface Crack," *Eng. Fract. Mech.*, 15, 185-92 (1981).

<sup>24</sup>F. F. Lange, "Processing-Related Fracture Origins: I. Observations in Sintered and Isostatically Hot-Pressed  $\text{Al}_2\text{O}_3/\text{ZrO}_2$  Composites," *J. Am. Ceram. Soc.*, 66(6) 396-98 (1983).

<sup>25</sup>F. F. Lange and M. Metcalf, "Processing-Related Fracture Origins: II. Agglomerate Motion and Cracklike Internal Surface Caused by Differential Sintering," *J. Am. Ceram. Soc.*, 66(6) 398-406 (1983).

<sup>26</sup>F. F. Lange, B. I. Davies, and I. A. Aksay, "Processing-Related Fracture Origins: III. Differential Sintering of  $\text{ZrO}_2$ : Agglomerates in  $\text{Al}_2\text{O}_3/\text{ZrO}_2$  Composite," *J. Am. Ceram. Soc.*, 66(6) 407 (1983). □

**THE ROLE OF CRYSTALLIZATION OF AN INTERGRANULAR GLASSY PHASE IN DETERMINING GRAIN BOUNDARY RESIDUAL STRESSES IN DEBASED ALUMINAS**

NITIN P. PADTURE<sup>1</sup>, HELEN M. CHAN<sup>1</sup>, BRIAN R. LAWN<sup>2</sup> and MICHAEL J. READEY<sup>3</sup>

<sup>1</sup>Department of Materials Science and Engineering, Whitaker Lab # 5, Lehigh University, Bethlehem, PA 18015

<sup>2</sup>Ceramics Division, Bldg. # 223, National Institute of Standards and Technology, Gaithersburg, MD 20899

<sup>3</sup>Coors Ceramics Company, 17750, 32nd Avenue, Golden, CO 80401

**ABSTRACT**

The influence of microstructure on the crack resistance (R-curve) behavior of a commercial debased alumina containing large amounts of glassy phase (28 vol %) has been studied using the Indentation-Strength test. The effect of two microstructural variables, viz. grain size and the nature of the intergranular second phase (glassy or crystalline) has been evaluated. Crystallization of the intergranular glass was carried out in order to generate residual stresses at the grain boundaries, which have been shown to enhance R-curve behavior in ceramic materials. Enhancement of the R-curve behavior was observed with the increase in grain size. However, no effect of the nature of the intergranular second phase on the R-curve behavior, in small and large grain materials, was observed. The results from characterization of these materials using various analytical techniques is presented, together with possible explanations for the observed effects.

**INTRODUCTION**

Recently several researchers [1 to 4] have reported considerable increase in toughness of debased (liquid-phase-sintered) aluminas, containing 10 to 30 vol % intergranular glass, by crystallization of the glass via simple heat-treatments. However, it should be noted that the toughness measurements in the above studies were performed at single crack length values, whereas recent work has shown that many alumina ceramics show increase in toughness with crack length, i.e. crack resistance or R-curve behavior [5 to 10]. The effect of crack resistance has been attributed to the phenomenon of microstructural grain-localized bridging of the crack, in the wake of its tip, and is very sensitive to the microstructure of the material [5, 11]. In the present study we have set out to evaluate the effect of grain size and crystallization of the intergranular glass on the mechanical properties (R-curve behavior) of these materials over a wide range of crack lengths.

The grains bridging the crack, in non-cubic polycrystalline ceramics, have been postulated to be clamped in the matrix by compressive residual stresses generated during cooling from processing temperatures, due to thermal expansion anisotropy present in these materials [12]. These residual stresses play an important role in the bridging phenomenon. The grain size of the polycrystalline ceramic is also known to influence R-curve behavior of these materials [7,13].

Indentation-strength [7, 8] is a very convenient way of monitoring R-curve behavior in ceramic materials. Bending over of the fracture stress versus indentation load curve at the low indentation load end is a direct consequence of R-curve behavior exhibited by the material, and gives rise to a region where the fracture stress is independent of the indentation load (and hence crack size) [15, 16]. An important implication of R-curve behavior, therefore, is that it suggests a degree of flaw tolerance, which is very useful in terms of engineering design. R-curve behavior also has great significance in the wear properties of materials, since this is governed by fracture characteristics at low flaw sizes. More recently it has been postulated that R-curve behavior increases the Weibull modulus of ceramic materials which exhibit such behavior [17].

18].

The purpose of this study was to determine the separate and combined influence(s) of grain size and second phase crystallinity on the R-curve behavior of debased ceramics. The material chosen was Coors AD85 alumina containing about 28 vol % glass. This material was subjected to carefully designed heat-treatments so as to increase the grain size and increase residual stresses at the grain boundaries by crystallization of the intergranular glass. It was envisaged that in doing so, it would be possible to enhance R-curve behavior in these materials.

## EXPERIMENTAL

About 300 samples of AD85 alumina in the form of disks (25mm dia x 3mm) were obtained from Coors Ceramic Company. A series of heat-treatments was carefully devised in order to produce four sets of samples of differing microstructures. Tables I and II show the details of the heat-treatments and the resulting microstructures respectively. The denotation S or L refers to small or large grain size respectively, and C or G refers to crystalline or glassy second phase respectively.

Table I Various heat-treatments, AD85 subjected to.

<u>Material</u>	<u>Heat-treatments</u>	<u>Purpose</u>
AD85-S-G	a) As-received	
AD85-S-C	a) 1400°C for 6 hours, quenched b) 1150°C for 130 hours	Homogenize intergranular glass Crystallize intergranular glass
AD85-L-G	a) 1550°C for 250 hours	Increase grain size
AD85-L-C	b) 1200°C for 130 hours	Crystallize the intergranular glass

Table II Microstructural aspects of AD85 after the heat-treatments.

<u>Material</u>	<u>Grain size</u>	<u>Intergranular phase</u>
AD85-S-G	3μm	Glassy
AD85-S-C	3μm	80% crystalline
AD85-L-G	18μm	Glassy
AD85-L-C	18μm	80% crystalline

Specimens for Transmission Electron Microscopy (TEM) were prepared from the above samples using a dimpler and then ion-beam milling until perforation. TEM investigation was performed on a Phillips EM 400T at an accelerating voltage of 120 keV. Chemical composition of the intergranular glass was determined using Scanning Transmission Electron Microscopy (STEM) and Energy Dispersive Spectroscopy of x-rays (EDS) on the same instrument. Samples were prepared for Scanning Electron Microscopy (SEM) by polishing sections to 1μm grade followed by thermal etching at 1500 °C for 15 minutes.

Mechanical testing of AD85-S-G, AD85-S-C, AD85-L-G and AD85-L-C was carried out as follows. About 50 disk samples of each were polished to 1μm grade on the prospective tensile side. A Vickers indentation was made at the center of the polished surface with loads varying from 2 to 300 N. Some samples were left unindented. The samples were broken in biaxial flexure using the 3-point support and punch fixture. Details of this particular method of mechanical testing have been described elsewhere [7].

## RESULTS AND DISCUSSION

Table III shows the composition of the intergranular glass of AD85-S-G samples after homogenization heat-treatment, as determined by STEM and EDS. This is an average of many different spectra obtained from different regions of the sample. The compositions were observed to be fairly consistent, which implies that the glassy phase is homogeneous. The composition obtained agrees closely with that determined by Weiderhorn et al. [19] for AD85 with the same heat-treatment. Using this composition as the basis, the heat-treatment given in table I was devised. Figure 1 show SEM micrographs of AD85-S-G (grain size 3 $\mu$ m) and AD85-L-G (grain size 18 $\mu$ m). Figures 2 and 3 show TEM micrographs of AD85-S-G and AD85-S-L showing glassy and crystalline intergranular phases respectively. The grain size did not change appreciably during crystallization heat-treatment. The crystalline intergranular phase in AD85-S-C was observed to be mostly anorthite. With this composition it was not possible to achieve 100% crystallinity, thus pockets of residual glassy phase were observed at the triple points.

Table III Average composition of the intergranular glass in AD85.

Oxide	SiO <sub>2</sub>	Al <sub>2</sub> O <sub>3</sub>	MgO	CaO	BaO
Wt%	56.5	27.5	2.1	8.6	5.3

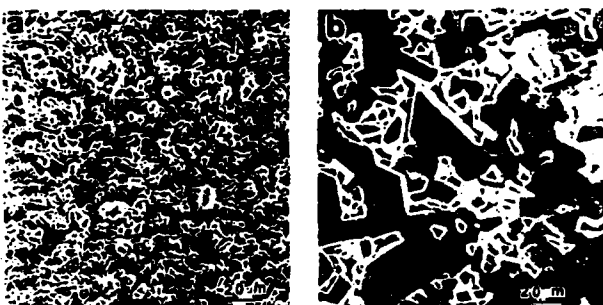


Figure 1 SEM Secondary electron images of polished and etched sections of AD85 aluminas  
a) AD85-S-G (fine grained material), b) AD85-L-G (coarse grained material).



Figure 2 TEM bright field image of AD85-S-G showing intergranular glassy pockets (A-Alumina, G-Glass).



Figure 3 TEM bright field image of AD85-S-C showing crystalline intergranular phase (A-Alumina, C-Crystalline).

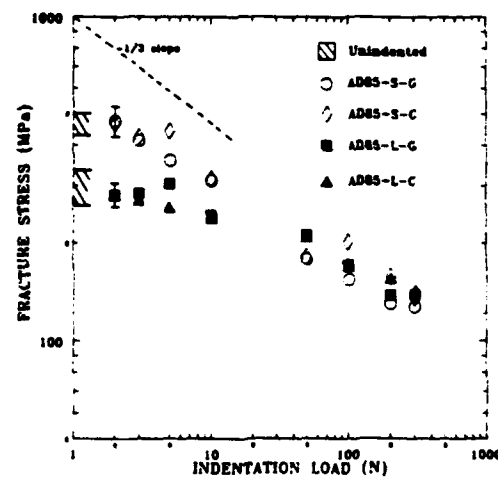


Figure 4 Plot of indentation load versus fracture stress for four different materials, derived from AD85. The error bars for all the data are shown in the left. The hatched region represents failures from natural flaws.

Figure 4 shows indentation load versus fracture stress for AD85-S-G, AD85-S-C, AD85-L-G, and AD85-L-C. It can be seen that all the data essentially falls on two graphs corresponding to 1) fine grained materials (AD85-S-G and AD85-S-C) and 2) coarse grained materials (AD85-L-G and AD85-L-C). It can be clearly seen that coarse grain aluminas show much more pronounced R-curve behavior than fine grain aluminas.

Because the curves for materials with glassy and crystalline intergranular phases show similar behavior, this indicates marginal or no effect of crystallization on the R-curve properties of these materials. The effect of grain size on the R-curve behavior, however, is much more marked, and this is in agreement with results obtained by Cook et al.[7] for single phase aluminas, and Bennison et al. [20] for debased aluminas. Given that grain-bridging processes must be dependent on the residual stresses in the grain boundary regions, the lack of effect of crystallization on the R-curve behavior is somewhat surprising.

Possible explanations for the lack of effect of crystallization of the intergranular glass are thought to be as follows:

1. Stress relaxation by residual glass
2. Fracture through the residual glass
3. Stress relaxation by high temperature deformation (twinning) of anorthite.

Work is currently underway to determine which of the above mechanisms (if any) are correct [21].

## CONCLUSIONS

The major conclusions from the above study can be summarized as follows:

1. The effect of grain size on the R-curve behavior predominates.
2. Crystallization of the intergranular glass has relatively little or no effect on the R-curve behavior of AD85. Possible explanations attributing to the observed behavior have been described above.
3. An important conclusion can however be drawn from the observed behavior. Coors AD85 can be subjected to prolonged heat-treatment cycles up to 1200°C without having any significant effect on room temperature mechanical properties (pertaining to fast crack growth). This property of AD85 can be very useful in prolonged high temperature structural applications and in metallization applications imparting heat-treatment tolerance along with flaw tolerance.

## ACKNOWLEDGEMENTS

The authors wish to thank Dr. S. J. Bennison for many useful discussions.

## REFERENCES

1. N.A. Travitzky, D.G. Brandon and E.Y. Gutmanas, Mater. Sci. Eng., 71, 65-70 (1985).
2. N.A. Travitzky, D.G. Brandon and E.Y. Gutmanas, Mater. Sci. Eng., 71, 77-86 (1985).
3. Y. Yeshurun, Z. Rosenburg, N.A. Travitzky and D.G. Brandon, Mater. Sci. Eng., 71, 71-75 (1985).
4. W.A. Zdaniewski and H.P. Kirchner, Adv. Ceram. Mater., 1, 99-103 (1986).
5. R. Knehans and R. Steinbrech, J. Mater. Sci. Letters, 1, 327-329 (1982).
6. R.W. Steinbrech, R.Knehans and W. Schaarwachter, J. Mater. Sci., 18, 265-270 (1983).

7. R.F. Cook, B.R. Lawn and C.J. Fairbanks, *J. Amer. Ceram. Soc.*, **68**, 604-615 (1985).
8. R. F. Cook, B. R. Lawn, and C. J. Fairbanks, *J. Amer. Ceram. Soc.* **68**, 616-623, (1985).
9. M. V. Swain, *J. Mater. Sci. Letters*, **5**, 1313-1315 (1986).
10. F. Duerler, R. Knehans and R. W. Steinbrech, *J. de Physique*, **C1**, 617-621 (1986).
11. P.L. Swanson, C.J. Fairbanks, B.R. Lawn, Y-W. Mai and B.J. Hockey, *J. Amer. Ceram. Soc.*, **70**, 279-289 (1987).
12. S. J. Bennison and B. R. Lawn, *Acta Metall.*, **37**, 2659-2671, (1989).
13. P. Chanikul, S. J. Bennison and B. R. Lawn, *J. Amer. Ceram. Soc.*, to be published.
14. Y-W. Mai and B. R. Lawn, *J. Amer. Ceram. Soc.*, **70**, 289- 294 (1987).
15. R.F. Cook, C.J. Fairbanks, Y-W. Mai and B.R. Lawn, *J. Mater. Res.*, **2**, 345-356 (1987).
16. S. J. Bennison and B. R. Lawn, *J. Mater. Sci.*, **9**, 3169-3175 (1989).
17. R. F. Cook and D. R. Clarke, *Acta Metall.*, **36**, 555-562 (1988).
18. D. K. Shetty and J-S. Wang, *J. Amer. Ceram. Soc.*, **72**, 1158-1162 (1989).
19. S.M. Wiederhorn, B.J. Hockey and R.F. Krause Jr., *Ceramic Microstructures '86*, edited by J. Pask and A.G. Evans (Plenum Publishing Company, New York, 1988) pp. 795-806.
20. S.J. Bennison, H. M. Chan and B.R. Lawn, *J. Amer. Ceram. Soc.*, **72**, 677-679 (1989).
21. N. P. Padture, H. M. Chan, B. R. Lawn and M. J. Readey, *J. Amer. Ceram. Soc.*, to be published.

**FABRICATION OF FLAW-TOLERANT ALUMINUM-TITANATE-REINFORCED ALUMINA**

Julie L. Runyan\* and Stephen J. Bennison\*\*

Ceramics Division  
National Institute of Standards and Technology  
Gaithersburg, MD 20899

June 1990

For: Journal of the European Ceramic Society

---

\* Summer Student from the Department of Materials Engineering, Virginia Polytechnic Institute and State University, Blacksburg, VA 24061, USA.

\*\* Guest Scientist on leave from the Department of Materials Science and Engineering, Lehigh University, Bethlehem, PA 18015 USA.

Abstract

Fabrication and flaw tolerance behavior of particulate aluminum-titanate-reinforced alumina composites have been studied. High-density (~99 % theoretical) composites with controlled microstructures are readily produced via a conventional ceramics processing scheme using starting powders of  $\alpha$ -alumina and  $\beta$ -aluminum titanate. Indentation-strength measurements demonstrate that these composites are highly flaw tolerant. Direct observations of crack evolution from Vickers indentations during loading reveal a strong crack-stabilization with pre-failure extensions of a millimeter or more. This stabilization gives rise to the flaw tolerance properties and results from pronounced crack-resistance (R-curve) behavior. Grain-localized crack bridging is active in these materials and is believed to be a contributor to the R-curve properties.

## 1 Introduction

One of the more important manifestations of strong rising crack resistance (R-curve, T-curve) behavior [1-9] in ceramics is the reduced sensitivity of strength to the size of processing or service-induced defects; viz: the quality of "flaw tolerance" [7,10,11]. The resulting improvements in reliability as reflected in greater Weibull moduli [12-16] and enhanced fatigue limits [17] make flaw tolerance a desirable property for brittle materials in structural applications.

A variety of phenomena can give rise to R-curves in ceramics [18]. For nontransforming materials with relatively simple microstructures and a predominantly intergranular fracture mode grain-localized crack bridging has been identified as a primary mechanism [19,20]. In this case intact grains bridge the crack walls and apply closure forces that shield the crack tip from the applied stress intensity field [21,22]. These bridging grains are assumed to be "locked" into the microstructure by local thermal expansion anisotropy stresses [9,23]. The important microstructural and material parameters include grain size and shape, intensity of residual stress, grain boundary toughness and friction at the sliding grain-matrix interface [23]. A proper understanding of the role of these parameters opens the way to tailoring the R-curve and flaw tolerance properties through controlled processing [24].

In the present study improvements in the R-curve and flaw tolerance characteristics of alumina are sought through enhancement of the local residual stress levels. The approach is to incorporate a second phase  $\beta$ -aluminum titanate into the  $\alpha$ -alumina matrix. Aluminum titanate exhibits extremely high thermal expansion anisotropy [25] and when added to alumina is

calculated to raise the maximum levels of residual stress by approximately one order of magnitude.<sup>1</sup>

The fabrication of aluminum titanate and alumina/aluminum titanate is usually accomplished via a reaction-sintering route with starting powders of alumina and titania [26-29]. However, unless careful control of the powder characteristics is maintained during processing [30] the resulting microstructures generally display low as-fired densities (<90% theoretical) and abnormal grain growth making them weak, and therefore, generally unsuitable for structural applications.

In the present work a conventional ceramics processing scheme using starting powders of alumina and aluminum titanate is developed whereby composites of high fired densities and controlled grain structures are readily manufactured. The R-curve and flaw tolerance properties are investigated using the indentation-strength technique in which the strength is determined as a function of indentation load [7,10,11,22]. The interaction of cracks with the microstructure is studied using a statically loaded biaxial flexure device mounted either in an optical or scanning electron microscope (SEM). It will be shown that certain composites of  $\alpha$ -alumina reinforced with  $\beta$ -aluminum titanate demonstrate pronounced flaw tolerance resulting from the crack-stabilizing effect of a strong R-curve. The unusual flaw tolerance properties coupled with the ease of fabrication make these composites attractive for applications where components are subjected to damage during service.

---

<sup>1</sup> Based on most severe orientation of alumina and aluminum titanate and using  $\sigma_R = \frac{1}{3}E\Delta\alpha\Delta T$ ; ( $\sigma_R$  - residual stress, E - Young's modulus,  $\Delta\alpha$  - thermal expansion difference,  $\Delta T$  - temperature range over which stresses develop).

## 2 Experimental

### 2.1 Composite Fabrication

All powder processing was carried out in class A-100 clean room conditions. A stable colloid of high-purity  $\alpha$ -Al<sub>2</sub>O<sub>3</sub><sup>2</sup>, the desired volume fraction of  $\beta$ -Al<sub>2</sub>TiO<sub>5</sub><sup>3</sup> and water was prepared by adjusting the pH to  $\approx$  3 with additions of HNO<sub>3</sub>. Drying was carried out using a hot-plate while stirring continuously and the resulting cake was subsequently broken down by crushing in a polyethene bag. Disc-shaped test specimens, 25 mm diameter and 5 mm thickness, were fabricated by uniaxial pressing at 63 MPa using a high-purity graphite die, punch and spacer assembly. Removal of any defects associated with die pressing was achieved by subsequent wet-bag isostatic pressing at 350 MPa. A green density of  $\approx$  55 % of the theoretical limit was attained using this procedure.

Green discs were packed in loose alumina powder in high-purity alumina crucibles for firing using a two-stage heat treatment. The first stage consisted of heating at a rate of 50°C/hr to a calcining temperature of 1050°C with a 12 hr soak. The second stage consisted of heating at a rate of 500°C/hr from the calcining temperature to a sintering temperature of 1600°C with hold times of 1 and 16 hr. Specimens were cooled at  $\approx$  500°C/hr. All heat treatments were carried out in air using a MoSi<sub>2</sub> resistance heated furnace.

---

<sup>2</sup> Sumitomo AKP-HP grade (99.995 % pure, 0.5  $\mu$ m crystallites), Sumitomo Chemical America Inc., 345 Park Ave, New York, NY 10154, USA.

<sup>3</sup> 99.9 %, 1-5  $\mu$ m particle size, Trans-Tech Inc., 5520 Adamstown Rd., Adamstown, MD 21710, USA.

Sample specimens from each batch were subjected to microstructural characterization. Densities were measured by the Archimedes method using water as the immersion medium [31]. Surfaces were prepared, where possible, for optical and scanning electron microscopy (SEM) by diamond-polishing to a 1  $\mu\text{m}$  finish. Microstructures were revealed by thermal etching (air, 1500°C, 6 minutes) and grain sizes were determined by a linear intercept technique [32]. Where polishing was found to be impractical (due to localized spontaneous microfracture) approximate grain sizes were determined from fracture surfaces examined by SEM. Phases present in the composite were identified by X-ray diffraction.

## 2.2 Indentation-Strength Testing

Prior to testing, each fired disc was machined to a thickness of 2.5 mm and the prospective tensile face diamond-polished to a 1  $\mu\text{m}$  finish. Care was taken to ensure that polishing removed the majority of the surface damage introduced during the preliminary machining operation. Most specimens were indented at their face centers with a Vickers diamond pyramid at contact loads between 3-300 N; some discs were left unindented as controls. All indentations were made in laboratory ambient and allowed to stand for 10 min. Biaxial strength tests were then made using a flat circular punch (4 mm diameter) on three-point support (15 mm diameter) [33]. A drop of dry silicone oil was placed on each indentation prior to testing and the failure times were kept below 20 ms to minimize possible effects from moisture assisted non-equilibrium crack growth. "Inert" strengths were calculated from the breaking loads and specimen dimensions using thin-plate formulas [34].

Special effort was made to examine all specimens after testing using optical microscopy to verify the indentation contact site as the origin of failure. Unsuccessful breaks were incorporated into the data pool of unindented controls.

Direct observations of crack extension from indentations during loading were made on selected specimens using a biaxial flexure device mounted on an optical microscope [19]. Crack-microstructure interactions were also investigated using this fixture mounted in an SEM.

### 3 Results

Table 1 lists the salient characteristics of the two composites (20 volume % aluminum titanate) prepared in this study.

Figure 1 shows the microstructure of composite A (alumina grain size = 5.8  $\mu\text{m}$ ). The aluminum titanate phase is primarily distributed as isolated particles both at grain boundaries and within grains. Local concentrations of aluminum titanate are occasionally observed. These islands typically consist of 5-10 grains and are probably remnants of hard agglomerates in the base powder. The alumina matrix shows no sign of abnormal grain growth although faceted grain shapes are evident. The microstructure is of high density (~99%), as confirmed by direct measurements (Table 1), with angular pores resulting from grain pullout during polishing constituting the prominent surface defect population. Microcracks are seen in this composite and are predominantly associated with the islands of aluminum titanate.

Figure 2 shows the microstructure of composite B, (alumina grain size ~

14  $\mu\text{m}$ ). The primary distinctions between composites A and B are the increased scale of the microstructure in the latter and the widespread occurrence of microcracking in this coarser material. The difficulty in preparing quality polished sections for microscopy implies that the majority of the microcracks form spontaneously on cooling from the sintering temperature.

Figure 3 presents the measured inert strengths as a function of each indentation load for both materials. Each datum point represents the mean and standard deviation of, on average, four indentation-flaw failures; the shaded boxes at the far left represent failures from natural flaws. Figure 4 is a post mortem micrograph showing the fracture path in one specimen tested; the fracture clearly initiates from the indentation site. Great care was taken to ensure the indentation site was the source of the critical flaw for all data reported.

Both materials show unusually pronounced flaw tolerance behavior with little dependence of the strength on indentation load. The strengths of specimens containing 300 N indentations are only slightly degraded ( $\approx 8\%$ ) over the unindented controls. Composite B is considerably weaker, by a factor of  $\approx 5$ , than composite A for a relatively small ( $\approx 2\frac{1}{2}$ ) increase in grain size.

Observations of crack evolution from an indentation during static loading are presented as Figures 5-6. Figure 5 shows the crack pattern from a 30 N indentation during subsequent biaxial tensile loading. The radial cracks have extended stably from an initial size of the order of 100  $\mu\text{m}$  to sizes in the millimeter range. Note the cracks are in equilibrium with the applied tensile field. Figure 6 shows interactions of the primary radial crack with features of the microstructure. The failure mode is predominantly intergranular and active bridging can be readily observed. The primary crack is heavily

deflected on the scale of the grain size and tends to be attracted to the matrix-second phase interface.

Figure 7 shows a secondary crack 5-20 grain dimensions in size formed during the loading of composite A. Such secondary cracks are seen on the tensile surface of the test specimen within the zone of constant equibiaxial tension. The location of these cracks does not appear to correlate with the position and evolution of the primary cracks developing from the indentation site.

Figure 8 displays the load versus displacement of the testing machine cross-head responses for the two composites each containing 200 N Vickers indentations. The finer material (A) shows predominantly linear (Hookean) behavior during loading with slight non-linear characteristics just prior to peak load. The composite fails abruptly at peak load. The coarser material (B) shows very pronounced non-linear behavior with greater strain to a lower maximum in load. Failure then proceeds in a stable manner until final rupture at very large displacements (strains). Widespread secondary cracking is observed on the tensile face of composite B during testing. Note a finite force,  $P'$ , is required to separate the crack walls of composite B after large displacements.

#### 4 Discussion

Two important conclusions may be drawn from these experiments: (i) high-density alumina-aluminum titanate composites with controlled microstructures can be readily fabricated via a processing route using starting powders of

alumina and aluminum titanate; (ii) reinforcement of alumina with aluminum titanate results in composites with pronounced flaw tolerance.

The microstructures developed in the present work display several improvements over those generally produced by reaction sintering between alumina and titania [26-29]. The first clear improvement is the absence of abnormal grain growth and associated pore-grain boundary separation. Addition of the aluminum titanate phase prior to the start of sintering is thought to suppress the initiation of abnormal grains by a pinning mechanism similar to that suggested for other two-phase systems [35]. The second improvement is the attainment of high (~99% theoretical) fired densities. The high density results from the avoidance of pore-grain boundary separation associated with abnormal grain growth [36] and the indirect enhancement of densification with respect to coarsening resulting from grain growth inhibition [37]. Also, it is possible that the aluminum titanate enhances densification processes directly in a fashion analogous to the function of titania additions to alumina [38,39].

The indentation-strength properties of the composites may be compared with those of unreinforced aluminas of varying R-curve and flaw tolerance characteristics. Figure 9 presents the behavior of composite A together with trends for aluminas with grain sizes of 5.8 and 80  $\mu\text{m}$ . (The trends for the aluminas were calculated from a "calibrated" grain-bridging model used previously to interpret the effect of grain size on R-curve behavior [23,24]). It can be seen that composite A has superior flaw tolerance to the 80  $\mu\text{m}$  alumina (D); i.e: it is stronger and displays less degradation in strength with increasing contact load. The remaining alumina (C), with comparable grain size to composite A, shows higher strengths at lower indentation loads

but the strength degrades rapidly with increasing contact load and eventually fall well below composite A at the highest loads. Composite A is, therefore, a better choice of material than monophase alumina for applications where the component is subjected to in-service damage.

The composites may also be compared to pure aluminum titanate ceramics. It is generally difficult to fabricate aluminum titanate with sufficiently fine grain size to avoid spontaneous microcracking on cooling from the sintering temperature [26-29]. As such it is damage tolerant and shows strong R-curve behavior but at the same time is weak (strengths  $\approx$  20 MPa for optimum load-displacement characteristics) [40]. Composite B displays similar load versus cross-head displacement properties to pure aluminum titanate, is equally damage tolerant but is stronger by approximately a factor of three. Composite B may, therefore, be considered a contender for applications where pure aluminum titanate is presently used.

The unusual flaw tolerance of the aluminum titanate reinforced alumina composites results from strong stabilization of incipient critical flaws; this stabilization is a manifestation of pronounced R-curve behavior. The underlying physical mechanism(s) giving rise to the flaw tolerance properties observed are yet to be unequivocally identified. Evidence for grain bridging is presented in the form of in situ observations of loaded cracks (Fig. 6). The ability of composite B to support a finite load even after what is normally considered catastrophic failure (Fig. 8) further suggests the presence of intact grain bridges across the crack wall interfaces. These preliminary observations imply grain bridging is a contributor to the R-curve and flaw tolerance properties of the composites.

The subsidiary cracking observed on the tensile faces of the test

specimens is also expected to contribute to the damage tolerance of the composites. One consequence of the subsidiary cracking is nonlinear stress-strain response as reflected in the load-deflection traces recorded (Fig. 8). Such nonlinear behavior influences the strength properties by reducing the applied stress-intensity field [41,42]. The mechanism through which the composites tolerate widespread damage evolution is presently unclear. However, considering the potential benefits of such unusual damage-tolerant characteristics further investigation is warranted. It is worth noting that the behavior observed in the present work is similar to damage phenomena reported for some transformation-toughened zirconia ceramics [41] and continuous fiber-reinforced composites [43].

It is anticipated that the strength and damage tolerance properties of alumina-aluminum titanate composites can be further tailored through microstructure adjustment. When manipulating the toughness behavior in this manner there is a compromise between the component strength and flaw tolerance. Potential applications will ultimately depend on a fore-knowledge of the degree of damage a component is likely to experience and the stresses to be supported. It is recommended that  $\text{Al}_2\text{O}_3$  -  $\text{Al}_2\text{TiO}_5$  composites are given full consideration for components where damage tolerance and reliability are the primary design requirements.

#### ACKNOWLEDGEMENTS

The authors wish to thank E.P. Butler, B.R. Lawn, N.P. Padture, and J. Rödel for useful discussions. J.F. Kelly contributed to the SEM work, J. Cline assisted with the X-ray diffraction characterization and S. Darby machined the test specimens. The work was supported by the US Air Force Office of Scientific Research and E.I. duPont de Nemours & Co. Inc.

## REFERENCES

1. Hübner, H. & Jillek, W., Sub-critical crack extension and crack resistance in polycrystalline alumina. J. Mater. Sci. **12** (1977) 117-25.
2. Knehans, R. & Steinbrech, R.W., Memory effect of crack resistance during slow crack growth in notched  $Al_2O_3$  bend specimens. J. Mater. Sci. Lett. **1** (1982) 327-29.
3. Steinbrech, R.W., Knehans, R. & Schaarwächter, W., Increase of crack resistance during slow crack growth in  $Al_2O_3$  bend specimens. J. Mater. Sci. **18** (1983) 265-70.
4. Knehans, R. & Steinbrech, R.W., Effect of grain size on the crack-resistance curves of  $Al_2O_3$  bend specimens. In Science of Ceramics, Vol. 12, ed. P. Vincenzini. Ceramurgia, Imola, Italy, 1984, pp. 613-19.
7. Cook, R.F., Lawn, B.R. & Fairbanks, C.J., Microstructure-strength properties in ceramics: I. Effect of crack size on toughness. J. Am. Ceram. Soc. **68** (1985) 604-15.
8. Rose, L.R.F. & Swain, M.V., Two R-curves for partially stabilized zirconia. J. Am. Ceram. Soc. **69** (1986) 203-7.
9. Swain, M.V., R-curve behavior in a polycrystalline alumina material. J. Mater. Sci. Let. **5** (1986) 1313-15.
10. Lawn, B.R. & Fairbanks, C.J., Toughness and flaw responses in nontransforming ceramics: implications for NDE. In Review of Progress in Quantitative NDE, Vol. 6B, edited by D.O. Thompson and D.E. Chimenti. Plenum, New York, USA 1987, pp. 1023-30.
11. Bennison, S.J. & Lawn, B.R., Flaw tolerance in ceramics with rising crack-resistance behavior. J. Mater. Sci. **24** (1989) 3169-75.

12. Kendall, K., McN. Alford, N., Tan, S.R. & Birchall, J.D., Influence of toughness on Weibull modulus of ceramic bending strength. J. Mater. Res. 1 (1986) 120-23.
13. Cook, R.F. & Clarke, D.R., Fracture stability, R-curves and strength variability. Acta Metall. 36 (1988) 555-62.
14. Shetty, D.K. & Wang, J-S., Crack stability and strength distribution of ceramics that exhibit rising crack-growth-resistance (R-curve) behavior. J. Am. Ceram. Soc. 72 (1989) 1158-62.
15. Evans, A.G., New opportunities in the processing of high reliability structural ceramics. In Ceramic Transactions, vol. 1, edited by G.L. Messing, E.R. Fuller Jr., and H. Hausner. American Ceramic Society, Westerville, OH, USA, 1989, pp. 989-1010 .
16. Li, C-W. & Yamanis, J., Super-tough silicon nitride with R-curve behavior. Ceramic Engineering and Science Proceedings 10 (1989) 632-45.
17. Lathabai, S. & Lawn, B.R., Fatigue limits in noncyclic loading of ceramics with crack-resistance curves. J. Mater. Sci. 24 (1989) 4298-4306.
18. Evans, A.G., Perspectives on the development of high-toughness ceramics. J. Am. Ceram. Soc. 73 (1990) 187-206.
19. Swanson, P.L., Fairbanks, C.J., Lawn, B.R., Mai, Y-W. & Hockey, B.J., Crack-interface grain bridging as a fracture resistance mechanism in ceramics: I. Experimental study on alumina. J. Am Ceram. Soc. 70 (1987) 279-89.

20. Swanson, P.L., Crack-interface traction: A fracture-resistance mechanism in brittle polycrystals. In Advances in Ceramics, vol. 22, American Ceramic Society, Westerville, OH, USA 1988 pp. 135-55.
21. Mai, Y-W. & Lawn, B.R., Crack-interface grain bridging as a fracture resistance mechanism in ceramics: II. Theoretical Fracture Mechanics Model. J. Am. Ceram. Soc. 70 (1987) 289-94.
22. Cook, R.F., Fairbanks, C.J., Lawn, B.R. & Mai, Y-W., Crack resistance by interfacial bridging: Its role in determining strength characteristics. J. Mater. Research 2 (1987) 345-56.
23. Bennison, S.J. & Lawn, B.R., Role of interfacial grain-bridging sliding friction in the crack-resistance and strength properties of nontransforming ceramics. Acta Metall. 37 (1989) 2659-71.
24. Chantikul, P., Bennison, S.J. & Lawn, B.R., Role of grain size in the strength and R-curve properties of alumina. J. Am. Ceram. Soc. (1990) in press.
25. Bayer, G., Thermal expansion characteristics and stability of pseudobrookite type compounds,  $M_3O_5$ . J. Less Common Met. 24 (1971) 129-38.
26. Cleveland, J.J. & Bradt, R.C., Grain size/microcracking relations for pseudobrookite oxides. J. Am. Ceram. Soc. 61 (1978) 478-81.
27. Hamano, K., Ohya, Y. & Nakagawa, Z-E., Microstructure and mechanical strength of aluminum titanate ceramic prepared from mixture of alumina and titania. Yogyo-Kyokai-Shi 91 (1983) 95-101.

28. Ohya, Y., Hamano, K. & Nakagawa, Z-E., Microstructure and mechanical strength of aluminum titanate ceramics prepared from synthesized powders. Yogyo-Kyokai-Shi 91 (1983) 289-97.
29. Qian, D-F, Ohya, Y., Hamano, K. & Nakagawa, Z-E., Effects of excess alumina on microstructure of aluminum titanate ceramics prepared from mixture of alumina and titania. Yogyo-Kyokai-Shi 93 (1985) 315-21.
30. Okamura, H., Barringer, E.A. & Bowen, H.K., Preparation and sintering of narrow-sized  $Al_2O_3$ - $TiO_2$  composites. J. Mater. Sci. 24 (1989) 1867-1880.
31. Pennings, E.C.M. & Grellner, W., Precise nondestructive determination of the density of porous ceramics. J. Am. Ceram. Soc. 72 (1989) 1268-70.
32. Wurst, J.C. & Nelson, J.A., Lineal intercept technique for measuring grain size in two-phase polycrystalline ceramics. J. Am. Ceram. Soc. 55 (1972) 109.
33. Marshall, D.B., An improved biaxial flexure test for ceramics. Am. Ceram. Soc. Bull. 59 (1980) 551-53.
34. De With, G. & Wagemans, H.H.M., Ball-on-ring test revisited. J. Am. Ceram. Soc. 72 (1989) 1538-41.
35. Brook, R.J., Controlled grain growth. In Treatise on Materials Science and Technology, vol. 9, edited by F.F.Y. Wang, Academic Press, New York, NY, USA, 1976, pp. 331-64.
36. Coble, R.L. & Burke, J.E., Sintering in ceramics. Progr. Ceram. Sci. 3 (1963) 197-251.

37. Harmer, M.P., Use of solid-solution additives in ceramic processing. In Advance in Ceramics, vol. 10, edited by W.D. Kington, American Ceramic Society, Westerville, OH, USA, 1984, pp. 679-96.
38. Bagley, R.D., Cutler, I.B. & Johnson, D.L., Effect of  $TiO_2$  on initial sintering of  $Al_2O_3$ . J. Am. Ceram. Soc. **53** (1970) 136-41.
39. Morgan, P.E.D. & Koutsoutis, M.S., Phase studies concerning sintering in aluminas doped with  $Ti^{4+}$ . J. Am. Ceram. Soc. **68** (1985) C156-C158.
40. Hamano, K., Ohya, Y. & Nakagawa, Z-E., Crack propagation resistance of aluminum titanate ceramics. Int. J. High Technology Ceramics **1** (1985) 129-37.
41. Marshall, D.B., Strength characteristics of transformation-toughened zirconia. J. Am. Ceram. Soc. **69** (1986) 173-80.
42. Chuang, T-J. & Mai, Y.W., Flexural behavior of strain-softening solids. Int. J. Solids Structures **25** (1989) 1427-43.
43. Roach, D.A., Damage evolution in ceramic matrix composites. Paper 101-SIV-90 presented at The 92<sup>nd</sup> Annual Meeting of the American Ceramic Society, Dallas, TX, USA (1990).

Table 1. Microstructural characteristics of the two composites studied.

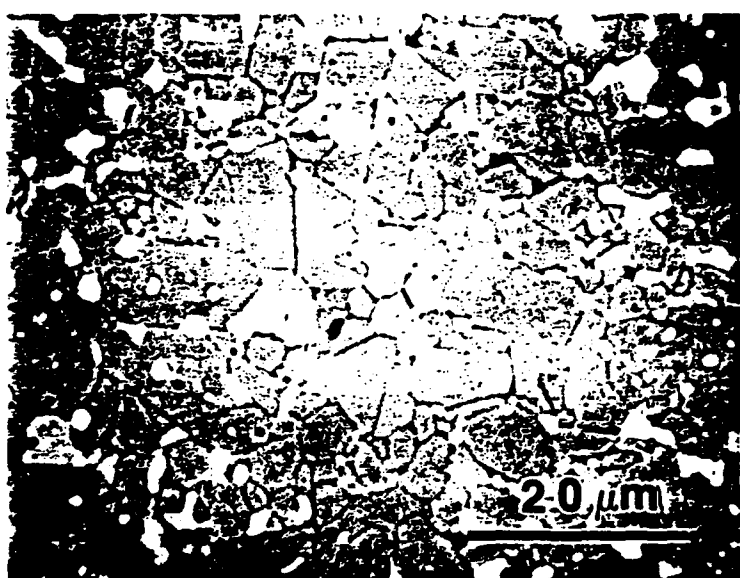
Composite	Volume % $\text{Al}_2\text{TiO}_5$	Grain Size $\text{Al}_2\text{O}_3$ ( $\mu\text{m}$ )	Density ( $\text{Mg} \cdot \text{m}^{-3}$ )	Phases Present
A	20	5.8	3.88 (98.9 %)	$\alpha\text{-Al}_2\text{O}_3$ $\beta\text{-Al}_2\text{TiO}_5$
B	20	$\approx 14$	3.89 (99.0 %)	$\alpha\text{-Al}_2\text{O}_3$ $\beta\text{-Al}_2\text{TiO}_5$

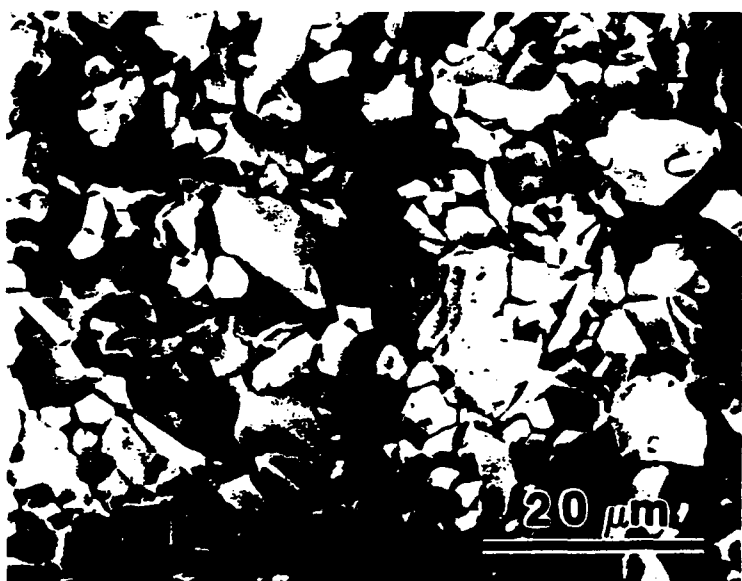
## FIGURE CAPTIONS

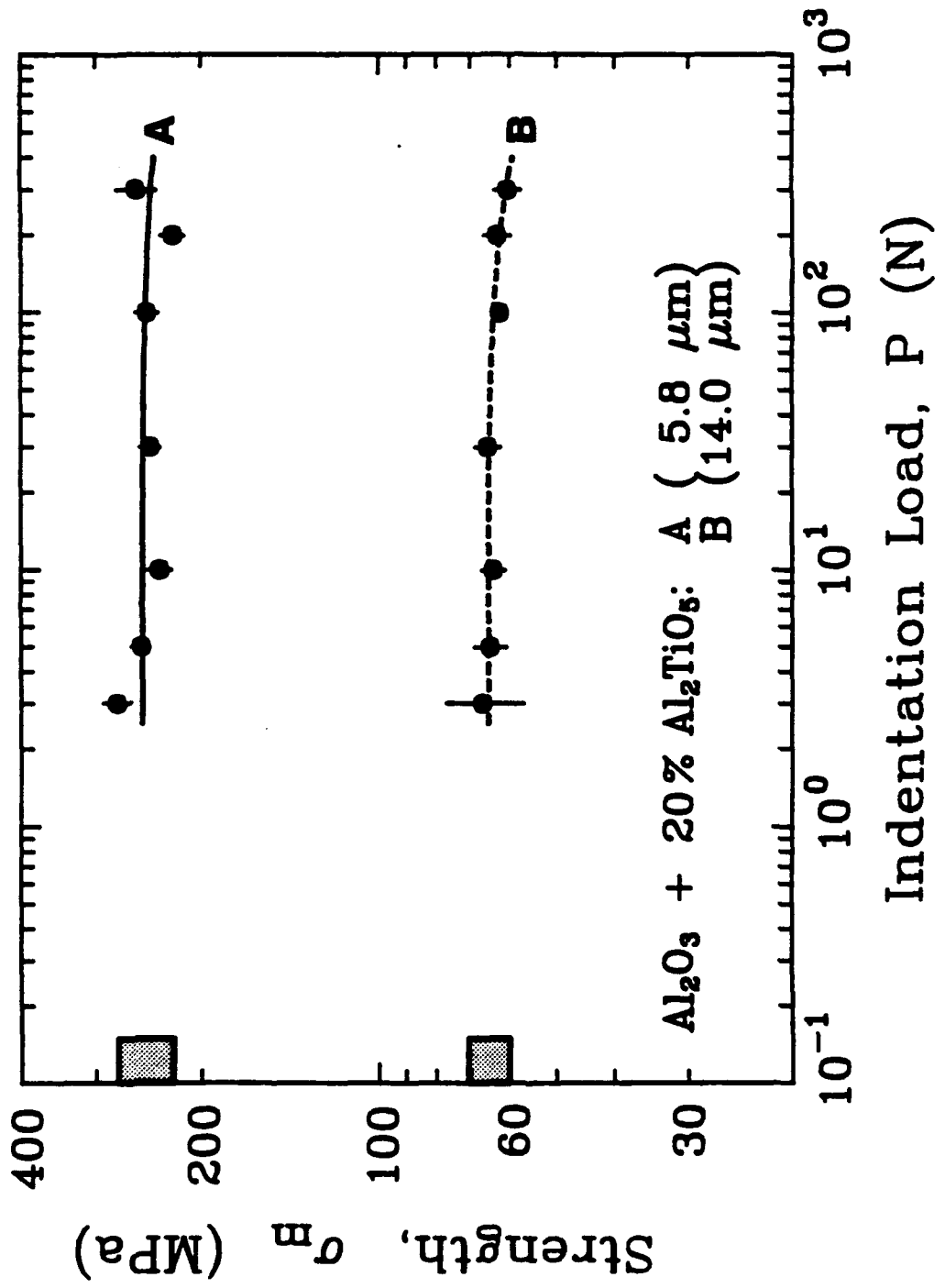
1. SEM micrograph (backscattered electron image) of a polished and etched section from composite A (20 volume %  $\text{Al}_2\text{TiO}_5$ ,  $\text{Al}_2\text{O}_3$  grain size =  $5.8 \mu\text{m}$ ). The lighter phase is  $\text{Al}_2\text{TiO}_5$ , the grey phase is  $\text{Al}_2\text{O}_3$  and the black phase is porosity.
2. SEM micrograph (backscattered electron image) of a fracture surface from composite B (20 volume %  $\text{Al}_2\text{TiO}_5$ ,  $\text{Al}_2\text{O}_3$  grain size  $\approx 14 \mu\text{m}$ ).
3. Plot of inert strength,  $\sigma_m$ , versus indentation load,  $P$ , for the two composites. The curves are empirical linear fits to the data and serve only as a guide to the eye. Note the pronounced flaw tolerance of these materials.
4. Optical micrograph (reflected light) of fracture path (post mortem) in composite A. The fracture clearly initiates from the 30 N indentation site (IS).
5. Optical micrograph (reflected light) of a 30 N indentation loaded in equibiaxial flexure (composite A). The radial cracks have grown stably from the initial size ( $\sim 100 \mu\text{m}$ ) produced by indentation and are in equilibrium with the applied tensile field.

(Figure captions continued)

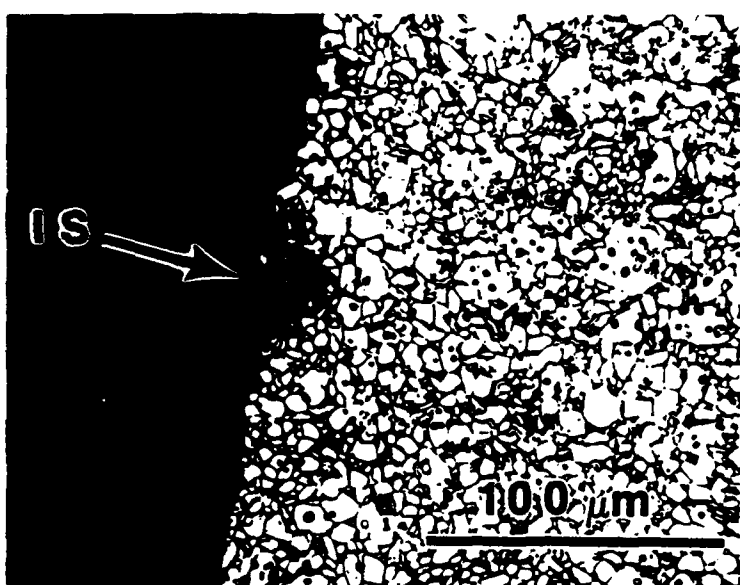
6. SEM micrograph (backscattered electron image) showing details of crack-microstructure interactions. Evidence for bridging grains can be seen (e.g. at B-B).
7. Optical micrograph (reflected light) of a secondary crack (C-C) located on the tensile face of one test specimen within the equibiaxial tensile zone.
8. Load vs. cross-head displacement traces for composites A and B each containing 200 N Vickers indentations. Material A displays unstable fracture at a critical displacement and evidence of slight nonlinearity prior to reaching peak load. Material B shows stable fracture and very pronounced nonlinear behavior. Note material B shows some load bearing capacity well after peak loading (denoted by P').
9. Strength,  $\sigma_m$ , versus indentation load, P, characteristics. Results for composite A compared to trends calculated for aluminas of grain sizes: C = 5.8  $\mu\text{m}$ , D = 79.8  $\mu\text{m}$  using a bridging model [23,24].

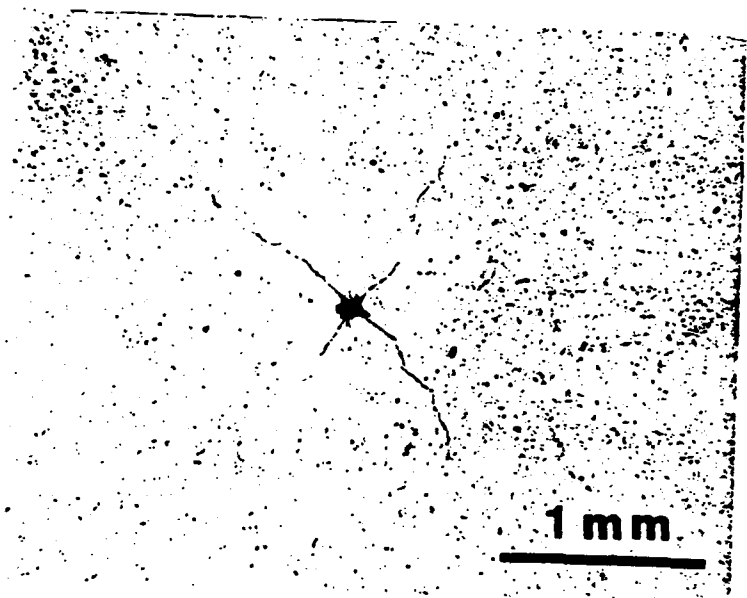


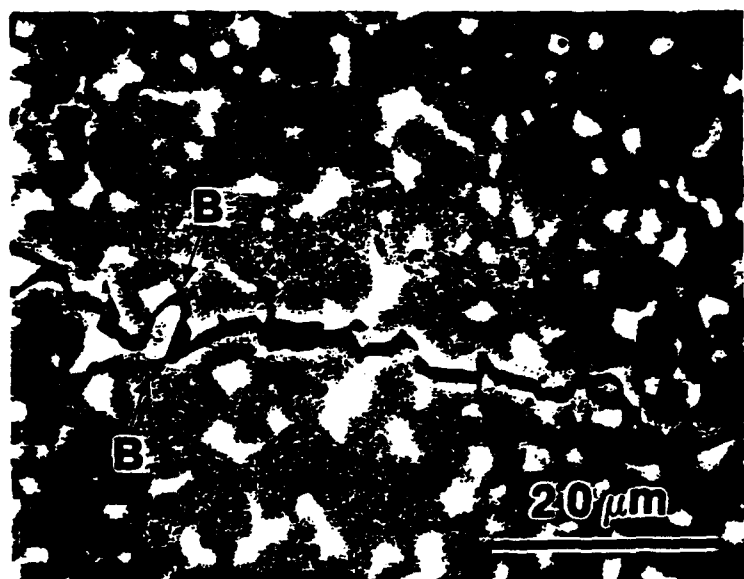


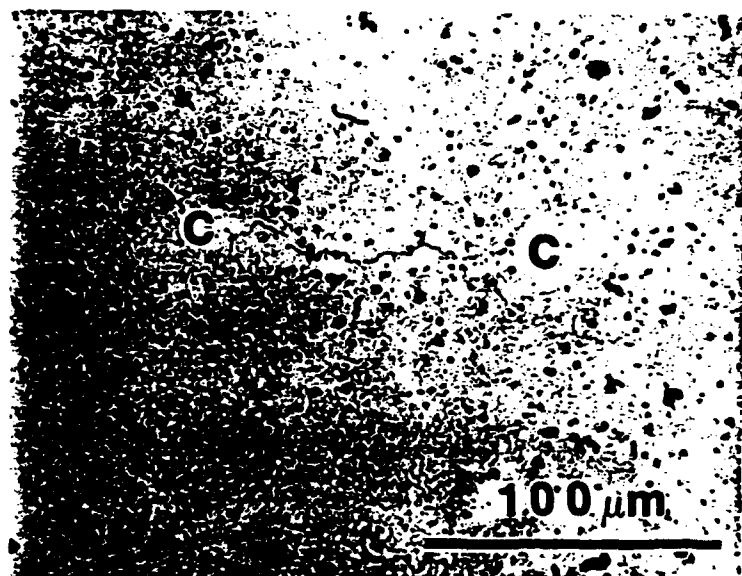


— FIG. 3. (Runyan & Bennison) —



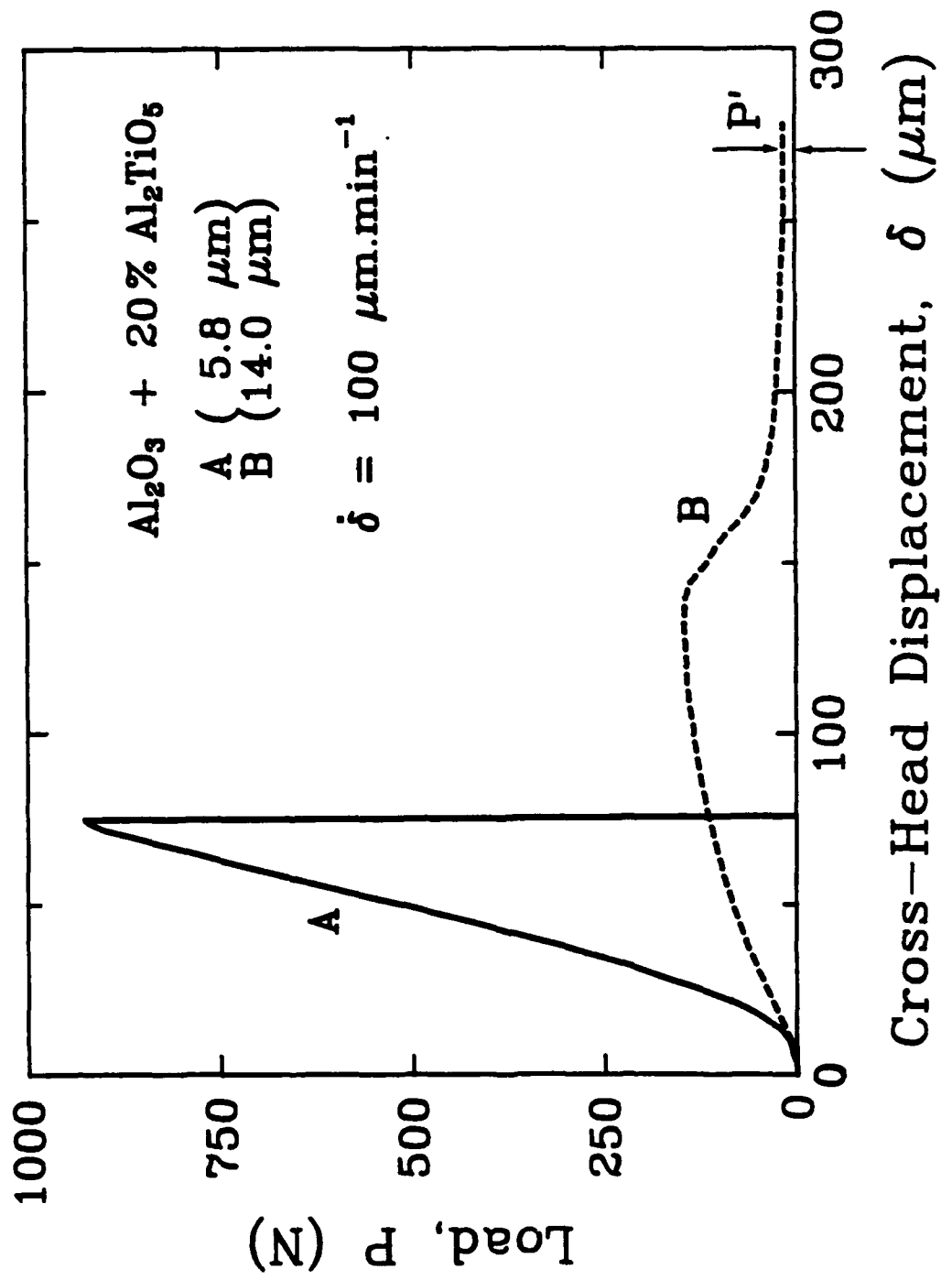






130

— FIG. 7. (Runyan & Bennison) —



— FIG. 8. (Runyan & Bennison) —

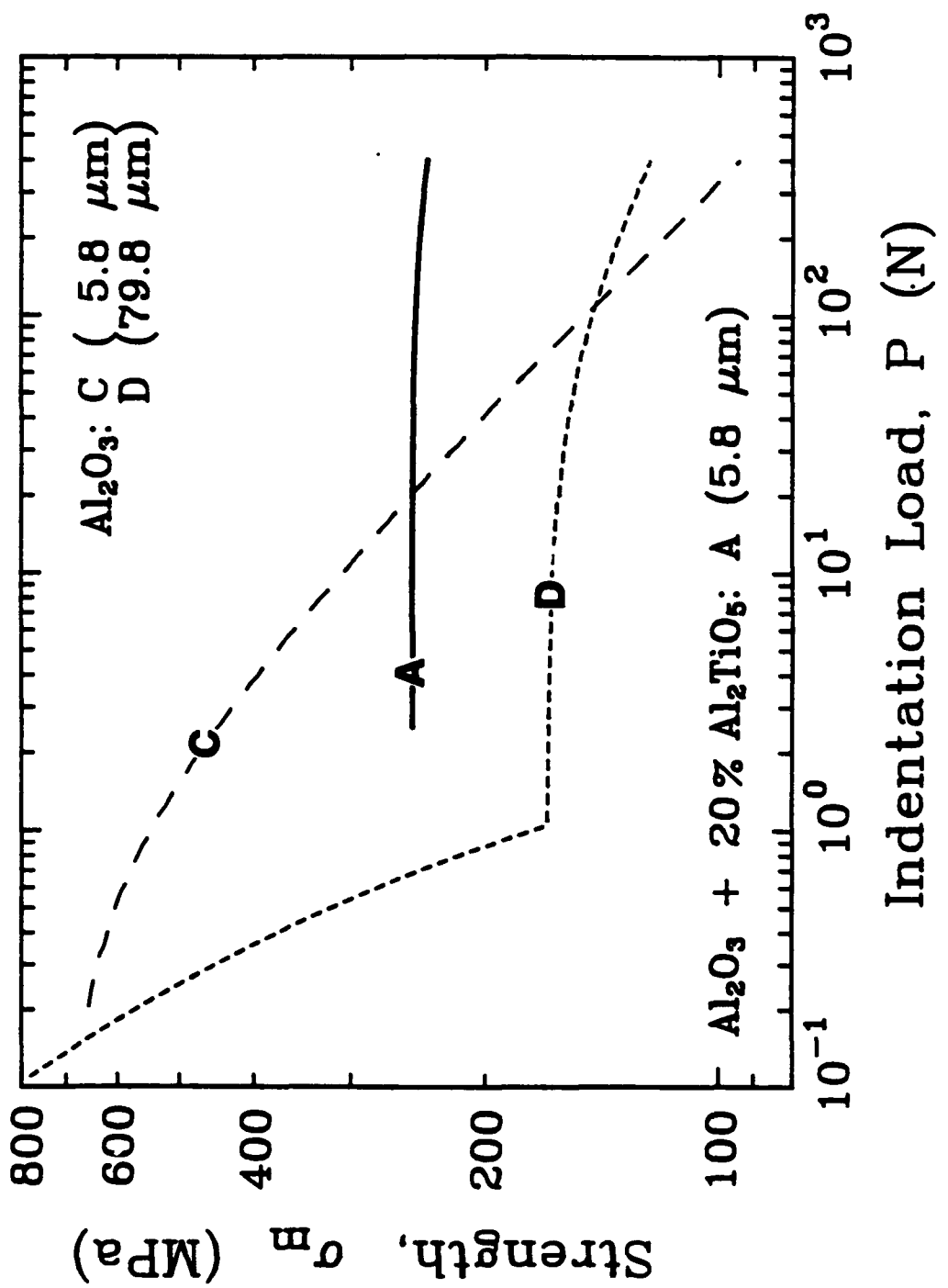


FIG. 9. Runyan & Bennison

FUNDAMENTAL CONDITION FOR EXISTENCE OF MICROCRACK CLOUDS  
IN MONOPHASE CERAMICS

Brian R. Lawn

Ceramics Division  
National Institute of Standards and Technology  
Gaithersburg, MD 20899

April 1990

For: J. European Ceram. Soc.

## ABSTRACT

Conditions for the existence of a microcrack cloud about a primary crack front in monophase polycrystalline ceramics are examined. With the assumption that microcracks initiate from sub-facet flaws, and that these flaws scale with the grain size, an expression is derived for the cloud radius. The cloud radius diminishes rapidly with grain size, from unlimited dimension at the critical size for spontaneous, general microcracking, to sub-grain level at some fraction of the critical size. The corresponding grain-size "window" is dependent on the flaw size, but is restrictively small for typical monophase ceramics.

Frontal-zone microcracking has been proposed as a mechanism of toughening [1-5] and consequent source of R-curve behaviour [5] in polycrystalline ceramics. In principle, individual microcracks can be activated at incipient sources, e.g. sub-facet grain boundary flaws, in the field of a primary crack. The primary-crack stresses may be augmented by internal residual tensile stresses from differential thermal expansion or elastic mismatch. In relieving these tensile stresses the fully developed microcracks remain irreversibly open, typically over several grain dimensions, thereby imposing a dilatant closure field on the primary crack [5].

The issue of microcracking involves two fundamental questions: (i) Under what conditions will a microcrack cloud exist?; (ii) Given that such a cloud does exist, what is the extent of toughening? The second of these questions has been frequently addressed, the first rarely. Thus the vast majority of studies presume the existence of a microcrack cloud. After all, above a critical grain size many noncubic ceramics do exhibit general, spontaneous microcracking throughout the material. However, definitive experimental supporting evidence for microcrack cloud zones in ceramics is almost totally lacking. Moreover, recent in situ observations of propagating cracks in aluminas and other R-curve ceramics [6,7] (previously considered prime candidates for microcracking [5]) reveal no evidence whatsoever for active frontal zones; on the other hand, considerable grain-interlock bridging activity is observed at the crack interface behind the crack tips. Those observations have led some to question the very existence of microcrack clouds in ceramic materials.

In the present note we consider this last point: what are the underlying conditions for existence of a microcloud zone? For simplicity, we focus on

monophase ceramics, although the principles to be outlined below extend to multiphase ceramics and, indeed, to other frontal-zone toughening processes (e.g. transformation toughening).

Consider a monophase ceramic material with predominantly intergranular fracture. For generality, suppose the material to be noncubic, to allow for any thermal expansion anisotropy stresses. We investigate the critical condition for microcrack initiation from the perspective of an observer at the tip of an equilibrium primary crack (P) looking outward toward potential sources (M) at  $(r, \theta)$ , Fig. 1. The stress  $\sigma^M$  acting on a particular active source, assumed to be located at a grain boundary sub-facet, is the superposition of two contributions:

(i) The mean (hydrostatic) tensile near-tip stress,  $\bar{\sigma}_{ii} = (\sigma_{rr} + \sigma_{\theta\theta} + \sigma_{zz})/3$ , in the polar field of the primary crack, evaluated from the Irwin displacement equation for a slit-like crack [8] at  $K = K^P$ ,

$$\bar{\sigma}_{ii} = K^P \bar{f}_{ii}(\theta) / (2\pi r)^{1/2} \quad (1)$$

with  $\bar{f}_{ii}(\theta) = (2/3)(1 + \nu)\cos(\theta/2)$  [5,9]. This stress component has a maximum value  $\bar{f}_{ii}(\theta) = 0.72$  at  $\theta = 60^\circ$  [9].

(ii) The tensile component of the thermal expansion anisotropy stress

$$\sigma_R = E\Delta\alpha\Delta T / (1 + \nu) \quad (2)$$

with  $\Delta\alpha$  the differential expansion coefficient between adjacent grains and  $\Delta T$  the temperature range through which the material deforms elastically during the first cooling cycle. Of course,  $\sigma_R = 0$  for cubic materials.

Approximating the sources as uniformly stressed penny-shaped flaws of radius  $c_0$ , the critical stress intensity factor for microcrack extension is [8]

$$\begin{aligned} K^M &= 2\sigma_C^M (c_0/\pi)^{1/2} \\ &= 2(\bar{\sigma}_{ii} + \sigma_R)(c_0/\pi)^{1/2} = T_0 \end{aligned} \quad (3)$$

with  $T_0$  the intrinsic grain boundary toughness.

Mention was made of a critical grain size,  $\ell_C$  say, above which noncubic ceramics tend to general microcracking during initial cooling. It is accordingly of interest to determine the conditions for microcracking in the absence as well as in the presence of a primary crack, to establish an upper bound to the scale of the frontal cloud. Suppose that the dimensions  $c_0$  and  $r$  in Fig. 1 scale directly with grain size  $\ell$ , i.e. in accordance with the principles of geometrical similitude, so that the corresponding normalised quantities

$$\underline{C}_0 = c_0/\ell \quad (4a)$$

$$\underline{R} = r/\ell \quad (4b)$$

are scale-invariant. Then we may distinguish between spontaneous and activated microcracking, as follows:

(i) Spontaneous (general) microcracking. In the absence of any primary crack ( $\bar{\sigma}_{ii} = 0$ ), sources M initiate at tensile sub-facets from the sole action of the internal stress ( $+\sigma_R$ ). Equation (3) is then satisfied at the critical grain size

$$\ell_C = (\pi/4\underline{C}_0)(T_0/\sigma_R)^2. \quad (5)$$

Above  $l_c$  general microcracking occurs from active sources throughout the material. Taking typical values for alumina,  $T_0 \approx 2.0 \text{ MPa} \cdot \text{m}^{1/2}$ ,  $\sigma_R \approx 250 \text{ MPa}$ ,  $C_0 \approx 0.5$  (say), we obtain  $l_c \approx 100 \mu\text{m}$  in eqn. 5; this is of the order of the critical grain size observed experimentally. We note that whereas some grain facets are in tension ( $+\sigma_R$ ), others will be in compression ( $-\sigma_R$ ), so the initiated microcracks arrest at neighbouring facets (incipient bridging sites [10,11]) after extending  $\approx 3-5$  grain diameters.

(ii) Activated (cloud) microcracking. Now consider the grain-size domain  $l \leq l_c$ . Active microcracking is confined to a cloud around the tip of primary crack P, within a maximum radius determined by inserting  $K^P = T_0$  in eqn. 1 and combining with eqn. 3:

$$\underline{R}_c = 2\underline{C}_0 \{ \bar{f}_{ii} / \pi [1 - (l/l_c)^{1/2}] \}^2. \quad (6)$$

We plot  $\underline{R}_c$  as a function of  $l/l_c$  in Fig. 2, at two bounding values of  $\underline{C}_0$ , with  $\bar{f}_{ii}$  evaluated at  $\theta = 60^\circ$  as above.

These calculations help to explain why microcrack clouds may not be as prevalent as generally presumed. In interpreting the plots in Fig. 2, we note that the condition  $\underline{R}_c = r_c/l = \infty$  indicates an upper bound for general microfracture, as described by eqn. 5; and  $\underline{R}_c = 1$  indicates a lower level below which microcrack sources simply coalesce into the primary crack, i.e. there can be no detached cloud. With that, consider two limiting cases in eqn. 6:

(a)  $\ell/\ell_c \rightarrow 1$ ,  $\underline{R}_c \rightarrow \infty$ , corresponding to the limiting grain size for general microfracture.

(b)  $\ell/\ell_c \rightarrow 0$ ,  $\underline{R}_c \approx 0.1 \underline{C}_0$ , relating to materials for which  $\ell \rightarrow 0$  or  $\ell_c \rightarrow \infty$  ( $\sigma_R \rightarrow 0$  in eqn. 5). Thus, since  $\underline{C}_0 < 1$  generally, it follows that  $\underline{R}_c < 0.1$ , so that no microcracking, spontaneous or activated, is expected in fine-grained or cubic materials. Physically, this is because the sub-facet flaws lie too far distant (one grain dimension or more) from the primary-crack tip for the near field alone to be effective; decreasing the grain size brings the sources closer (eqn. 4b), but this is more than counteracted by a diminished flaw size (eqn. 4a).

Figure 2 shows that between these limits the cloud radius diminishes rapidly with decreasing grain size, more so at smaller  $c_0$ . Thus for "well made" ceramics (small  $c_0$ ) the "window" of allowable grain sizes for the activation of significant clouds (at  $r_c/\ell > 10$ , say) may simply be too restrictive for common observation.

We are led to believe, especially in light of the current trend for materials processors to fabricate fine-grained, flaw-free microstructures, that microcrack-cloud toughening is unlikely to be a commonplace observation in monophase ceramics. Alternative toughening modes, e.g. grain-interlock bridging [5,6], are not subject to the same restrictive windows, and are therefore expected to dominate over the broader range of grain sizes.

In principal, the above analysis should be extendable to multiphase ceramics, and to other frontal-zone processes, with cosmetic adjustments to the treatment. It is conceivable that the flexibility afforded by addition of

a second phase (e.g. removal of necessity to conform to the restrictions of geometrical similarity) could facilitate an expansion of the grain-size window, and thereby make microcracking a more viable prospect. In this context it is interesting to note that the best validated observations of microcrack zones in ceramics have been reported in two-phase systems [12].

#### ACKNOWLEDGEMENTS

The author thanks S.J. Bennison, S. Lathabai and J. Rödel for comments and discussions. This work was funded by the U.S. Air Force Office of Scientific Research.

## REFERENCES

- [1] R.G. Hoagland, J.D. Embury and D.J. Green, On the Density of Microcracks Formed During the Fracture of Ceramics. Scripta Met. 9[9] 907-09 (1975).
- [2] A.G. Evans, On the Formation of a Crack-Tip Microcrack Zone. Scripta Met. 10[1] 93-97 (1976).
- [3] N. Claussen, J. Steeb and R.F. Pabst, Effect of Induced Microcracking on the Fracture Toughness of Ceramics. Amer. Ceram. Soc. Bull. 56[6] 559-62 (1977).
- [4] A.G. Evans and K.T. Faber, Crack-Growth Resistance of Microcracking Brittle Materials. J. Amer. Ceram. Soc. 67[4] 255-60 (1984).
- [5] D.R. Clarke, A Simple Calculation of Process-Zone Toughening by Microcracking. J. Amer. Ceram. Soc. 67[1] C-15-16 (1984).
- [6] P.L. Swanson, C.J. Fairbanks, B.R. Lawn, Y-W. Mai and B.J. Hockey, Crack-Interface Grain Bridging as a Fracture Resistance Mechanism in Ceramics: I. Experimental Study on Alumina. J. Amer. Ceram. Soc. 70[4] 279-89 (1987).
- [7] P.L. Swanson, Crack-Interface Traction: A Fracture-Resistance Mechanism in Brittle Polycrystals; pp. 135-55 in Advances in Ceramics, Vol. 22, Fractography of Glasses and Ceramics. American Ceramic Society, Columbus, OH, 1988.
- [8] B.R. Lawn and T.R. Wilshaw, Fracture of Brittle Solids. Cambridge University Press, London, 1975, Ch. 3.
- [9] R.M. McMeeking and A.G. Evans, Mechanics of Transformation Toughening in Brittle Materials. J. Amer. Ceram. Soc. 65[5] 242-46 (1982).

[10] S.J. Bennison and B.R. Lawn, Role of Interfacial Grain-Bridging Sliding Friction in the Crack-Resistance and Strength Properties of Nontransforming Ceramics. Acta Metall. 37[10] 2659-71 (1989).

[11] Prapaipan Chantikul, S.J. Bennison and B.R. Lawn, Role of Grain Size in the Strength and R-Curve Properties of Alumina. J. Amer. Ceram. Soc., in press.

[12] M. Ruhle, N. Claussen and A.H. Heuer, Transformation Toughening and Microcracking as Complementary Processes in  $ZrO_2$ -Toughened  $Al_2O_3$ . J. Amer. Ceram. Soc. 69[3] 195-97 (1986).

FIGURE CAPTIONS

1. Coordinates for evaluating microcrack initiation in polycrystalline material. Intrinsic penny-like microcrack flaw (M) at  $(r, \theta)$ , radius  $c_0$  (not shown), subjected to superposed opening stresses  $\sigma^M$  from field of primary crack (P) and thermal expansion mismatch stresses. It is assumed that the microstructure satisfies conditions of geometrical similarity at different grain sizes  $\ell$ , such that  $c_0$  and  $r$  scale with  $\ell$ .
2. Microcrack cloud radius around primary crack tip as function of grain size, for two values of penny-flaw diameter.

